



**HAL**  
open science

# Multi-instrument and modelling studies of ionospheres at Earth and Mars

Maxime Grandin

► **To cite this version:**

Maxime Grandin. Multi-instrument and modelling studies of ionospheres at Earth and Mars. Earth and Planetary Astrophysics [astro-ph.EP]. Université Toulouse 3 Paul Sabatier (UT3 Paul Sabatier), 2017. English. NNT: . tel-01636840

**HAL Id: tel-01636840**

**<https://theses.hal.science/tel-01636840>**

Submitted on 17 Nov 2017

**HAL** is a multi-disciplinary open access archive for the deposit and dissemination of scientific research documents, whether they are published or not. The documents may come from teaching and research institutions in France or abroad, or from public or private research centers.

L'archive ouverte pluridisciplinaire **HAL**, est destinée au dépôt et à la diffusion de documents scientifiques de niveau recherche, publiés ou non, émanant des établissements d'enseignement et de recherche français ou étrangers, des laboratoires publics ou privés.



# THÈSE

En vue de l'obtention du

## DOCTORAT DE L'UNIVERSITÉ DE TOULOUSE

**Délivré par :**

Université Toulouse 3 Paul Sabatier (UT3 Paul Sabatier)

**Cotutelle internationale avec :**

University of Oulu (Finlande)

---

**Présentée et soutenue par :**

**Maxime Grandin**

Le 26 octobre 2017

**Titre :**

Étude multi-instrumentale et modélisation des ionosphères terrestre et martienne

---

**École doctorale et discipline ou spécialité :**

ED SDU2E : Astrophysique, Sciences de l'Espace, Planétologie

**Unité de recherche :**

Sodankylä Geophysical Observatory et Institut de Recherche en Astrophysique et Planétologie

**Directeur(s) de Thèse :**

Dr Alexander Kozlovsky, Dr Aurélie Marchaudon,  
Codirecteurs : Prof. Anita Aikio, Dr Thomas Ulich

**Rapporteurs :**

Prof. Kathryn McWilliams  
Dr Ronan Modolo

**Autre(s) membre(s) du jury :**

Dr Mervyn Freeman  
Dr Pierre-Louis Blelly



**SODANKYLÄ GEOPHYSICAL OBSERVATORY  
PUBLICATIONS**



No. 113

**MULTI-INSTRUMENT AND MODELLING STUDIES OF THE  
IONOSPHERES AT EARTH AND MARS**

**MAXIME GRANDIN**

Sodankylä 2017



**SODANKYLÄ GEOPHYSICAL OBSERVATORY  
PUBLICATIONS**



No. 113

**MULTI-INSTRUMENT AND MODELLING STUDIES OF THE  
IONOSPHERES AT EARTH AND MARS**

**MAXIME GRANDIN**

Academic dissertation  
University of Oulu Graduate School  
Faculty of Science

*Academic dissertation to be presented, with the assent of the Doctoral Training Committee of Technology and Natural Sciences of the University of Oulu and of the Sciences de l'Univers, de l'Environnement et de l'Espace (SDU2E) Doctoral School of the Université Toulouse III Paul Sabatier, for public discussion in the Polaria lecture hall of Sodankylä Geophysical Observatory on 26 October 2017 at 12 o'clock noon.*

Sodankylä 2017

SODANKYLÄ GEOPHYSICAL OBSERVATORY PUBLICATIONS

Editor: Dr Thomas Ulich  
Sodankylä Geophysical Observatory  
FI-99600 SODANKYLÄ, Finland

This publication is the continuation of the former series  
“Veröffentlichungen des geophysikalischen Observatoriums  
der Finnischen Akademie der Wissenschaften”

Sodankylä Geophysical Observatory Publications

ISBN 978-952-62-1614-0 (paperback)

ISBN 978-952-62-1615-7 (pdf)

ISSN 1456-3673

**OULU UNIVERSITY PRESS**

**Sodankylä 2017**

## Abstract

This thesis studies the ionospheres of the Earth and Mars by combining the observations of versatile instruments providing information on various aspects of the planetary environments. The work on the terrestrial ionosphere focuses particularly on solar wind–magnetosphere–ionosphere coupling, while the work on the Martian ionosphere is based on the development of a new approach to analyse radio-occultation data to retrieve the atmospheric and ionospheric profiles.

In the Earth’s ionosphere, two papers study the effects of solar wind high-speed streams on the ionospheric  $F$ -region peak electron density and on cosmic noise absorption resulting from the precipitation of energetic ( $>30$  keV) electrons into the  $D$  region. For the first paper, a modified version of the superposed epoch analysis method, called phase-locked superposed epoch analysis method, was developed. The main finding is that a depletion near the  $F$ -region peak takes place in the afternoon and evening sectors during high-speed stream events. This could be explained by an increase in the electron loss rate as a consequence of ion-neutral frictional heating, which enhances the ion temperature and leads to neutral atmosphere expansion. In addition, dayside and post-midnight  $F$ -peak electron density increases are observed, probably related to soft particle precipitation. The second study reveals that cosmic noise absorption occurs during up to 4 days after the arrival of a high-speed stream, as substorm-injected energetic electrons precipitate in the midnight to early-afternoon ionosphere, principally at auroral latitudes. A third study reports for the first time observations of a modulation of cosmic noise absorption at periods near 10 s, associated with pulsating aurora. This suggests that the energetic component of the precipitating flux is modulated consistently with the auroral (1–10 keV) energies.

At Mars, radio-occultation experiments have been performed by the Mars Express spacecraft since 2004. In this thesis, a new data analysis approach is developed, based on the numerical simulation of radio wave propagation through modelled Martian atmosphere and ionosphere. This approach enables one to overcome limitations inherent in the classical inversion method which has been in use so far. It also gives access to new parameters such as ion density profiles. The new method is tested by analysing the data from two radio-occultation experiments.

*Keywords:* Auroral ionosphere, ionosphere–magnetosphere coupling, solar wind high-speed streams, Martian atmosphere and ionosphere, radio-occultation.



## Tiivistelmä

Tämä väitöskirja tutkii Maapallon ja Marsin ionosfäärejä yhdistämällä useiden eri instrumenttien havaintoja, joilla saadaan tietoa planeettojen ympäristöistä. Maapallon ionosfääriä koskeva työ tutkii aurinkotuuli-magnetosfääri-ionosfääri-kytkentää, kun taas Marsin ionosfääriä koskevan työn tavoite on uuden radio-okkultaatiomittauksen data-analyysimenetelmän kehittäminen, joka tuottaa ilma-kehän ja ionosfäärin profiileja.

Maan ionosfäärin tapauksessa yhdessä julkaisussa tutkitaan nopeiden aurinkotuulivirtausten vaikutuksia  $F$ -kerroksen elektronitiheyteen ja toisessa julkaisussa tutkitaan energettisten ( $>30$  keV) elektronien sateesta johtuvaa kosmisen radiokohinan absorptiota  $D$ -kerroksessa. Ensimmäisessä julkaisussa on kehitetty uusi versio data-analyysimenetelmästä, jota kutsutaan vaihelukituksi epookkien superpositiomenetelmäksi. Julkaisun päätulos on, että nopeiden aurinkotuulivirtausten aikana  $F$ -kerroksen maksimielektronitiheys pienenee iltapäivän ja illan sektoreilla. Tämä voidaan selittää johtuvan siitä, että ioni-neutraalitörmäysten synnyttämä kitkalämpö kasvattaa ionilämpötilaa ja aiheuttaa lisäksi ilma-kehän laajenemisen. Molemmat prosessit kasvattavat elektronien häviönopeutta.  $F$ -kerroksen elektronitiheysmaksimi puolestaan kasvaa sektorilla, joka ulottuu keskiyöstä aamun kautta keskipäivään, ja tämä johtuu matalaenergeettisestä elektronisateesta. Toisessa julkaisussa havaitaan, että lisääntynyt kosmisen radiokohinan absorptio kestää jopa neljä päivää nopean aurinkotuulivirtauksen saavuttua Maan kohdalle. Tämä johtuu siitä, että alimyrskyitse injektoidut energettiset elektronit satavat keskiyön ja aamun ionosfääriin, pääasiassa revontuliovaalin alueella. Kolmas julkaisu raportoi ensimmäistä kertaa havainnon sykkiviin revontuliin liittyvästä kosmisen radiokohinan absorptiosta n. 10 s jaksollisuudella. Tämä osoittaa, että elektronivuon energettinen komponentti on moduloitu samalla jaksollisuudella kuin revontulielektronien energiat (1–10 keV).

Marsissa on tehty radio-okkultaatiomittauksia vuodesta 2004 saakka Mars Express-luotaimen avulla. Väitöskirjassa on kehitetty uusi datan analyysimenetelmä, joka perustuu numeeriseen simulointiin radioaaltojen etenemisestä Marsin ilma-kehässä ja ionosfäärissä. Tämän lähestymistavan avulla vältetään tähän asti käytetyn klassisen inversiomenetelmän rajoitukset. Lisäksi menetelmä tuottaa uusia parametrejä kuten ionitiheysprofiileja. Uutta menetelmää testattiin tulkiten kahden radio-okkultaatiomittauksen aineistoa.

*Asiasanat:* Revontuli-ionosfääri, ionosfääri-magnetosfääri-kytkentä, nopeat aurinkotuulivirtaukset, Marsin ilma-kehä ja ionosfääri, radio-okkultaatio.



## Résumé

Le travail présenté dans ce manuscrit de thèse s’articule autour de l’étude des ionosphères terrestre et martienne. Une approche multi-instrumentale est adoptée afin de combiner des observations permettant de mettre en perspective des manifestations de phénomènes physiques de natures différentes mais intervenant dans un même contexte global. Le travail doctoral comporte également un volet modélisation. Le manuscrit de thèse consiste en une partie introductrice à laquelle sont adossées cinq publications dans des revues scientifiques à comité de lecture.

La partie introductrice de ce manuscrit de thèse a pour objectif de présenter le contexte scientifique sur lequel est basé le travail doctoral. Un premier chapitre passe en revue les principaux aspects théoriques dans lesquels s’inscrivent les études dont les résultats sont publiés dans les cinq articles. Les atmosphères et ionosphères de la Terre et de Mars y sont succinctement décrites, de même que les interactions entre ces planètes et le vent solaire, comprenant notamment la formation de magnétosphères. Les deux chapitres suivants présentent les instruments dont sont issues les données utilisées dans ce travail doctoral ainsi que les méthodes d’analyse des données. Le quatrième chapitre résume les principaux résultats obtenus autour des trois grandes thématiques abordées au cours de cette thèse. Enfin, des pistes quant à la continuation potentielle du travail présenté dans ce manuscrit de thèse sont évoquées en conclusion.

Le premier article porte sur une étude statistique des effets des courants de vent solaire rapide sur la région  $F$  de l’ionosphère aurorale. Il s’appuie sur des données mesurées par l’ionosonde de Sodankylä entre 2006 et 2008. Au cours de cette période, 95 événements associés à des courants de vent solaire rapide ont été sélectionnés, et la réponse de l’ionosphère au-dessus de Sodankylä a été étudiée à partir des fréquences critiques des régions  $E$  et  $F$  de l’ionosphère, qui donnent la valeur du pic de concentration électronique dans ces deux régions. Pour cela, une version modifiée de la méthode des époques superposées a été développée, appelée “méthode des époques superposées avec verrouillage de phase”. Une augmentation du pic de concentration des régions  $E$  et  $F$  est observée du côté nuit et le matin, en lien avec une activité aurorale accrue, tandis qu’une déplétion de la région  $F$  est révélée aux temps magnétiques locaux situés entre 12 h et 23 h. Une estimation des effets d’une possible modification de l’équilibre photo-chimique résultant d’un accroissement du chauffage issu de la friction entre les ions et les éléments neutres est proposée.

Le deuxième article s’intéresse aux précipitations énergétiques dans l’ionosphère aurorale durant ces mêmes 95 événements, en étudiant l’absorption du bruit cosmique qui en résulte. Il apparaît que les événements au cours desquels le vent solaire

demeure rapide pendant plusieurs jours produisent davantage de précipitations énergétiques, qui peuvent atteindre les latitudes subaurorales. Par ailleurs, trois types de précipitations énergétiques sont étudiés séparément, selon qu'elles sont associées avec des signatures de sous-orage magnétique, avec des pulsations géomagnétiques, ou ni l'un ni l'autre. Les deux premiers types de précipitations semblent liés. En effet, l'analyse des données suggère que les électrons énergétiques sont injectés dans la magnétosphère interne durant les sous-orages. Tandis qu'une partie d'entre eux précipitent immédiatement du côté nuit, d'autres dérivent vers le côté matin, où ils subissent des interactions avec des ondes électromagnétiques de type siffleur (*whistler* en anglais), qui peuvent être modulées par des pulsations géomagnétiques, menant à leur précipitation.

Le troisième article présente pour la première fois l'observation de signatures d'aurore pulsante dans des données d'absorption du bruit cosmique. Ces signatures sont consistantes avec les pulsations observables dans l'émission aurorale, et semblent indiquer une modulation cohérente des composantes aurorale (1–10 keV) et énergétique ( $> 30$  keV) du spectre des précipitations électroniques au cours d'une aurore pulsante.

Le quatrième article introduit une nouvelle méthode proposée pour analyser les données de radio-occultation mesurées par la sonde Mars Express. Cette approche vise à contourner des difficultés posées par les hypothèses fortes nécessaires à la mise en œuvre de la méthode classique d'inversion, notamment celle d'un environnement martien à symétrie sphérique – qui n'est pas acceptable lors de sondages proches du terminateur jour-nuit. La nouvelle méthode est basée sur la modélisation de l'atmosphère et de l'ionosphère de Mars, et sur la simulation de la propagation des ondes radio entre la station sol sur Terre et Mars Express lors d'une expérience de radio-occultation. Les paramètres libres contrôlant les profils atmosphériques et ionosphériques sont ajustés afin que la simulation reproduise le plus fidèlement possible les mesures.

Le cinquième article est une réponse à un commentaire sur l'article précédent. Il vise d'une part à répondre aux critiques émises sur la méthode développée, montrant que celles-ci n'en remettent en cause ni la validité ni la pertinence, et d'autre part à y apporter quelques améliorations.

*Mots-clefs:* Ionosphère aurorale, couplages ionosphère–magnétosphère, courants de vent solaire rapide, atmosphère et ionosphère martiennes, radio-occultation.

*This thesis is dedicated to those who never had a chance to fully express their potential because of discriminations based on their social background, ethnical origin, gender, sexual orientation or physical condition. May society find the path towards becoming fully inclusive and tolerant.*



## Acknowledgements

This doctoral work has been carried out at Sodankylä Geophysical Observatory (SGO), an independent department of the University of Oulu, Finland, and at the Institut de Recherche en Astrophysique et Planétologie (IRAP), Toulouse, France. My first thanks go to my supervisors, Dr Alexander Kozlovsky, Dr Aurélie Marchaudon, Prof. Anita Aikio, and Dr Thomas Ulich. Their guidance, their patience and their constant support have been invaluable throughout my doctoral training. I thank the evaluators of this thesis who accepted to provide criticism to my work: Dr Ronan Modolo (opponent and pre-examiner), Dr Mervyn Freeman (opponent), and Prof. Kathryn McWilliams (pre-examiner). I am also grateful to the members of my follow-up group, Prof. Ilya Usoskin, Dr Mikko Orispää, and Dr Ilpo Virtanen. I acknowledge the former Exactus doctoral programme of the University of Oulu Graduate School for funding this doctoral work alongside SGO.

I warmly thank the other coauthors of the papers on which this thesis is based: Dr Pierre-Louis Blelly, Dr Olivier Witasse, Mr Tero Raita, Dr Antti Kero, Dr Noora Partamies, Mr Derek McKay, Dr Daniel Whiter, and Prof. Yoshizumi Miyoshi. Their valuable input and feedback largely contributed to the success of the corresponding studies. I also want to thank my colleagues from SGO and IRAP for making the work environment a nice place and for helping me in all kinds of matters, especially: Mr Romain Bielawski, Mr Mikel Indurain, Ms Issaad Kacem, Ms Pirkko Kaukonen, Mr Michaël Lavarra, Ms Liliana Macotela Cruz, Dr Jyrki Manninen, Mr Johannes Norberg, Dr Frédéric Pitout, Mr Nicolas Rey, Dr Lassi Roininen, Ms Iina Sirviö, Ms Morgane Steckiewicz, Dr Geneviève Soucail, Mr Tomi Teppo, Dr Esa Turunen, Ms Sirkku Väitalo, and Ms Jaana Yli-Suvanto. And I want to extend my thanks beyond these two institutes to collaborators whose humanity and passion for science have fuelled my desire to be part of the space physics community, in particular to Ms Mary McCready, Dr Kirsti Kauristie, Dr Noora Partamies, Dr Anja Strømme, and Prof. Juha Vierinen. They are in some sense my “science heroes”.

Last but not least, I wish to thank my family and friends for not forgetting me and for remaining present during these four years of doctoral training, in spite of the distance. No need to name them; they know who they are!

Sodankylä, 30 August 2017  
Maxime Grandin



# Contents

Abstract . . . . .	iii
Tiivistelmä . . . . .	v
Résumé . . . . .	vii
Acknowledgements . . . . .	xi
<b>Original publications</b>	<b>1</b>
<b>1 Introduction</b>	<b>3</b>
1.1 Atmospheres and ionospheres . . . . .	3
1.1.1 Neutral atmospheres . . . . .	3
1.1.2 Ionospheres . . . . .	6
1.1.2.1 Photoionisation, chemistry and transport . . . . .	6
1.1.2.2 Structures of the terrestrial and Martian ionospheres	7
1.2 Solar wind . . . . .	10
1.2.1 General properties . . . . .	10
1.2.2 High-speed streams . . . . .	11
1.3 Magnetospheres . . . . .	12
1.3.1 Terrestrial magnetosphere . . . . .	12
1.3.2 Martian induced magnetosphere . . . . .	15
1.4 Planetary environments and solar wind interactions . . . . .	16
1.4.1 Reconnection and convection . . . . .	16
1.4.2 Geomagnetic storms and magnetospheric substorms . . . . .	18
1.4.3 Particle precipitation . . . . .	19
1.4.4 Some aspects of Mars interactions with the solar wind . . . . .	21
<b>2 Instrumentation</b>	<b>23</b>
2.1 Ground-based instruments . . . . .	23
2.1.1 Sodankylä ionosonde . . . . .	23
2.1.2 IMAGE magnetometers . . . . .	26
2.1.3 SGO riometer chain and KAIRA . . . . .	27
2.1.4 Kilpisjärvi All-Sky Camera . . . . .	29
2.2 Satellites . . . . .	30
2.2.1 Mars Express . . . . .	30
2.2.2 NOAA/POES . . . . .	31
2.2.3 ACE . . . . .	31

<b>3</b>	<b>Methods</b>	<b>33</b>
3.1	Superposed epoch analysis . . . . .	33
3.1.1	Classical version . . . . .	33
3.1.2	Phase-locked version . . . . .	34
3.2	Radio-occultation . . . . .	36
3.2.1	Principle . . . . .	36
3.2.2	Data analysis . . . . .	37
<b>4</b>	<b>Results</b>	<b>41</b>
4.1	Effects of solar wind high-speed streams on the high-latitude ionosphere of the Earth . . . . .	41
4.1.1	Solar wind driving . . . . .	42
4.1.2	Overview of ionospheric response to high-speed streams . . . .	42
4.1.3	<i>E</i> and <i>F</i> region responses . . . . .	45
4.1.4	Energetic particle precipitation . . . . .	47
4.2	Modulation of energetic precipitation during pulsating aurora . . . .	50
4.3	Analysis of Mars Express data with the radio-occultation model . . . .	52
4.3.1	Reproduction of the frequency residual profile . . . . .	52
4.3.2	Influence of medium asymmetry . . . . .	54
4.3.3	Ion density profiles . . . . .	56
4.3.4	Improvements introduced in Paper V . . . . .	57
<b>5</b>	<b>Conclusion</b>	<b>59</b>
	<b>Bibliography</b>	<b>63</b>

# Original publications

This thesis consists of an introductory part and the following original papers:

- I Grandin, M., A. T. Aikio, A. Kozlovsky, T. Ulich, and T. Raita (2015), Effects of solar wind high-speed streams on the high-latitude ionosphere: Superposed epoch study, *Journal of Geophysical Research: Space Physics*, *120*, 10,669–10,687, doi:10.1002/2015JA021785.
- II Grandin, M., A. T. Aikio, A. Kozlovsky, T. Ulich, and T. Raita (2017), Cosmic radio noise absorption in the high-latitude ionosphere during solar wind high-speed streams, *Journal of Geophysical Research: Space Physics*, *122*, 5203–5223, doi:10.1002/2017JA023923.
- III Grandin, M., A. Kero, N. Partamies, D. McKay, D. Whiter, A. Kozlovsky, and Y. Miyoshi (2017), Observation of pulsating aurora signatures in cosmic noise absorption data, *Geophysical Research Letters*, *44*, 5292–5300, doi:10.1002/2017GL073901.
- IV Grandin, M., P.-L. Blelly, O. Witasse, and A. Marchaudon (2014), Mars Express radio-occultation data: A novel analysis approach, *Journal of Geophysical Research: Space Physics*, *119*, 10,621–10,632, doi:10.1002/2014JA020698.
- V Grandin, M., P.-L. Blelly, O. Witasse, and A. Marchaudon (2016), Reply to comment by Pätzold et al. on “Mars Express radio-occultation data: A novel analysis approach”, *Journal of Geophysical Research: Space Physics*, *121*, 10,592–10,598, doi:10.1002/2015JA022229.

In the text, the original papers are referred to by their Roman numerals.

The original idea of studying solar wind high-speed stream effects using ionosonde and riometer data from the Sodankylä Geophysical Observatory instruments was proposed by Prof. A. Aikio. In Papers I and II, the author carried out the data analysis and data visualisation, with regular feedback and guidance from coauthors, and was the responsible writer. The author had the original idea which led to the development of the phase-locked superposed epoch analysis presented in Paper I.

Comparing cosmic noise absorption data within chosen beams of the Kilpisjärvi Atmospheric Imaging Receiver Array with optical data during a pulsating aurora event was suggested by Dr A. Kero during a workshop at the International Space Science Institute (ISSI). The author exploited this idea with regular discussions and input from the coauthors of Paper III, and was the responsible writer of the paper. The pre-processing of cosmic noise absorption data and the Sodankylä Ion–Neutral Chemistry model simulations mentioned in the paper were made by Dr A. Kero.

The original idea of the new analysis approach for Mars Express radio-occultation data was formulated by Dr P.-L. Blelly. The method presented in Papers IV and V was developed by the author, under the guidance of coauthors. In particular, the atmospheric and ionospheric models for Mars were built, partly using already existing codes (e.g., the kinetic code for photoionisation). In addition, the ray-tracing model used for the calculation of radio wave trajectories during radio-occultation experiments was developed by the author. Finally, the author was the responsible writer for Papers IV and V.

# Chapter 1

## Introduction

Planetary ionospheres owe their formation and their dynamics to the Sun, through its radiation and its expanding atmosphere and magnetic field – the solar wind. The work presented in this thesis is focused on the ionospheres of the Earth and Mars and their behaviours in response to solar wind driving. To study the terrestrial ionosphere, the approach adopted during this doctoral work was to combine observations from various ground-based and satellite instruments (Papers I, II and III). To analyse radio-occultation data from the Mars Express mission, modelling work was undertaken in order to develop a new approach enabling to overcome assumptions limiting the use of the classical inversion method (Papers IV and V).

This chapter gives an overview of the theoretical background on which the work presented in this thesis is based. Chapter 2 presents the instruments which provided the data used in the papers, and Chapter 3 shortly introduces the methods which were utilised. The main results of Papers I to V are summarised in Chapter 4, and concluding remarks are made in Chapter 5.

### 1.1 Atmospheres and ionospheres

#### 1.1.1 Neutral atmospheres

Both the Earth and Mars exert gravitational forces great enough to maintain an atmosphere. While their atmospheres differ by their composition, their pressure levels and their temperature profiles, they are essentially governed by the same equations (continuity, momentum, diffusion...). Physical parameters, such as temperature, pressure and density of a given species, exhibit spatiotemporal variations resulting from the boundary conditions and the external sources of energy applied to the atmosphere, and their time evolution. The main external source providing energy to planetary atmospheres is the Sun, whose radiation heats the atmospheric constituents. An immediate consequence is that typical atmospheric profiles are different on the dayside and nightside of a planet, and also vary according to solar activity. Other sources of energy include for instance galactic cosmic rays [e.g., *Velinov et al.*, 2013],

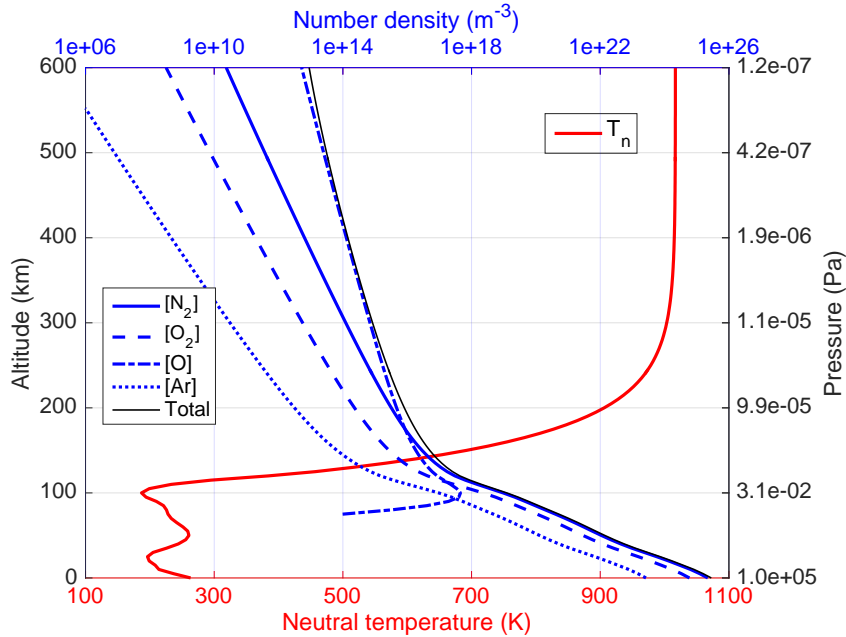


**Figure 1.1.** Altitude profiles in the terrestrial atmosphere above Sodankylä on 1 January 2014 at 12:00 local time, taken from the MSIS-90 model. Red: Neutral temperature. Blue: Number densities of  $\text{N}_2$  (solid),  $\text{O}_2$  (dashed),  $\text{O}$  (dash-dotted), and  $\text{Ar}$  (dotted). Black: Total neutral density.

particle precipitation (see section 1.4.3), Joule heating, atmospheric gravity waves [Hickey *et al.*, 2011], or volcanism [Vyushin *et al.*, 2004].

Figure 1.1 gives typical profiles of the main atmospheric parameters for the Earth, given by the MSIS-90 model [Hedin, 1991] above Sodankylä on 1 January 2014 at 12:00 local time. Focusing first on the temperature profile, one may notice several vertical gradient inversions below 100 km altitude, which define four distinct regions, called with increasing altitude: troposphere, stratosphere, mesosphere, and thermosphere. Above 100 km altitude, i.e., in the thermosphere, the influence of the 11-year solar cycle is significant. The exospheric temperature (i.e., the temperature in the outermost regions of the atmosphere) may vary from about 1000 K during so-called solar minimum conditions to 1400 K during so-called solar maximum conditions [Brekke, 2012]. The composition of the atmosphere varies with altitude. Below 100 km, the atmosphere is a well-mixed gas made of, roughly, 78% of nitrogen ( $\text{N}_2$ ), 21% of oxygen ( $\text{O}_2$ ) and 1% of argon ( $\text{Ar}$ ) and other gases. Above 100 km, as density decreases, collisions become less frequent and each species therefore behaves independently. While the heaviest species are more affected by gravitation and tend to remain at lower altitude, the lightest ones are prone to escaping. Atomic oxygen, formed by dissociation of  $\text{O}_2$  by solar ultraviolet (UV) radiation, appears

above  $\sim 90$  km altitude, and becomes the main species above  $\sim 150$  km [Rees, 1989]. Other atomic species (He and H) become dominant in the topside atmosphere (above  $\sim 600$  km) [Hargreaves, 1995].

Another key parameter in a planetary atmosphere is the scale height, noted  $H$  and given by

$$H = \frac{k_B T}{Mg}, \quad (1.1)$$

with  $k_B$  the Boltzmann constant,  $T$  the temperature,  $M$  the molecular mass, and  $g$  the standard acceleration due to gravity. Under the hydrostatic equilibrium assumption, the neutral density  $N$  at altitude  $z$  can be calculated as a function of temperature by

$$N(z) = N_0 \frac{T_0}{T(z)} \exp \left[ - \int_{z_0}^z \frac{dz}{H(z)} \right], \quad (1.2)$$

where  $N_0$ ,  $T_0$  are neutral density and temperature values at a reference altitude  $z_0$ . In the case of an isothermal atmosphere, this equation simplifies into

$$N(z) = N_0 \exp \left[ - \frac{z - z_0}{H} \right], \quad (1.3)$$

and the scale height therefore gives the altitude increase corresponding to a density decrease by a factor of  $e$ . Above 100 km altitude, each neutral constituent has its own scale height. The scale heights are of the order of a few kilometres below 100 km altitude, and increase to several tens of kilometres above, with a dependency on solar activity since they depend on temperature. Correspondingly, the neutral density in the thermosphere and exosphere also depends on solar activity.

At Mars, the atmosphere is governed by the same concepts, with some differences. First, the composition of the Martian atmosphere is very different. Below 120 km altitude, where the atmosphere is a well-mixed gas [Izakov, 2007], the main constituent is carbon dioxide ( $\text{CO}_2$ , 96%), the remainder consisting mostly of argon and molecular nitrogen [Mahaffy *et al.*, 2013]. Above 200 km altitude, atomic oxygen (O) becomes the main neutral species [Fox, 2009]. The temperature essentially decreases from ground level to about 40–120 km altitude, where it reaches a minimum [Nier and McElroy, 1977; Seiff and Kirk, 1977]. Above that, the thermospheric profile is exponential, the exospheric temperature ranging between 200 and 300 K, depending on solar activity [Fox, 2009]. Finally, the Martian atmosphere is very rarefied, with ground pressure levels of the order of 100 times lower than on Earth. Figure 1.2 gives an example of atmospheric temperature and neutral density profiles (for  $\text{CO}_2$ , O and  $\text{N}_2$ ) obtained from the Mars Climate Database v5.2 [Millour *et al.*, 2015] during the conditions of the landing of the Curiosity rover, on 6 August 2012.

One specificity of the Martian atmosphere is the dust which is lifted from the ground up to 60 km altitude by strong winds during the dust storm season [Clancy *et al.*, 2010]. This dust strongly affects the temperature and densities in the lower atmosphere, especially by absorbing solar radiation and reemitting energy in the infrared frequency range, hence heating the neutral gas.

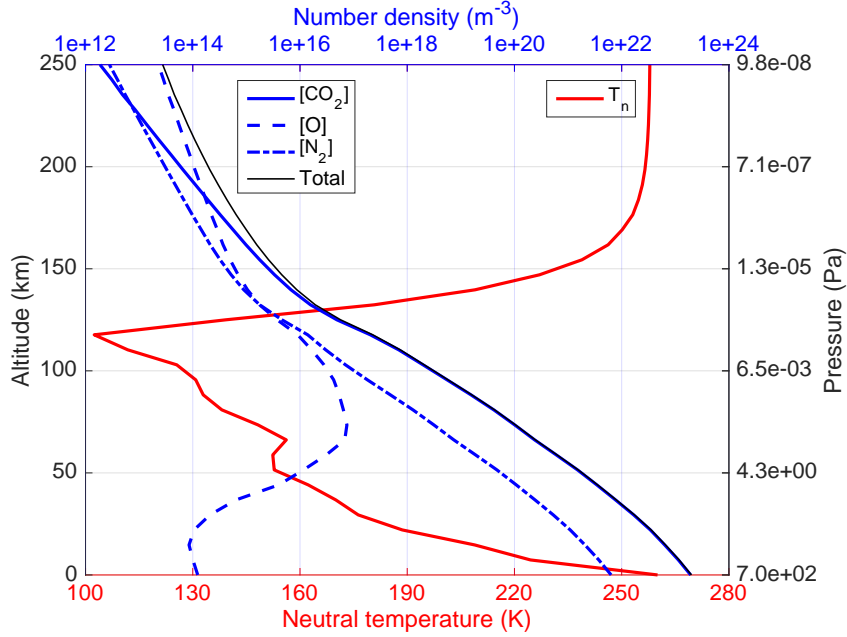


**Figure 1.2.** Altitude profiles in the Martian atmosphere at the landing time and location of the Curiosity rover, given by the Mars Climate Database v5.2. Red: Neutral temperature. Blue: Number densities of CO<sub>2</sub> (solid), O (dashed) and N<sub>2</sub> (dash-dotted). Black: Total neutral density.

A comparison of the terrestrial and Martian neutral atmospheres shows that, besides very different compositions, the two main differences noticeable in the presented parameters are that (1) pressure and total neutral density are about two orders of magnitude smaller at Mars than at Earth, and (2) the Martian atmosphere is overall colder than the terrestrial atmosphere. At ground level, the temperature difference is only of the order of a few tens of Kelvin, but the exospheric temperature is significantly higher at Earth (1000–1400 K) than at Mars (200–300 K).

## 1.1.2 Ionospheres

### 1.1.2.1 Photoionisation, chemistry and transport

Besides heating the atmosphere, the solar radiation also modifies its composition. Solar photons in the extreme ultraviolet (EUV) and X-ray energy ranges indeed carry enough energy to dissociate molecules and ionise constituents. As a result, a great number of photochemical and chemical reactions take place in the atmospheres of the Earth and Mars, including photodissociation, photoionisation, charge exchange and recombination reactions.

In the upper atmosphere, ion species and free electrons are always present, and this region is called the *ionosphere*. The ionosphere is a plasma of low ionised fraction ( $10^{-3}$  for the Earth,  $10^{-5}$  for Mars). Ionospheres are commonly divided into regions, based on their electron density altitude profiles.

In an ionosphere, neutrals, electrons and ions behave differently. The motion of neutral species (neutral winds) is mostly driven by pressure gradient forces. The motion of electrons mainly depends on electromagnetic fields, as their collision frequency with other species is very low. They follow the  $\mathbf{E} \times \mathbf{B}$  drift (see section 1.4.1), at a speed  $\mathbf{v}_{E \times B} = \mathbf{E} \times \mathbf{B} / B^2$  (with  $\mathbf{E}$  the electric field and  $\mathbf{B}$  the magnetic field). The motion of ion species, on the other hand, is influenced by both electromagnetic fields and collisions with neutral particles. The ion-neutral collision frequency varies with altitude. In the lower ionosphere (up to about 200 km altitude for the Earth and Mars [Vogt *et al.*, 2016]), collisions with the neutrals are frequent, and as a result the ions drift at a speed with a component parallel to the electric field and a component in the  $\mathbf{E} \times \mathbf{B}$  direction. Since the ion motion is not in the same direction as the motion of the electrons, currents are flowing in the plasma. At higher altitude, however, the collisions are rare enough to allow the ion motion to follow the  $\mathbf{E} \times \mathbf{B}$  drift, as for the electrons [Brekke, 2012]. This produces plasma convection [Hargreaves, 1995]. The field-aligned motion of ions is dominated by the field-aligned component of the neutral wind. Ambipolar diffusion of electrons and ions, essentially upwards, also plays a role in the field-aligned motion of charged particles [Rees, 1989].

### 1.1.2.2 Structures of the terrestrial and Martian ionospheres

The terrestrial ionosphere is mainly divided into three regions according to the electron density profile. Figure 1.3 shows typical electron density profiles in the ionosphere of the Earth during daytime and nighttime, as well as density profiles of the main ions during daytime. Between about 60 and 90 km altitude, the so-called *D* region has a complex photochemistry, which includes negative and cluster ions [Turunen *et al.*, 1996]. It is formed principally by solar Lyman- $\alpha$ , EUV and hard X-ray radiation, galactic cosmic rays, and energetic to relativistic particle precipitation from the magnetosphere (see section 1.4.3). The *D* region generally disappears at night, as recombination takes place rapidly in this region where collision frequencies are high.

Between 90 and 150 km altitude, approximately, the *E* region predominantly consists of  $\text{O}_2^+$  and  $\text{NO}^+$  ions. In this region, the motions of ions and electrons are decoupled, which allows the existence of electric currents flowing in this part of the ionosphere. The *E* region electron density is greatly reduced at night, but at high latitudes it may also be significantly enhanced by auroral precipitation.

Above 150 km altitude, the *F* region contains the main electron density peak, which may be of the order of  $10^{12} \text{ m}^{-3}$ . During solar maximum and on the dayside, the *F* region may exhibit a bulge under the main peak; it is then commonly divided into *F*<sub>1</sub> and *F*<sub>2</sub> regions. The *F*<sub>1</sub> region consists mostly of molecular ions ( $\text{O}_2^+$  and  $\text{NO}^+$ ) and disappears at night, while the dominant species in the *F*<sub>2</sub> peak is  $\text{O}^+$ . The main peak altitude typically ranges between 250 and 300 km during daytime, and between 300 and 400 km during nighttime [Rishbeth *et al.*, 2000a].

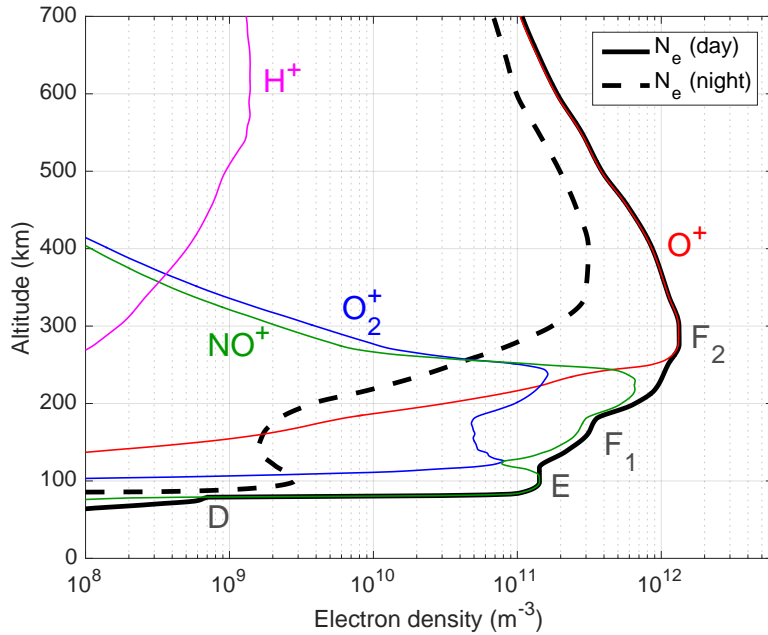


**Figure 1.3.** Typical electron density profiles in the daytime (black, solid) and nighttime (black, dashed) terrestrial ionosphere (after *Cravens* [1997]). Density profiles of the main ion species in the daytime ionosphere are given in colours. The ion composition was estimated using the TRANSCAR model [*Blelly et al.*, 2005].

In spite of the background atmosphere being different, the Martian ionosphere presents a structure with some similarities to the terrestrial ionosphere. The same general formation mechanisms – photoionisation, chemistry, ion and electron diffusion – lead to the creation of an ionosphere with two main regions. While there is no commonly used official nomenclature for the Martian ionospheric regions, it is chosen here to follow *Rishbeth and Mendillo* [2004] and call them  $M_1$  and  $M_2$ . Figure 1.4 shows a typical electron density profile from 60 to 240 km altitude in the dayside Martian ionosphere. The main peak  $M_2$  is located at about 120 km altitude and its electron density is of the order of  $10^{11} \text{ m}^{-3}$ . The secondary peak,  $M_1$ , lies at 100–110 km altitude and resembles more a bulge than an independent peak. In fact, the  $M_1$  and  $M_2$  regions are believed to be distinct when the solar zenith angle is high and to merge to form a single electron density peak near local noon [*Mayyasi and Mendillo*, 2015]. The main ion species in both regions is  $\text{O}_2^+$ , but  $\text{NO}^+$  may become dominant below 100 km altitude [*Fox*, 2009]. The nightside ionosphere of Mars is significantly less well-known, but recent studies suggest that the ionisation does not completely disappear at night [*Withers et al.*, 2012; *Fowler et al.*, 2015]. Besides, it has been found that the global dust storms, by affecting the neutral atmosphere (see section 1.1.1), may also have an effect on the ionosphere. Indeed, the dust-loaded

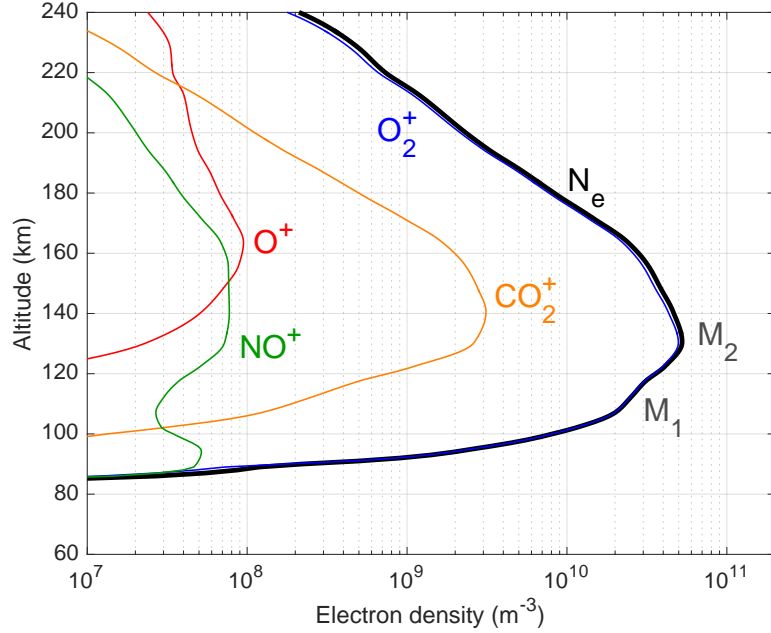


**Figure 1.4.** Electron and main ion density profiles in the dayside Martian ionosphere, given by the model developed in this thesis work. In the chosen example, the local solar zenith angle is  $82^\circ$ .

gas heating may lead to an enhancement of neutral density in the upper atmosphere, favouring photoionisation at higher altitudes and thus resulting in an increase in the  $M_2$  region peak altitude [Wang and Nielsen, 2003].

In addition to the main ionospheric region consisting of  $M_1$  and  $M_2$ , some studies have revealed a sporadic layer at lower altitude, supposedly originating from meteoric ablation and therefore consisting of metallic ions (mostly  $\text{Mg}^+$  and  $\text{Fe}^+$ ) [Molina-Cuberos *et al.*, 2003]. This layer is located around 80 km altitude, and it almost disappears on the nightside. Models have also predicted the existence of ionisation associated with cosmic rays down to about 35 km altitude [Withers, 2009; Cardnell *et al.*, 2016].

The main differences between the terrestrial and Martian ionospheres can be summarised as follows. First, the altitude extent of the ionosphere of Mars is reduced compared to the terrestrial case, as the main peak is located around 120 km (versus 250–300 km at Earth) during daytime. Second, the main peak electron density is one order of magnitude lower at Mars than at Earth ( $\sim 10^{11}$  vs  $10^{12}$   $\text{m}^{-3}$ ). Third, the main ion species at most altitudes in the Martian ionosphere is  $\text{O}_2^+$ , whereas in the ionosphere of the Earth  $\text{O}^+$  dominates in the main peak and above, and  $\text{NO}^+$  dominates in the  $E$  and lower  $F$  regions.

These descriptions of the terrestrial and Martian ionospheres correspond to typical, undisturbed conditions, and the presented electron density profiles are idealised ones. However, ionospheres are subject to great dynamical variations triggered by disturbances in the nearby space. In the case of the Earth, for instance, there is a strong coupling between the ionosphere, the magnetosphere (described in section 1.3.1) and the solar wind. At Mars, a coupling between the ionosphere and the solar wind also exists, and will be described in section 1.4.4.

## 1.2 Solar wind

### 1.2.1 General properties

The Sun also affects the planetary environments through the continuous expansion of its own atmosphere, the corona. This plasma flow is called the *solar wind*, and it is the main driver of space weather.

The outward flow of the solar wind originates from the pressure gradient existing between the solar surface and the outer solar atmosphere, whose effect is greater than the gravitational forces exerted on the coronal constituents. The main constituents of the solar wind are protons and electrons, and about 5% of the positive charge carriers are  $\alpha$ -particles ( $\text{He}^{2+}$ ) [Hundhausen, 1995]. When measured near the Earth's orbit, the average solar wind ion density is of the order of 3–10 particles per cubic centimetre. Its velocity is predominantly radial and typically ranges between 200 and 800 km/s [Hargreaves, 1995]. The dynamic pressure, given by  $p_{\text{dyn}} = \rho V^2$  (with  $\rho$  the mass density and  $V$  the velocity) [Walker and Russel, 1995], is therefore most of the time of the order of a few nanopascals. At Mars, the Mars Atmosphere and Volatile Evolution (MAVEN) mission recently started to provide solar wind observations using the Suprathermal and Thermal Ion Composition instrument. A statistical study by Masunaga et al. [2017] using 1.3 year of measurements estimated that ion density, solar wind velocity and dynamic pressure have values at Mars of the order of 1–10  $\text{cm}^{-3}$ , 200–600 km/s, and 0.2–2.0 nPa, respectively.

The solar wind being a plasma originating from the Sun, which has an intrinsic magnetic field, it drags the solar magnetic field along its outward motion. This comes from the fact that the solar wind conductivity along the magnetic field lines is very high, and this is called the “frozen-in” flux concept [e.g., Baumjohann and Treumann, 1997]. The magnetic field carried by the solar wind is called *interplanetary magnetic field* (IMF). Since the Sun rotates around its spin axis and the solar wind mostly flows radially, the interplanetary magnetic field lines draw a spiral in the interplanetary space, which is called the Parker spiral, after Parker [1958]. At the Earth and Mars orbits, the spiral angles made with the Sun–planet direction are close to  $45^\circ$  and  $57^\circ$ , respectively. The IMF strength is typically of the order of 5 nT near the Earth [Brekke, 2012] and 3 nT near Mars [Masunaga et al., 2017], yet values may commonly range from 1 to 15 nT.

The solar wind exhibits great spatiotemporal variability, both during quiet and disturbed conditions. Disturbances in the background plasma flow may be created

by structures forming on the solar surface. The most extreme type of disturbances arises when solar plasma is released from the surface of the Sun, forming a so-called *coronal mass ejection* (CME). Such a structure exhibits a large magnetic field magnitude and often travels at high speed (exceptionally up to 2500 km/s) in the interplanetary medium [Lugaz *et al.*, 2005]. CMEs are most frequent during the period of maximum activity in the 11-year solar cycle, and they are often released following a sudden brightening of a localised region at the surface of the Sun, called a solar flare [Hargreaves, 1995].

### 1.2.2 High-speed streams

Another type of solar wind structures affecting space weather, the solar high-speed streams are created by the fast flow of solar wind plasma along open magnetic field lines. These regions of open magnetic flux are called *coronal holes*, and they are almost always present on the Sun, especially at high latitudes [Lowder *et al.*, 2017]. During the declining phase of the solar cycle, coronal holes from the polar regions tend to migrate to lower latitudes, and the resulting high-speed streams of solar wind may flow in the ecliptic plane [Kojima and Kakinuma, 1987]. When the fast solar wind (typically 500–800 km/s) is preceded by a slower stream (200–400 km/s), this creates a compression region characterised by high IMF magnitude, solar wind density and pressure, called *corotating interaction region* [Richter and Luttrell, 1986]. The terminology came from the observation that such structures often show a  $\sim 27$  day recurrence, corresponding to the solar rotation period near the equator, which implies that a same coronal hole (and hence, the resulting high-speed stream) may persist during several solar rotations. Figure 1.5 shows the IMF magnitude and the solar wind velocity, density and dynamic pressure measured near the Earth during a high-speed stream event from March 2007. The transition from the slow solar wind stream to the high-speed stream contains several local peaks of solar wind pressure and density, in this particular example. The east-west component of the solar wind velocity (not shown here) generally exhibits a sign reversal at the transition from slow to fast solar wind, defining the stream interface [Kavanagh *et al.*, 2012].

Even though the coronal mass ejections may represent the most violent type of disturbances, it is estimated that the corotating interaction regions and following high-speed streams are more geoeffective, i.e., are more efficient in depositing energy into the ionosphere, even though the energy input into the planetary environments is generally smaller than for CMEs [Turner *et al.*, 2009]. It is suggested that this may arise from solar wind driving differences between these two types of disturbances, and also possibly from saturation in the magnetospheric response to CMEs. As a result, a CIR may sometimes result in a deposition of energy into the ionosphere comparable to what a CME could produce [Turner *et al.*, 2009].

At Mars, CIRs are more often associated with shocks than at 1 AU [Gosling and Pizzo, 1999]. They are an important cause for atmospheric erosion [Hara *et al.*, 2011].

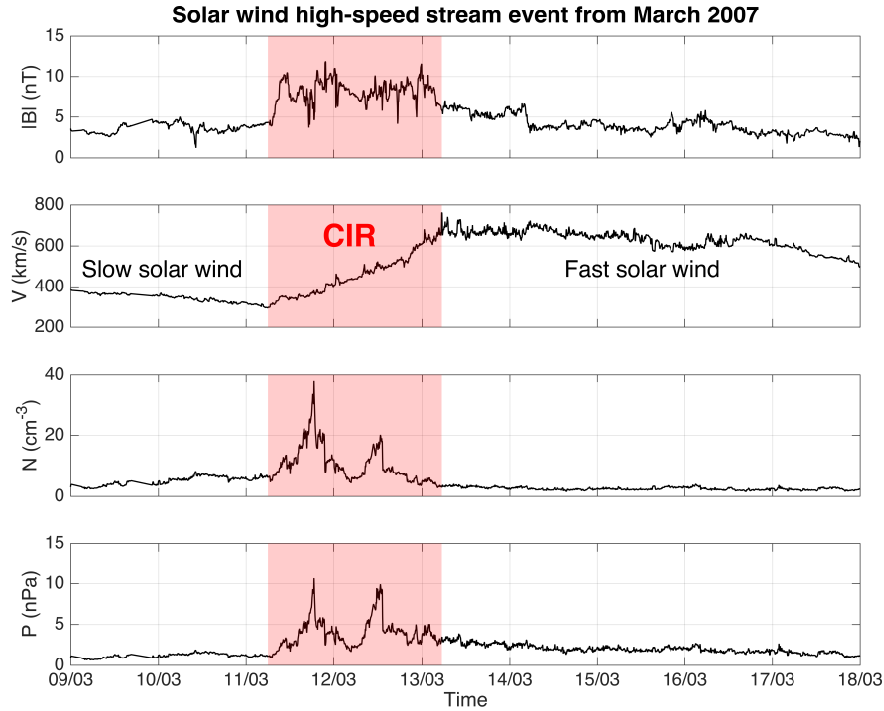


**Figure 1.5.** Main solar wind parameters measured near the Earth during a high-speed stream event from March 2007. From top to bottom: IMF magnitude, solar wind velocity, solar wind density, and solar wind dynamic pressure. The data come from the ACE satellite and were retrieved from the OMNI data base [King and Papitashvili, 2005].

### 1.3 Magnetospheres

The speed of sound in the solar wind is about 60 km/s near the Earth's orbit [Hundhausen, 1995], and the Alfvén speed is respectively of the order of 50 km/s [Hargreaves, 1995]. This means that the solar wind is supersonic and super-Alfvénic. Therefore, its encounter with obstacles such as planets with an intrinsic magnetic field or surrounded by an ionised atmosphere results in the formation of a bow shock ahead of the obstacle. At Earth, the nose of the bow shock is located about 14 Earth radii ( $R_E = 6371$  km) upstream from the centre of the Earth [Burgess, 1995]

#### 1.3.1 Terrestrial magnetosphere

Since the Earth has an intrinsic magnetic field, the solar wind cannot penetrate the terrestrial environment and is deviated. The boundary between the geomagnetic field and the solar wind is defined as the surface where their magnetic pressures are equal; it is called the *magnetopause*. The volume inside the magnetopause is the geomagnetic

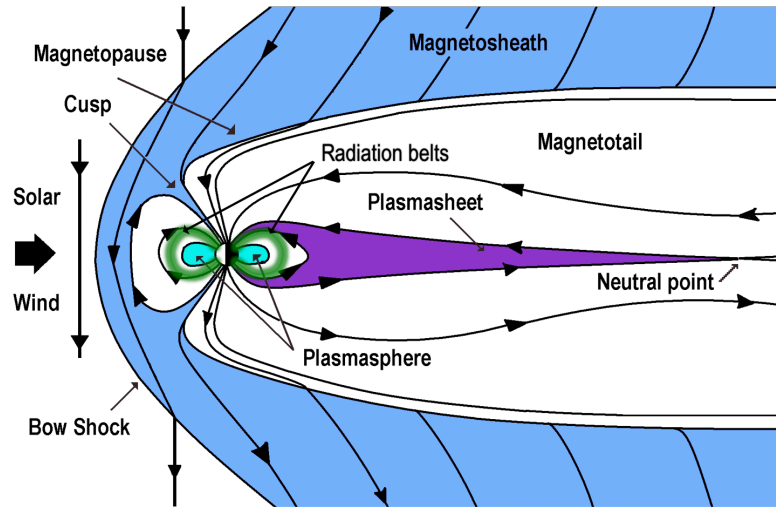


**Figure 1.6.** Schematic diagram of the terrestrial magnetosphere in the plane containing the Sun–Earth and the north–south directions. The Sun is located to the left of the sketch.

cavity, or the terrestrial magnetosphere. Figure 1.6 gives a schematic illustration of the terrestrial magnetosphere and its main regions. The region located between the magnetopause and the bow shock is called the magnetosheath (in blue in the figure). It consists of solar wind particles forming turbulent plasma, heated by the bow shock crossing. It may play an important role in the coupling of the solar wind and the terrestrial environment by introducing non-linearities in electric field and Poynting flux transfer between the bow shock and the magnetopause [Pulkkinen *et al.*, 2016].

The existence of the solar wind flow modifies the structure of the geomagnetic field. From a nearly dipolar field, it becomes compressed on the dayside and stretched on the nightside. On the dayside, the magnetopause position along the Sun–Earth line is most of the time  $\sim 10 R_E$  from the centre of the Earth; yet it may be moved to  $\sim 8 R_E$  when the IMF has a strong southward component [Shue *et al.*, 2001], and even closer to the Earth following the arrival of a CME [e.g., Huttunen *et al.*, 2002]. On the nightside, geomagnetic field lines are stretched to form the so-called magnetotail, whose extension is estimated to reach beyond several hundreds of Earth radii [Slavin *et al.*, 1983].

On the dayside, two neutral points directly connect the magnetosphere to the Earth; they are called *polar cusps*. The polar cusps are mapped to the Earth’s surface near magnetic noon at a geomagnetic latitude ranging from  $72^\circ$  to  $79^\circ$ , depending on solar wind conditions, and there is one cusp in each hemisphere [Newell *et al.*, 1989]. They correspond to holes in the magnetic shield of the Earth, through which the solar wind may directly enter the geomagnetic cavity.

Polewards from the cusp, a region of open geomagnetic field lines mapped to the distant magnetotail forms the (northern or southern) lobe. Its mapping into the ionosphere is called the *polar cap*, which extends from the geomagnetic pole to about  $71\text{--}74^\circ$  geomagnetic latitude on the nightside, and to about  $71\text{--}80^\circ$  geomagnetic latitude on the dayside [Vorobjev and Yagodkina, 2010]. These variations depend on geomagnetic activity: the polar cap expands during active times and shrinks during quiet times.

Between the northern and southern lobes, a region of geomagnetic field lines which are closed but significantly stretched inside the magnetotail is called the *plasma sheet* (in purple in Figure 1.6). Geomagnetic field lines reverse directions in the so-called neutral sheet, in which a dawn-to-dusk current flows in association with the magnetic field reversal. In the equatorial plane, the earthward boundary of the plasma sheet lies at  $7 R_E$ , approximately, and this region has extensions to the dawn and dusk sides of the magnetosphere [Hargreaves, 1995].

Closer to the Earth, the plasmasphere (in cyan) is a region of denser, colder plasma, corotating with the Earth. It consists mostly of protons and electrons which are diffused from the ionosphere during the day but remain trapped along the closed geomagnetic field lines. It extends from the  $\text{O}^+/\text{H}^+$  transition altitude in the topside ionosphere to about  $4\text{--}5 R_E$  in the equatorial plane [Brekke, 2012]. While plasmaspheric particles have low energies ( $\sim 1$  eV), a population of relativistic-energy ( $> 1$  MeV) electrons and protons was discovered by J. A. van Allen in the late 1950s [van Allen and Frank, 1959]. Most of the time, there are two radiation belts (in green, yet not shown separately from each other): the inner belt ( $1.3 < L < 2.5$ ) and the outer belt ( $4 < L < 7$ ), where  $L$  is the McIlwain parameter which defines a set of geomagnetic field lines by the distance of their intersection with the equatorial plane to the centre of the Earth, given in Earth radii [McIlwain, 1961]. The inner radiation belt consists of protons and electrons which are formed by the decay of neutrons created by cosmic rays. The outer radiation belt is mostly made of electrons injected from the outer magnetosphere. One of the main loss processes in the outer radiation belt involves precipitation of particles into the ionosphere, which will be described in 1.4.3.

Several large-scale current structures are present in the magnetosphere. At the magnetopause, because of the deflection of solar wind ions and electrons in opposite directions, an eastward current flows, called the *Chapman-Ferraro current*. It is connected on the nightside to the tail current system discussed above. In addition, in the inner magnetosphere, charged particles are trapped along closed geomagnetic field lines and bounce between two mirroring points. Trapped particles, in addition to their bounce motion, are subject to the gradient–curvature drift, which is oriented eastwards for electrons and westwards for ions. This results in a current flowing westwards close to the equatorial plane, called the *ring current*. This current is mostly carried by protons of moderate energy (3–50 keV) [Frank, 1967]. Besides these currents flowing perpendicularly to the geomagnetic field, field-aligned currents, also called *Birkeland currents*, exist. The main field-aligned current structures have the shape of an imperfect oval around the geomagnetic pole. The poleward part

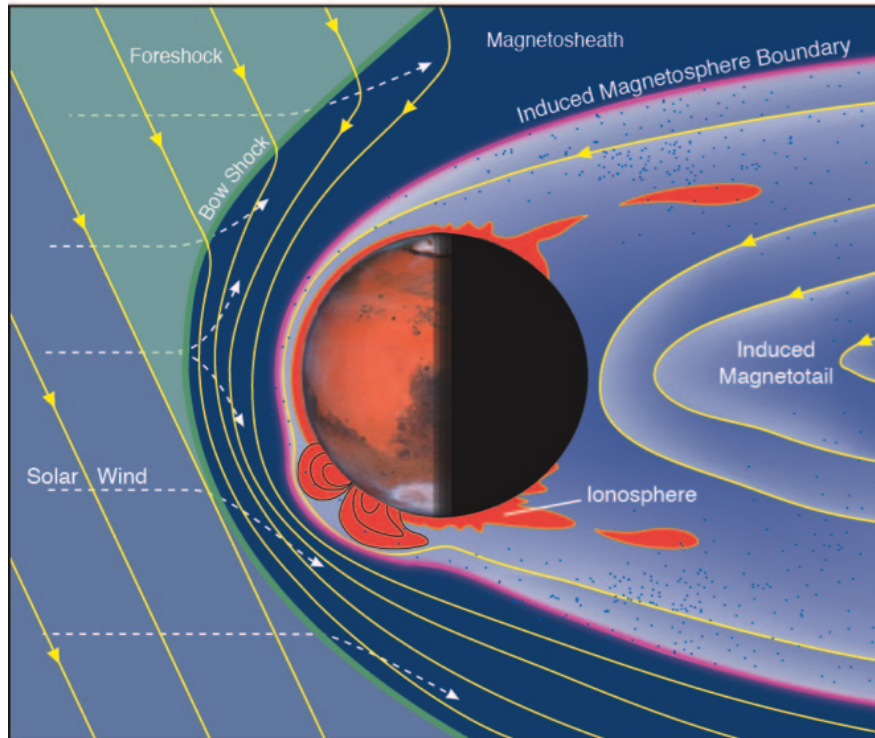


**Figure 1.7.** Schematic diagram of the Martian induced magnetosphere. (reproduced from *Brain et al.* [2017]; courtesy from Fran Bagenal and Steve Bartlett)

of this oval consists of so-called region-1 currents, which flow upwards on the dusk side and downwards on the dawn side. The equatorward part of the oval consists of currents flowing downwards on the dusk side and upwards on the dawn side, called region-2 currents [*Iijima and Potemra*, 1978]. Upward currents are generally carried by precipitating electrons (see section 1.4.3), while downward currents are mostly carried by cold ionospheric electrons with an upward motion [e.g., *Aikio et al.*, 2004]. The magnetospheric current systems have their closure in the ionosphere, more precisely in the  $E$  region.

### 1.3.2 Martian induced magnetosphere

Contrary to the Earth, Mars no longer has an intrinsic magnetic field, presumably because its core became solid when cooling about four billion years ago [*Valdivia-Silva et al.*, 2013]. Presently, only a remanent crustal magnetic field can be measured close to the surface [*Acuña et al.*, 1999]. Its intensity may reach a few hundred nT at 200 km altitude [*Lewis and Simons*, 2012].

However, interactions of the Martian environment with the incoming solar wind lead to the formation of an induced magnetosphere. Its structure, as is understood from observations up to this date, is presented in Figure 1.7. Because the Martian dayside ionosphere is dense enough (see Figure 1.4), as a conducting medium it represents an obstacle for the solar wind. Therefore, like for the Earth, a bow shock is formed ahead of Mars. Its nose lies at 1.5–1.6 Martian radii ( $R_m = 3396$  km at the equator) from the centre of the planet [Trotignon *et al.*, 1993]. The shock defines the Martian magnetosheath, downstream, which is a turbulent plasma made of solar wind particles.

The planetward boundary of the magnetosheath is called the *magnetic pileup boundary* (also named the induced magnetosphere boundary [e.g., Bertucci *et al.*, 2011]), which is characterised by a sharp magnetic field gradient, a decrease in plasma temperature and turbulence, and an increase in the electron density. As its name tells, this boundary also represents the limit of the magnetic pileup region, where the solar wind magnetic field lines are draped around the Martian ionosphere and stretched into a structure analogous to a magnetotail. The draping takes place in or close to the plane containing the solar wind velocity and IMF vectors as seen from Mars [Crider *et al.*, 2004]. The presence of crustal fields, especially in the southern hemisphere, modifies the shape and location of the dayside magnetic pileup boundary, rising its average altitude locally from 600 km to 800 km and preventing it from reaching below 600 km altitude even in the case of extreme solar wind conditions [Fränz *et al.*, 2006].

It was found by Yeroshenko *et al.* [1990] that the Martian magnetotail contains two lobes, separated by a neutral sheet. In one lobe, the magnetic field is pointing Sunwards, while in the other one it is pointing anti-Sunwards. The polarity of the tail lobes is determined by the IMF component perpendicular to the solar wind velocity. In the central region of the tail, heavy ions (principally  $O^+$  ions) are accelerated from 0.1 to a few keV through energy transfer from the solar wind magnetic field to the Martian plasma [Nagy *et al.*, 2004]. The tailward ion flow in this plasma sheet is an important ion loss process occurring at Mars.

## 1.4 Planetary environments and solar wind interactions

### 1.4.1 Reconnection and convection

One of the main large-scale forms of interaction existing between the solar wind and the Earth is magnetospheric convection. It is driven by mostly two processes: magnetic reconnection and viscous interactions. Viscous interactions at the flanks of the magnetosphere are likely to take place continuously, the fast-flowing solar wind transferring energy to the magnetosphere by processes analogous to friction [Axford and Hines, 1961]. Magnetic reconnection may occur when two magnetic field lines of opposite directions are compressed close to each other. The magnetic field of the Earth is oriented northwards in the equatorial plane, as the magnetic pole located in the southern hemisphere is presently a north pole (see Figure 1.6). When the IMF north-south component  $B_z$  is negative (i.e., southwards), this leads to a configuration in which reconnection may occur with the Earth's magnetic field at

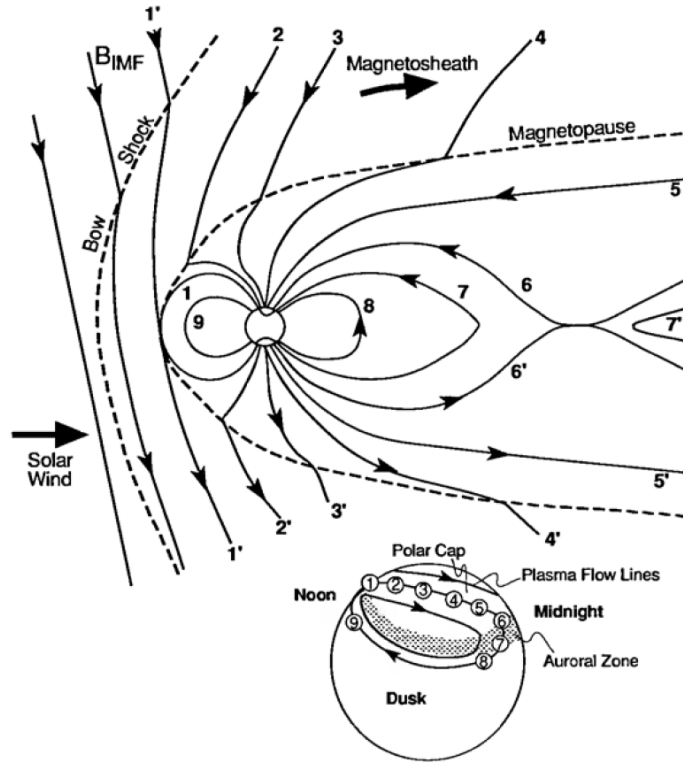


**Figure 1.8.** Magnetospheric and polar cap convection driven by magnetic reconnection with southward IMF. (reproduced from *Hughes* [1995])

the dayside magnetopause. This reconnection drives a magnetic field and plasma convection in the magnetosphere, whose principle is exposed in Figure 1.8.

When the IMF reconnects at the dayside magnetopause, the newly formed magnetic field lines have one footpoint in the Earth's ionosphere and another one at the Sun (line numbered 1 in the figure). As the solar wind propagates, this field line is dragged towards the nightside, initiating the convection (2-4). As the magnetic field piles up in the magnetotail (5), it gets compressed in the vicinity of the neutral sheet. This leads to the emergence of suitable conditions for magnetic reconnection to take place in the tail (6). The newly closed geomagnetic field line being stretched, magnetic tension makes it migrate towards the Earth to retrieve a configuration closer to a dipolar field line (7-8). On the anti-Sunward side, the reconnected IMF line is expelled away from the Earth (7'). Finally, a return flow takes place and brings dipolar field lines from the nightside to the dayside (9) [*Hughes*, 1995].

The magnetospheric plasma flow creates a dawn-to-dusk electric field, which is mapped in the polar cap due to very high conductivity along the magnetic field lines. Hence, the polar cap plasma is set in motion by the presence of this dawn-to-dusk

electric field and the geomagnetic field. This creates the  $\mathbf{E} \times \mathbf{B}$  plasma convection discussed in section 1.1.2.1. In this situation (Figure 1.8, bottom), the ionospheric plasma is transported from noon to midnight across the geomagnetic pole, and a return flow takes place along the auroral oval (see section 1.4.3) on the dawn and dusk sides, leading to a two-cell convection pattern. This idealised steady-state magnetospheric convection pattern is known as the *Dungey cycle*, after *Dungey* [1961]. In the general case, convection patterns are more complex, since the  $B_y$  (east-west) component of the IMF also has an influence on the locations where reconnection may occur, and on the asymmetry of the convection pattern observed in the polar cap [e.g., *Papitashvili et al.*, 1989]. In addition, steady state is seldom reached in reality, and reconnection occurs at different rates at the dayside magnetopause and in the magnetotail [*Cowley and Lockwood*, 1992].

Under northward IMF conditions, even more complex convection patterns take place. Reconnection cannot take place near the equatorial plane at the dayside magnetopause in this case, but the solar wind may reconnect with open field lines from the tail lobes, polewards from the cusp, creating two reverse convection cells in the polar cap [*Dungey*, 1963; *Burch and Reiff*, 1985; *Förster et al.*, 2008]. In this situation, two weak convection cells with normal sense of circulation are also created by viscous interactions equatorward from the reverse cells [*Axford and Hines*, 1961].

#### 1.4.2 Geomagnetic storms and magnetospheric substorms

Ground-based instruments enable the observation of signatures of the geomagnetic field perturbations and the estimation of the severeness of the disturbance. Magnetometers (see section 2.1.2) located at low geomagnetic latitudes observe a deflection in the horizontal component of the geomagnetic field. This is the signature of a *geomagnetic storm*, which is related to an intensification of the ring current (see section 1.3.1) when particles are injected into the inner magnetosphere. Geomagnetic disturbances are often quantified using geomagnetic indices, which are generally derived from a network of magnetometer stations. Geomagnetic storm severeness has historically been estimated using the  $D_{st}$  (“disturbance storm time”) index [*Sugiura*, 1964; *Sugiura et al.*, 1991], which is calculated using magnetometer data from four low-latitude stations and has 1-hour time resolution. More recently, the SYM-H index [*Iyemori*, 1990] has been preferred, as it provides an equivalent measure of storm severeness but with a higher (1 min) time resolution [*Wanliss and Showalter*, 2006]. A geomagnetic storm typically follows three phases: short-lived (a few hours) increase in the SYM-H index, followed by a decrease during up to one day, and slow recovery to pre-storm values during several days [*Hargreaves*, 1995]. The  $D_{st}$  or SYM-H minimum value typically reaches -30 to -50 nT during moderate storms, and may reach under -250 nT during extreme storms [*Gonzalez et al.*, 1999].

In the disturbed magnetosphere, a phenomenon known as *substorm* takes place, often repeatedly during a geomagnetic storm – even though a substorm may also occur outside of geomagnetic storm periods. It is initiated by magnetic reconnection in the magnetotail, at a distance from the Earth which is still debated. Recent results estimate it to be of the order of  $18 R_E$  [*Sergeev et al.*, 2012]. Three main

phases are distinguished: the growth, expansion, and recovery phases. In the ionosphere, a substorm has various manifestations that can be observed with ground-based instruments, such as precipitation of particles leading to auroral displays and electron density enhancements in the *D*, *E* and *F* regions, ionospheric currents, and plasma heating. During a typical substorm, the growth phase is associated with quiet auroral arcs in the east-west direction moving equatorwards [Motoba *et al.*, 2015]. Then, during the expansion phase, one of the arcs becomes active and moves polewards; the auroral oval becomes broader. The recovery phase manifests itself as a quietening of the auroral activity, with arcs becoming dimmer and slowly drifting back equatorwards [Akasofu, 1964]. Substorm activity is often measured using the AE (“auroral electrojet”) index, which is calculated using magnetometers located in the auroral oval [Davis and Sugiura, 1966]. It is sensitive to the intensification of auroral-zone currents such as the eastward electrojet in the evening sector, the westward electrojet in the early-morning sector, and the substorm electrojet flowing westwards in the midnight sector. Typical values for AE during a substorm are of the order of hundreds of nanoteslas but may exceed 1000 nT [Akasofu, 1981].

### 1.4.3 Particle precipitation

In the Earth’s ionosphere and upper atmosphere, a major space weather manifestation is the precipitation of particles of solar wind and magnetospheric origins. As was mentioned in section 1.3.1, in the inner magnetosphere, trapped particles bounce between two mirroring points. The mirroring point location for a given particle is determined by its *pitch angle* in the equatorial plane, which is the angle made by the velocity vector of the particle with the magnetic field direction.

If a particle has a pitch angle small enough to allow its mirroring point to be in the upper atmosphere, then it will lose its energy through collisions with atmospheric constituents. This is referred to as *particle precipitation*. A trapped particle may precipitate after interaction with very-low-frequency (VLF, several kHz) waves [e.g., Thorne *et al.*, 2010]. Indeed, VLF waves may change the energy anisotropy (and hence the pitch angle) of particles and scatter them into the *loss cone*, which is the ensemble of pitch angles associated with a mirroring point inside the upper atmosphere. In addition, during substorms, as reconnection takes place in the magnetotail, particles from the plasma sheet may be accelerated and directly precipitate into the ionosphere without spending any time as trapped particles bouncing between mirror points.

In the magnetosphere, several source regions for precipitating particles exist. On the dayside, the cusp region is of particular interest, as solar wind particles may directly precipitate into the upper atmosphere. In addition, when magnetic reconnection occurs at the dayside magnetopause, solar wind particles may follow the newly open field lines down to the ionosphere. Cusp precipitation is generally of high flux and rather low energy [Nilsson *et al.*, 1994]. On the nightside, reconnection in the plasma sheet may also lead to precipitation, which is of higher energy (typically 1–20 keV) [Newell *et al.*, 1996]. The equatorward extent of the region of precipitation associated to the plasma sheet typically reaches about 65° geomagnetic latitude [Winningham *et al.*, 1975]. The region where most auroral precipitation occurs forms

an approximate oval, including the cusp on the dayside and the plasma sheet on the nightside, called the auroral oval. At lower latitudes, regions mapped to the radiation belts may have precipitation of relativistic ( $> 1$  MeV) electrons. Precipitation is one of the main loss mechanisms for the radiation belts.

Depending on their energies, precipitating particles penetrate more or less deeply into the upper atmosphere. For instance, electrons with energies under 1 keV are stopped above 150 km altitude, while 300 keV electrons may reach down to 70 km altitude [Rees, 1963]. The energy deposition may take various forms: ionisation of neutral species, dissociation of molecules, or excitation of neutrals or ions. Each of these forms leads to observable consequences: enhancement of the electron density in the  $F$ ,  $E$  and  $D$  regions (see also 2.1.3), ozone destruction [e.g., Turunen *et al.*, 2016], and auroral emissions.

### Pulsating aurora

Auroral emissions at Earth are often studied at three wavelengths in the visible part of the electromagnetic spectrum. Atomic oxygen, when excited, may produce photons at 630.0 nm (red) and 557.7 nm (green), and the  $N_2^+$  ion is responsible for the 427.8 nm (blue) emission. Other emission lines exist in the visible and ultraviolet domains, e.g., hydrogen emissions at 656.3 nm ( $H_\alpha$ ) and 486.1 nm ( $H_\beta$ ) [Brekke, 2012].

One type of auroral precipitation which is studied more specifically in this thesis (Paper III) is so-called *pulsating aurora*. This type of aurora is particularly common during the morning hours in the equatorward part of the auroral oval [Kvifte and Pettersen, 1969]. It takes the form of auroral patches, arcs or arc segments whose brightness is modulated, exhibiting “on” and “off” times. Typical pseudo-periods for those modulations range from a few seconds to about 20 s, with a mean value of  $8 \pm 2$  s [Johnstone, 1978]. A given pulsating structure generally behaves independently from the other ones, having its own period. In addition, the pulsating period is not necessarily regular [Humbert *et al.*, 2016]. An additional internal modulation during “on” times, at about 3 Hz, has been reported [Sandahl *et al.*, 1980; Nishiyama *et al.*, 2016]. Besides, an east-west drift of the pulsating structures is generally observed at up to 1 km/s [Davis, 1978].

Pulsating aurora is currently a topic of high scientific interest, as it is suspected that this might be an important source of energy input into the upper and middle atmosphere [Turunen *et al.*, 2016]. The mechanism behind the modulation of the precipitating electron flux is still subject to speculation. It is generally accepted that the loss-cone scattering of electrons is due to interaction with VLF waves near the equatorial plane of the magnetosphere [Jaynes *et al.*, 2013]. More precisely, bursts of chorus waves, which are electromagnetic waves with frequencies of a few kHz propagating along the magnetic field lines, are often cited as likely candidates [Nishimura *et al.*, 2011; Miyoshi *et al.*, 2015a]. These waves are known to be responsible for low-energy (a few keV) electron precipitation such as those producing diffuse aurora [Thorne *et al.*, 2010]. Some theories suggest that chorus wave activity in the magnetosphere is controlled by magnetic field intensity modulation by Pc4–5

geomagnetic pulsations, or by plasma density fluctuations [Li *et al.*, 2011a,b], which could lead to the variations in auroral emission observed during pulsating aurora.

#### 1.4.4 Some aspects of Mars interactions with the solar wind

Besides the draping of the interplanetary magnetic field which creates an induced magnetosphere, the solar wind also interacts with Mars in ways that are to some extent analogous to phenomena observed at Earth. Mars Global Surveyor observations suggesting that magnetic reconnection occurs between the Martian crustal fields and the draped IMF were reported by Halekas *et al.* [2009]. The presence of crustal fields results in the existence of cusps, through which the solar wind electrons may directly access the planetary surface [Dubinin *et al.*, 2008]. These magnetic structures are of small size compared to the terrestrial cusps, hence the regions where direct penetration of solar wind particles is possible are also very localised. Recent observations of ultraviolet auroral emission in the vicinity of these “mini magnetospheres”, mostly located in the southern hemisphere, suggest that accelerated solar wind electrons may excite atmospheric species, in a similar way as particle precipitation does at Earth [Brain and Halekas, 2012]. In addition, diffuse auroral emission was also reported in the northern hemisphere, down to about 60 km altitude [Schneider *et al.*, 2015]. The current understanding is that the discrete type of aurora, on closed field lines, may be compared to nightside oval aurora at Earth, while the diffuse aurora, on open field lines, could be seen as analogous to polar rain aurora at Earth, associated to the precipitation of low-energy ( $< 1$  keV) electrons in the terrestrial polar cap.

In addition, recent results from the Mars Global Surveyor mission indicate that reconnection also takes place in the Martian magnetotail. Eastwood *et al.* [2012] reported the observation of a chain of three magnetic flux ropes, i.e., twisted magnetic structures containing a flowing current, in the magnetotail current sheet. These flux ropes were probably generated by instabilities during a magnetic reconnection event. It is believed that such processes may play an important role in plasma transport in the Martian environment.

Furthermore, Withers *et al.* [2016] have investigated the effect of solar wind dynamic pressure fluctuations on the Martian environment. They found that higher dynamic pressure results in magnetosphere compression, magnetosheath heating, and topside ionosphere compression.



## Chapter 2

# Instrumentation

This doctoral work essentially relies on space physics data measured by ground-based instruments located in Finland and satellites orbiting at low altitude around the Earth and Mars. Solar wind data were provided by the Advanced Composition Explorer (ACE) satellite and stored in the OMNI data base [King and Papitashvili, 2005]. This chapter presents the instrumentation and data sets which are used in the publications.

### 2.1 Ground-based instruments

The locations of the ground-based instruments described in this section are indicated on a map of Fennoscandia given in Figure 2.1.

#### 2.1.1 Sodankylä ionosonde

Ionosondes (ionospheric sounders) are radar systems designed to measure parameters related to the electron density profile in the ionosphere. They were first introduced in the 1930s after an idea from *Breit and Tuve* [1925]. Their principle relies on radio wave propagation in a plasma, which is governed by the Appleton–Hartree equation [Lassen, 1927; Appleton, 1932] giving the refractive index  $n$  in a plasma for a radio wave of angular frequency  $\omega$ . In the ionosphere, the refractive index is given by

$$n^2 = 1 - \frac{X}{1 - jZ - \frac{Y^2 \sin^2 \theta}{2(1 - X - jZ)} \pm \left( \frac{Y^4 \sin^4 \theta}{4(1 - X - jZ)^2} + Y^2 \cos^2 \theta \right)^{1/2}}, \quad (2.1)$$

where  $X = (\omega_0/\omega)^2$ ,  $Y = \omega_c/\omega$ ,  $Z = \nu_e/\omega$ , and  $\theta$  is the angle between the magnetic field and the wave vector [Hargreaves, 1995]. In these dimensionless ratios,

$$\omega_0 = \sqrt{\frac{N_e e^2}{m_e \varepsilon_0}} \quad (2.2)$$

is the plasma frequency, with  $N_e$  the electron density,  $e$  the elementary charge,  $m_e$  the electron mass, and  $\varepsilon_0$  the permittivity of free space. The electron gyrofrequency

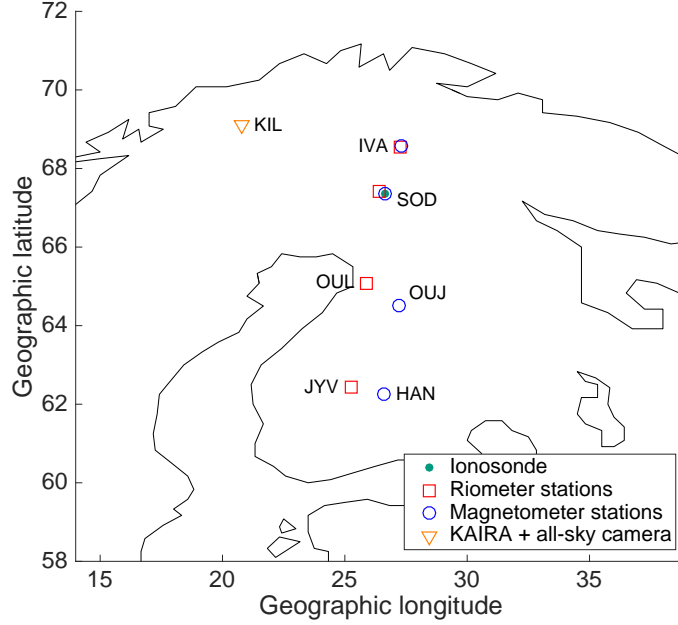


**Figure 2.1.** Map of Fennoscandia with the locations of the ground-based instruments used in this thesis. The station names and McIlwain  $L$ -parameter values are as follows: KIL (Kilpisjärvi,  $L = 6.2$ ), IVA (Ivalo,  $L = 5.7$ ), SOD (Sodankylä,  $L = 5.2$ ), OUL/OUJ (Oulu/Oulujärvi,  $L = 4.5$ ), JYV/HAN (Jyväskylä/Hankasalmi,  $L = 3.8$ ).

$\omega_c = eB/m_e$  is a function of the magnetic field magnitude  $B$ , and  $\nu_e$  is the electron collision frequency. The  $\pm$  sign in equation (2.1) defines two modes of propagation which correspond to different polarisations for the radio wave.

The Sodankylä ionosonde (geographic  $67.4^\circ\text{N}$ ,  $26.6^\circ\text{E}$ ;  $L = 5.2$ ) routinely performs vertical soundings of the ionosphere, transmitting every minute a radio signal sweeping in frequency from 0.5 to 16 MHz [Kozlovsky *et al.*, 2013; Enell *et al.*, 2016]. When the radio wave encounters a region of the ionosphere such that the real part of the refractive index is equal to zero, it is reflected back towards the ground. For each transmitted frequency, one may measure the time delay between the moment when the wave is transmitted and the moment when its echo is detected by the ionosonde receiver. The frequency sweep enables one to produce an image called ionogram (see Figure 2.2), in which the virtual height of reflection is given as a function of the frequency. The virtual height  $h'$  of reflection is given by  $h' = \Delta t/2c$ , where  $\Delta t$  is the time delay between transmission and reception of the radio wave at a given frequency, and  $c$  is the speed of light in vacuum. The height is called “virtual” as it is obtained assuming that the radio wave propagates at speed  $c$  along its whole path, which is not true, especially near the altitude of reflection. Ionospheric soundings from the ground provide information up to the main electron density peak, since frequencies able to

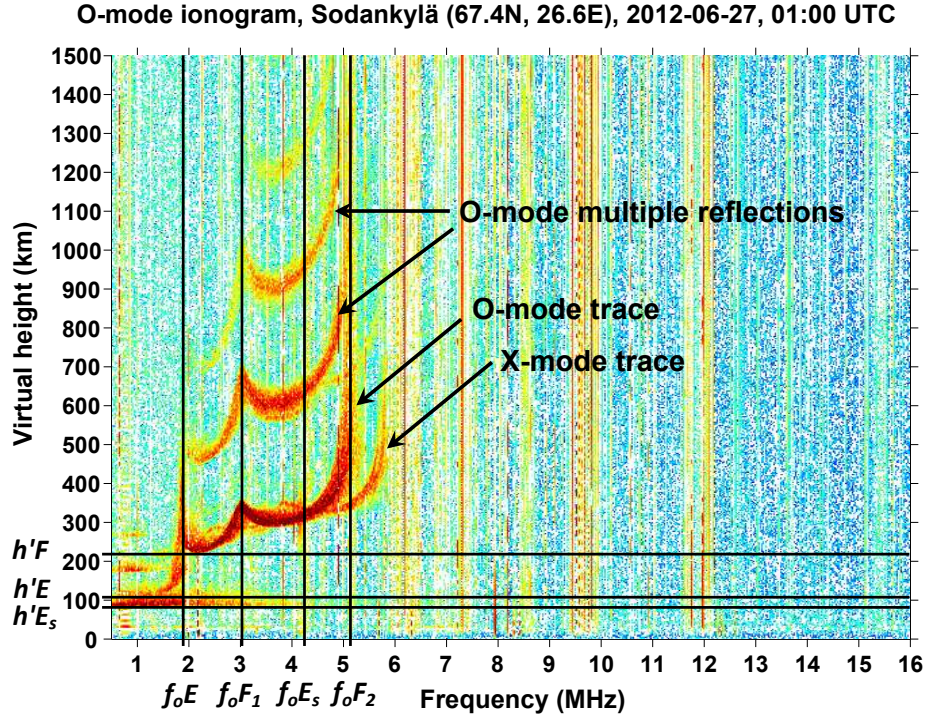


**Figure 2.2.** Typical summer-time scaled ionogram from the Sodankylä ionosonde.

propagate beyond the peak cannot be reflected by the topside ionosphere, where the electron density is below the peak electron density.

Neglecting the electron collisions ( $Z = 0$ ), and under the approximation that the radio wave propagates nearly along the geomagnetic field (quasi-longitudinal approximation), the refractive index is zero for the + sign in equation (2.1) when  $X = 1$ . This is the so-called ordinary (O) mode and it then reflects at an altitude where the wave frequency is equal to the plasma frequency. The refractive index is also zero for  $X = 1 \pm Y$ , corresponding to the extraordinary (X) mode.

To derive parameters of the ionospheric layers, the O-mode traces are scaled on ionograms. The main scaled parameters are so-called critical frequencies of ionospheric layers ( $f_oE$ ,  $f_oE_s$ ,  $f_oF_1$ , and  $f_oF_2$ ) and their virtual heights ( $h'E$ ,  $h'E_s$ , and  $h'F$ ). The O-mode critical frequencies are directly related to the electron peak density in the ionospheric layers. For instance, the  $F$ -peak electron density is given from equation (2.2) by

$$N_m^F = 4\pi^2 m_e \epsilon_0 (f_oF_2)^2 / e^2. \quad (2.3)$$

In the  $E$  region, two critical frequencies and virtual heights are generally scaled. The parameters called  $f_oE$  and  $h'E$  correspond to the “normal”  $E$  region produced by

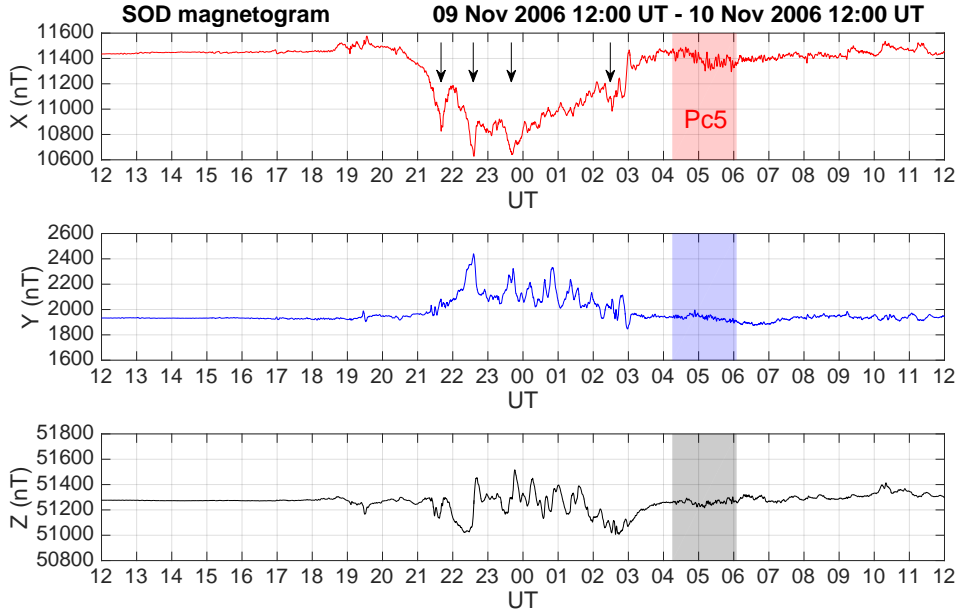


**Figure 2.3.** Magnetogram from the Sodankylä magnetometer. The geomagnetic field, especially the  $X$  component, shows substorm signatures between 21 and 03 UT (indicated with arrows), and Pc5 pulsations around 05 UT.

photoionisation of the neutral atmosphere by solar EUV radiation. In addition, it is very common at high latitudes to also observe an O-mode trace in the  $E$ -region altitude range related to ionisation due to particle precipitation (see section 1.4.3). This corresponds to what has been called a “sporadic  $E$  layer”, even though the nature of such a layer differs from what is usually referred to by this terminology, namely thin layers of metallic ions which may form at midlatitudes [Axford, 1963]. In Sodankylä, ionogram scaling is done manually at 30-min resolution for critical frequencies and at 1-h resolution for virtual heights. In Paper I, two parameters derived from Sodankylä ionospheric soundings are used,  $f_oF_2$  and  $f_oE(s) = \max(f_oE, f_oE_s)$ , with 1-h resolution.

### 2.1.2 IMAGE magnetometers

Geomagnetic measurements are the oldest observations made in Sodankylä Geophysical Observatory (SGO). The first magnetogram was recorded on 1 January 1914, and since then the magnetic field of the Earth has been almost continuously measured in Sodankylä. Currently, the main SGO magnetometer is a digital fluxgate magnetometer, operating at 2 Hz sampling rate. The vector geomagnetic field is projected along three components:  $X$  (northwards),  $Y$  (eastwards), and  $Z$  (towards the centre of the Earth). Baselines are controlled by absolute geomagnetic field observations, which are performed once a week.

Nowadays, the Sodankylä magnetometers belong to the IMAGE (International Monitor for Auroral Geomagnetic Effects) magnetometer network [Tanskanen, 2009]. IMAGE comprises 35 stations in Fennoscandia and in the Baltic countries, spanning from Svalbard to the border between Lithuania and Poland, and maintained by 10 institutes from northern and eastern European countries. The Principal Investigator (PI) institute of IMAGE is the Finnish Meteorological Institute.

Ground-based magnetometer data can be used to study ionospheric currents, e.g., the auroral electrojets, and ultra-low frequency (ULF) waves, which appear as continuous or irregular geomagnetic pulsations. When the periods of such pulsations range between 150 and 600 s (frequencies comprised between 1.7 and 6.7 mHz), continuous pulsations are called Pc5 and irregular ones are called Pi3 (Pi2 in some publications) [Saito, 1978; Hughes, 1994]. Figure 2.3 shows a 24 h magnetogram from the Sodankylä magnetometer. The  $X$  component shows several dips between 21 and 03 UT, corresponding to substorm signatures induced by westward electrojets flowing in the ionosphere, as well as Pc5 pulsations around 05 UT. Disturbances are also visible in the  $Y$  and  $Z$  components.

In Paper I, data from the  $X$  component of the Sodankylä magnetometer are used to study electrojet enhancements during high-speed stream events. In Paper II, magnetometer data from four IMAGE stations (Ivalo, Sodankylä, Oulujärvi and Hankasalmi) are used to study ULF wave activity in the magnetosphere during high-speed stream events.

### 2.1.3 SGO riometer chain and KAIRA

When particles with energies greater than a few tens of keV precipitate into the ionosphere, they may produce ionisation down to the  $D$  region (i.e., below 90 km altitude). This additional ionisation in the  $D$  region may be measured using riometers (relative ionospheric opacity metres), as was first done by *Shain* [1951].

Riometry is based on the measurement of the power of cosmic radio noise reaching the ground. When cosmic noise originating from a radio source in the sky propagates through the ionosphere, part of its power is absorbed. The absorption in the ionosphere can be derived by isolating the imaginary part of the complex refractive index given by equation (2.1). Under the quasi-longitudinal approximation, the absorption along a path noted  $l$  can be calculated in decibels (dB) by

$$A_{dB} = 4.6 \times 10^{-5} \int \frac{N_e \nu dl}{\nu^2 + (\omega \pm \omega_c \cos \theta)^2}, \quad (2.4)$$

with  $N_e$  the electron density,  $\nu$  the electron collision frequency,  $\omega$  the angular frequency of the radio wave,  $\omega_c$  the electron gyrofrequency, and  $\theta$  the angle between the direction of propagation and the magnetic field vector [Hargreaves, 1969].

In practice, the absorption is negligible in the  $F$  and  $E$  regions of the ionosphere, since the electron collision frequency is very small. Therefore, cosmic noise absorption is affected mainly by the electron density in the  $D$  region. The power of the radio signal observed by a riometer therefore depends on the distribution of radio sources in the

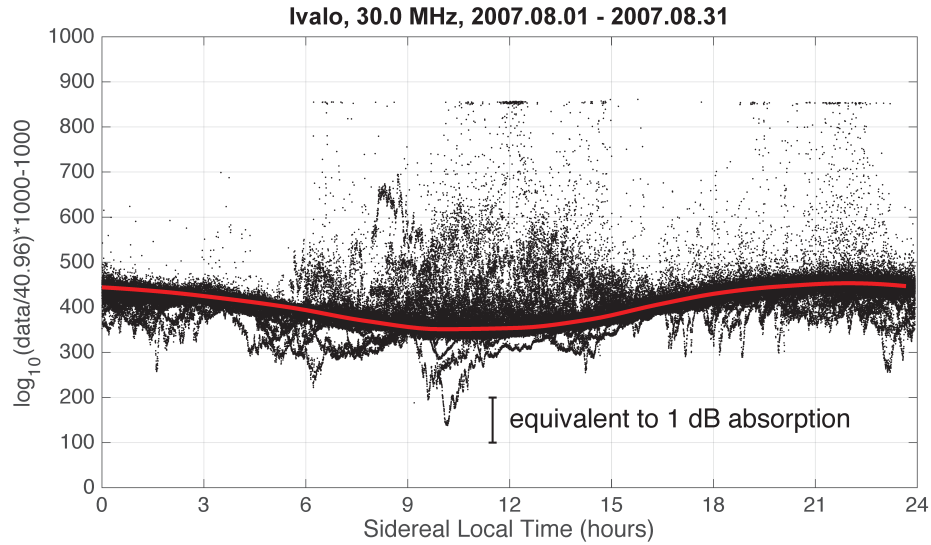


**Figure 2.4.** Example of QDC definition to obtain cosmic noise absorption, using riometer data from Ivalo ( $L = 5.7$ ) in August 2007. The measured power at 30 MHz (black dots; in an arbitrary logarithmic scale) during the whole month is plotted as a function of sidereal local time and the quiet-day curve (red line) for this period is defined manually.

sky, on the electron density profile in the  $D$  region, and on the observed frequency. If a riometer observes along a fixed beam, then a same radio source will periodically enter the beam as the Earth rotates. This implies that, under quiet ionospheric conditions with similar solar irradiance daily variations, the cosmic radio noise power measured by a riometer is periodic, the period corresponding to the duration of a sidereal day ( $T_{\text{sid}} = 86\,164$  s). However, if the  $D$ -region ionisation is enhanced compared to a quiet day, e.g., because of energetic particle precipitation or X-rays originating from a solar flare, then a greater amount of cosmic noise power is absorbed. By subtracting the time series of the cosmic radio noise power measured by a riometer from a so-called quiet-day curve (QDC), one may estimate the cosmic noise absorption (CNA) due to enhanced  $D$ -region electron density. In publications, CNA generally refers to what should strictly-speaking be called “excess cosmic noise absorption compared to a quiet day”.

Figure 2.4 illustrates the QDC definition used at SGO, with the example of the QDC defined for the station located in Ivalo for the month of August 2007. The QDC is estimated manually by superposing the measured power (black dots) during several days over a time period equal to  $T_{\text{sid}}$ . This enables one to identify the shape of the signal which would be measured on each sidereal day during that period of the year if there were no disturbances of any kind. This shape gives the quiet-day curve (red line). Then, for a given day, the measured radio noise power is subtracted to the QDC to obtain absorption, which is expressed in decibels. One may notice in Figure 2.4

that the measured power sometimes exceeds the QDC (e.g., between 6 and 15 sidereal local time, SLC). This may be due to solar radio emissions or to radio interferences originating from human-made systems. On the other hand, several downward spikes may also be observed under the QDC in the figure (e.g., near 10 SLC). These are cosmic noise absorption signatures, which are the data of geophysical interest.

It should be noted that QDCs vary according to the period of the year. Indeed, different radio noise sources appear in the antenna field of view throughout a year, as a consequence of the tilt of the Earth rotation axis. In addition, non-geophysical factors, such as the accumulation of snow on the antenna elements in winter, may affect the riometer beam shape. Therefore, QDCs must be regularly redefined to process the riometer data.

The CNA data used in Paper II come from four riometers of the SGO chain (Ivalo, Sodankylä, Oulu, and Jyväskylä), covering auroral and subauroral latitudes ( $L$ -shells between 3.8 and 5.7). The instruments are narrow-band wide-beam ( $60^\circ$ ) riometers, observing at frequencies near 30 MHz (32.4 MHz for Jyväskylä). CNA data is available at 1 min time resolution, but in Paper II it is used with 15 min resolution.

### Multibeam riometry with KAIRA

The Kilpisjärvi Atmospheric Imaging Receiver Array (KAIRA) is a multipurpose instrument which is located in Kilpisjärvi ( $L = 6.2$ ). Its construction was completed in 2013, and it has been operated since then by SGO and the University of Oulu (UOulu). It consists of two arrays of passive antennas measuring signals in the very-high frequency (VHF) range: the low-band antenna (LBA,  $f = 8\text{--}80$  MHz) array and the high-band antenna (HBA,  $f = 110\text{--}270$  MHz) array; each array consists of 48 antenna elements [McKay-Bukowski *et al.*, 2015]. KAIRA is based on the Low-Frequency Array (LOFAR) technology, whose applications include interplanetary scintillation, radio astronomy and solar radio emission studies, interferometric riometry, among other topics.

In this thesis, the LBA array of KAIRA is used as a multibeam riometer. In Paper III, cosmic noise absorption data from KAIRA at 1 s resolution are compared to auroral emission data from the Kilpisjärvi all-sky camera during a pulsating aurora event.

#### 2.1.4 Kilpisjärvi All-Sky Camera

Auroral emissions can be studied with optical instruments such as all-sky cameras or photometers. In Kilpisjärvi, the Finnish Meteorological Institute has operated an all-sky camera since 1978. Initially, the instrument was a film camera, but since 2007 an electron multiplying charge coupled device (EMCCD) digital camera has been in use in Kilpisjärvi [Sangalli *et al.*, 2011].

All-sky images are produced routinely during the dark season, which lasts from early September to mid-April. Optical filters are used to measure the auroral emissions in the visible part of the spectrum: 630.0 nm (red, atomic oxygen), 557.7 nm (green,

atomic oxygen), and 427.8 nm (blue, molecular nitrogen ion). A calibration of the camera is performed using an intercalibrated integrating sphere light source in Sodankylä at the beginning of each season [Brändström *et al.*, 2012]. Each all-sky camera image contains  $512 \times 512$  pixels and, when projected at 100 km altitude, corresponds to a field of view of about 600 km in diameter.

In Paper III, a pulsating aurora event is studied with optical data from the Kilpisjärvi all-sky camera. The data consist of blue-line (427.8 nm) images taken every 2 s.

## 2.2 Satellites

### 2.2.1 Mars Express

The Mars Express spacecraft was launched by the European Space Agency (ESA) on 2 June 2003. It was successfully inserted into orbit around Mars on 25 December 2003 and made its first measurements in January 2004. The payload consists of seven instruments to study the Martian atmosphere, ionosphere, surface and subsurface.

In this thesis, data from the Mars Express Radio Science Experiment (MaRS) were used. This instrument performs five types of radio science experiments to study the Martian surface, atmosphere, ionosphere, gravity anomalies, but also the solar corona and Phobos, one of the Martian natural satellites [Pätzold *et al.*, 2004].

Papers IV and V are based on data from the MaRS radio-occultation experiment. Radio-occultation is a technique enabling to retrieve neutral temperature and density profiles in the atmosphere and electron density profiles in the ionosphere by probing the planetary environment with super high frequency (SHF, 3–30 GHz) radio waves. It relies on the dependency of the refractive index in the atmosphere and ionosphere on neutral and electron densities. Altitude-dependent inhomogeneities in these parameters are therefore responsible for a slight bending of the radio waves transmitted between Mars Express and a ground station at Earth in a near-occultation configuration, which may be estimated by measuring accurately the frequency of the radio wave observed by the receiver. The principle of radio-occultation and the methods which may be used to retrieve the atmospheric and ionospheric profiles are presented in more detail in section 3.2.

Although its data are not used in this doctoral thesis, it is worth mentioning that another instrument onboard the Mars Express satellite is able to study the Martian ionosphere. This instrument is called Mars Advanced Radar for Subsurface and Ionospheric Sounding (MARSIS) [Jordan *et al.*, 2009; Orosei *et al.*, 2015]. It is able to perform topside ionospheric soundings, using the same principle as ground-based ionosondes (see section 2.1.1) and transmitting frequencies from 0.1 to 5.5 MHz. However, since in the case of MARSIS the soundings are performed from above the Martian environment, only the upper part of electron density profiles (above the main peak) can be retrieved with this technique [Gurnett *et al.*, 2008].

### 2.2.2 NOAA/POES

Paper II uses measurements of energetic particle fluxes from the Polar Orbiting Environmental Satellites (POES) from the National Oceanic and Atmospheric Administration (NOAA). The first satellites of the POES family were launched in the 1980s, but during 2006–2008 (when the data used in Paper II were collected) four spacecraft were in operation: NOAA-15, NOAA-16, NOAA-17, and NOAA-18. Each satellite has a nearly polar orbit which is Sun-synchronous. Their altitudes are close to 850 km, and the orbital period is 102 min (corresponding to about 14.1 orbits per day).

The Space Environment Monitor (SEM-2) set of instruments contains the Medium Energy Proton and Electron Detector (MEPED) which measures fluxes of protons and electrons within three energy channels ( $> 30$  keV,  $> 100$  keV, and  $> 300$  keV) [Evans and Greer, 2000]. The instrument consists of two telescopes, one oriented away from the centre of the Earth ( $0^\circ$  telescope), the other one pointing antiparallel to the spacecraft velocity vector ( $90^\circ$  telescope). The  $0^\circ$  telescope measures precipitating particle fluxes, whereas the  $90^\circ$  telescope measures trapped particle fluxes. Yet, Rodger *et al.* [2013] reported that the precipitating  $> 30$  keV electron flux may be underestimated, especially during periods of low geomagnetic activity. This is related to the fact that the  $0^\circ$  telescope does not view the bounce loss cone in its entirety. In addition, contamination issues have also been known to affect the measurements of electron fluxes [Asikainen and Mursula, 2013]. However, in this thesis, only a qualitative analysis of measurements of trapped and precipitating electron fluxes in the  $> 30$  keV and  $> 100$  keV energy channels during one event was performed in Paper II. Therefore, these issues are not critical for this work.

### 2.2.3 ACE

The Advanced Composition Explorer (ACE) satellite was launched by the National Aeronautics and Space Administration (NASA) in 1997. One of its primary goals is to continuously measure solar wind parameters upstream from the Earth. ACE is located at the L1 Lagrangian point [Chiu *et al.*, 1998], about  $1.5 \times 10^6$  km from the Earth in the direction of the Sun.

In this thesis, data from two instruments onboard ACE have been used. Interplanetary magnetic field (IMF) measurements are provided by the ACE Magnetic Field Experiment (MAG) [Smith *et al.*, 1998], while solar wind density and velocity come from the ACE Solar Wind Electron Proton Alpha Monitor (SWEPAM) [McComas *et al.*, 1998]. The solar wind parameters measured by these instruments at L1 are propagated to the Earth's bow shock nose and incorporated into the OMNI database [King and Papitashvili, 2005], from which they were downloaded for the studies presented in Papers I and II.



## Chapter 3

# Methods

### 3.1 Superposed epoch analysis

#### 3.1.1 Classical version

When studying the response of a system to a perturbation, the observed or measured parameters are subject to variations depending on other phenomena which are not necessarily related to the perturbation itself. This, alongside random noise associated with, e.g., measurement uncertainties, may lead to the parameters exhibiting features which significantly depart from the “typical” response during an isolated event.

One possible way to overcome this difficulty is to adopt a statistical approach by studying the behaviour of the system during many events. In this thesis, the chosen statistical method is the superposed epoch analysis. This method was first used by *Chree* [1913] in a study relating sunspot area and geomagnetic field disturbances observed at Kew Observatory in London; hence, it is also sometimes referred to as the Chree analysis.

The principle of the superposed epoch analysis is as follows. First, several events corresponding to the studied phenomenon need to be identified. Then, for each event, a “zero epoch”, corresponding to the reference instant in the event timeline, is defined. This enables the superposition of the events with respect to a characteristic feature of the perturbation, such as CIR stream interface (see section 1.2.2) [e.g., *Denton et al.*, 2009; *Kavanagh et al.*, 2012], solar flare [e.g., *Belov et al.*, 2008], or substorm onset [e.g., *Milan et al.*, 2009]. Finally, statistical properties are extracted from the physical parameters of the events as a function of time relative to the zero epoch. These statistical properties may be mean values, median values, standard deviation, quartiles, deciles, etc., but more complex estimators may also be used [*Samson and Yeung*, 1986]. In this thesis, we use the median values alongside the upper and lower quartiles, for their higher robustness to outliers compared to the mean and standard deviation [e.g., *Rousseew and Croux*, 1993]. The superposed epoch analysis is applied to study effects of solar wind high-speed streams on ionospheric parameters in Papers I and II, and to characterise pulsating aurora signatures in Paper III.

One critical aspect in the superposed epoch analysis is the choice of the zero epochs. *Ilie et al.* [2008] have shown that, depending on the selected criterion to determine the zero epochs, different features may be more or less prominent in the response of the studied parameters of the system. This implies that the zero epoch selection must be adapted to the physical constraints related to the studied parameters.

### 3.1.2 Phase-locked version

In Paper I, the superposed epoch analysis is used to study the response of the critical frequencies in the  $F$  and  $E$  regions,  $f_oF_2$  and  $f_oE(s)$ , to the arrival of a solar wind high-speed stream (HSS) at the bow shock. Since solar irradiance is the main source of ionisation in the ionosphere,  $f_oF_2$  and  $f_oE(s)$  are strongly dependent on the local time, and also exhibit seasonal variations. In addition, it is known that geomagnetic disturbances have very different effects in different magnetic local time (MLT) sectors – for instance, substorms are typically a nightside phenomenon. Therefore, it may be expected that effects of a HSS-driven disturbance on the  $F$  and  $E$  regions ionisation differ according to the MLT (and hence to the local time). On the other hand, the zero epochs used to study the effect of high-speed streams on the ionosphere are selected based on criteria on solar wind parameters (see section 4.1), which implies that the local time in Sodankylä at the zero epoch instant is different for each high-speed stream event. Therefore, the classical version of the superposed epoch method is not suitable to study the response of local  $f_oF_2$  and  $f_oE(s)$  to HSSs.

A possible solution is to shift the zero epochs so that they all correspond to a same MLT location of the Sodankylä ionosonde. This modified version of the method was called *phase-locked superposed epoch analysis* and is presented in Paper I. The phase locking was achieved by choosing a reference MLT to which the original zero epochs for the critical frequencies were moved. One downside of this approach is that it creates a  $\pm 12$  h ambiguity in the actual instant of arrival of the HSS at the terrestrial bow shock. This means that transient phenomena taking place within 12 h from the zero epoch are very likely to be averaged out through the statistical processing. In the work presented in Paper I, this is not so critical since the aim is to study effects over timescales of several days.

To illustrate the benefits of the phase-locked superposed epoch analysis on pseudo-periodic signals, a simple example is presented in Figure 3.1. We consider a sequence of  $N$  time series of an arbitrary parameter whose variations mostly follow a cosine function. The signal corresponding to event  $n$  is given as a function of time  $t$  by

$$s_n(t) = [1 + r_n(t)] \cos(t + \varphi_n) [1 + R(t)], \quad (3.1)$$

where  $r_n(t)$  is a function which, at each time  $t$ , returns a random number sampled from the standard uniform distribution on  $] -0.5, 0.5[$ ,  $\varphi_n$  is a random phase for a given signal sampled from the standard uniform distribution on  $] -\pi, \pi[$ , and  $R$  is the ramp function defined by  $R(t) = \max(t, 0)$ . In other words,  $(s_n)$  is a sequence of noisy cosine functions amplified for  $t > 0$  and with different phases. The ramp function  $R$  is chosen to represent the effect in each of the time series that we wish to reveal in the superposed epoch analysis. Figure 3.1 shows a comparison of the results obtained

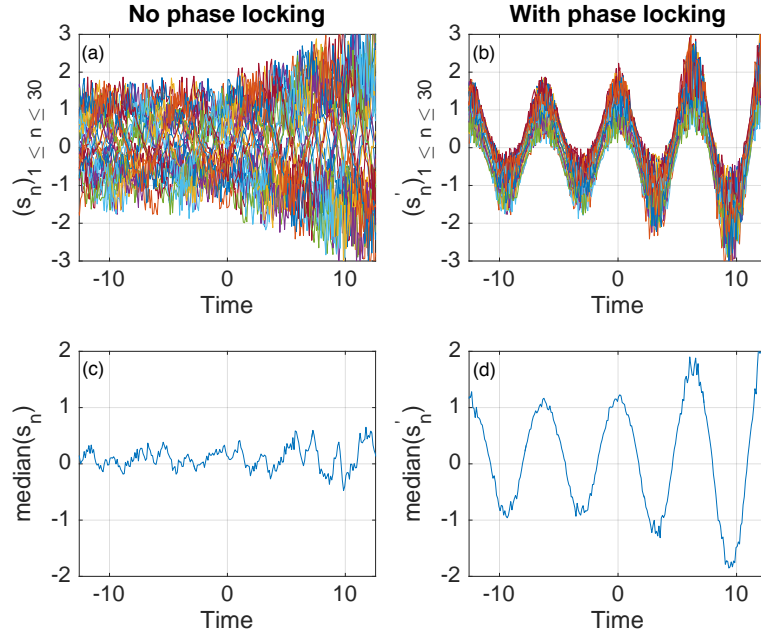


**Figure 3.1.** Comparison of the standard (left panels) and phase-locked (right panels) versions of the superposed epoch method. (top panels) Time series representing 30 events following cosine functions with noise, amplified for  $t > 0$ . (bottom panels) Median values of the time series calculated using the superposed epoch method. Units are arbitrary.

with the classical and phase-locked versions of the superposed epoch analysis, with  $N = 30$ . Panel (a) shows the time series of the 30 signals, and panel (c) shows the median values obtained with the classical superposed epoch method. Features visible in the median curve are essentially noisy, and the effect of the ramp function after the zero epoch does not appear clearly.

In the phase-locked version of the superposed epoch analysis, the time series corresponding to each event are shifted in time in such a way that they are all in-phase. This was achieved by adding a suitable phase, comprised between  $-\pi$  and  $+\pi$ , to each signal so that the phase-locked signals each have a zero phase at  $t = 0$ . The shifted signals, noted  $s'_n$ , are shown in panel (b) of the figure. As a result, the curve corresponding to their median values, shown in panel (d), is very close to a cosine function amplified at  $t > 0$ , thus revealing the ramp function effect after the zero epoch. Yet, there is an uncertainty of  $\pm\pi$  in the “physical” zero epoch times, and it is therefore not possible to determine with precision when the signal amplification starts.

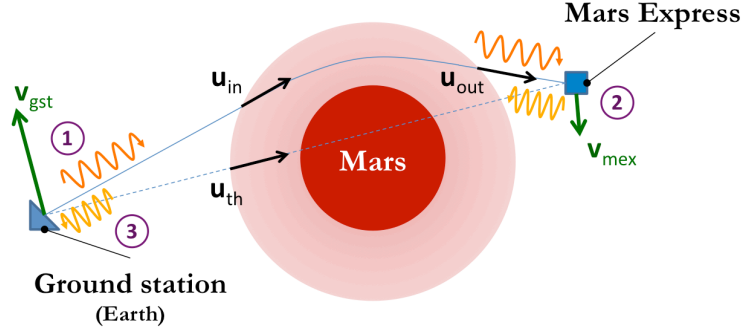


**Figure 3.2.** Setup of a radio-occultation experiment between the Earth and Mars (not to scale; modified from Figure 4 of Paper IV).

One may understand this simulation as an analogy to the analysis of  $f_oF_2$  time series during 30 high-speed stream events.

## 3.2 Radio-occultation

### 3.2.1 Principle

Radio-occultation is a technique enabling to measure atmospheric and ionospheric parameters by making use of radio wave propagation in the planetary environment. It is based on the accurate measurement of the Doppler shift experienced by a radio wave transmitted by a spacecraft and received either by a ground station or by another satellite after propagating through the planetary environment in a nearly tangential direction. At Earth, radio-occultation experiments generally involve two satellites, and may provide estimations of the  $F$ -region peak electron density [e.g., *Shubin et al.*, 2013]. At other planets, however, such experiments are made between a spacecraft orbiting the planet and a ground station on Earth. This method has been used since the 1960s with the Mariner IV and V satellites orbiting around Mars [*Kliore and Tito*, 1967] and Venus [*Cain et al.*, 1967], respectively. Later on, radio-occultation was also used to study the atmospheres of Saturn and Titan, using data from Voyager 1 [*Lindal et al.*, 1983] and Cassini [*Schinder et al.*, 2011a,b]. At the time of writing this thesis, proposals to use the Juno (NASA) and JUICE (Jupiter Icy Moons Explorer, ESA) spacecraft to perform radio-occultation experiments to study Jupiter and its main satellites (Io, Europa, Callisto, and Ganymede) have been investigated [*Gurvits et al.*, 2013; *Phipps and Withers*, 2017].

In this thesis, radio-occultation data from the MaRS experiment onboard Mars Express are used. The setup of the radio-occultation experiments is illustrated in Figure 3.2. A ground station on Earth transmits a signal in the X band (at 7.1 GHz) towards the spacecraft orbiting around Mars (step 1 in the figure). Upon reception of the signal, Mars Express transmits it back, after applying a transponder ratio (equal

to 880/749; see Pätzold *et al.* [2004]) to the received frequency (step 2). The ground station finally measures the frequency of the radio wave when it receives it; it is then close to 8.4 GHz (step 3). This is what is called a two-way radio-occultation experiment, with an uplink and a downlink wave, which is the setup considered in this thesis.

The relative motion between Mars Express and the Earth creates a Doppler shift between transmission and reception of the wave. If the propagation takes place in vacuum, this Doppler shift can be accurately predicted, provided the motions of transmitter and receiver are known in a reference frame. However, when Mars Express is at a location close to occultation by Mars (as seen from the Earth), the radio wave propagates through the Martian atmosphere and ionosphere, where the refractive index  $n$  is locally given by

$$n = 1 + \bar{\kappa}N_n - \frac{e^2}{8\pi\epsilon_0 m_e} \frac{N_e}{f^2} \quad (3.2)$$

where  $\bar{\kappa}$  is the refractive volume of Mars neutral atmosphere, equal to  $1.804 \times 10^{-29} \text{ m}^3$  for a well-mixed atmosphere consisting of 95.3% CO<sub>2</sub>, 2.7% N<sub>2</sub>, and 1.6% Ar [Hinson *et al.*, 1999; Tellmann *et al.*, 2013], which is valid up to about 120 km altitude [Izakov, 2007]. Other parameters in equation (3.2) are as follows:  $N_n$  is the neutral density,  $e$  is the elementary charge,  $\epsilon_0$  is the permittivity of free space,  $m_e$  is the electron mass,  $N_e$  is the electron density, and  $f$  is the frequency of the radio wave.

Since  $N_n$  and  $N_e$  vary according to the location, the refractive index is not homogeneous in the Martian environment. When propagating through the planetary environment, the radio wave therefore undergoes a small deviation, and it is thus received by the spacecraft with an arrival direction (noted  $\mathbf{u}_{\text{out}}$  in the figure) slightly different from the straight-line direction of the Earth (noted  $\mathbf{u}_{\text{th}}$ ). This results in a small difference in the frequency shift compared to the prediction, which is generally called *frequency residual*. The order of magnitude of the frequency residual is about 0.1 Hz when probing the ionospheric peak region, and up to a few Hz when probing the lower atmosphere. Since the contributions of the neutral atmosphere and of the ionosphere to the refractive index are of opposite signs, the frequency residual also has a different sign depending on whether the radio wave propagates predominantly in the ionosphere or in the neutral atmosphere. Through several measurements of the frequency residual as Mars Express gets closer and closer to full occultation, deeper and deeper regions of the Martian atmosphere and ionosphere are probed, thus enabling to get a frequency residual profile as a function of altitude. This corresponds to the measurement containing information on atmospheric and ionospheric physical parameters given by MaRS.

### 3.2.2 Data analysis

Traditionally, radio-occultation data is analysed using an inversion method detailed in Fjeldbo *et al.* [1971]. However, this method is based on two strong assumptions on the planetary environment: (i) the neutral atmosphere and the ionosphere are fully decoupled, and (ii) the physical properties of the planetary environment follow

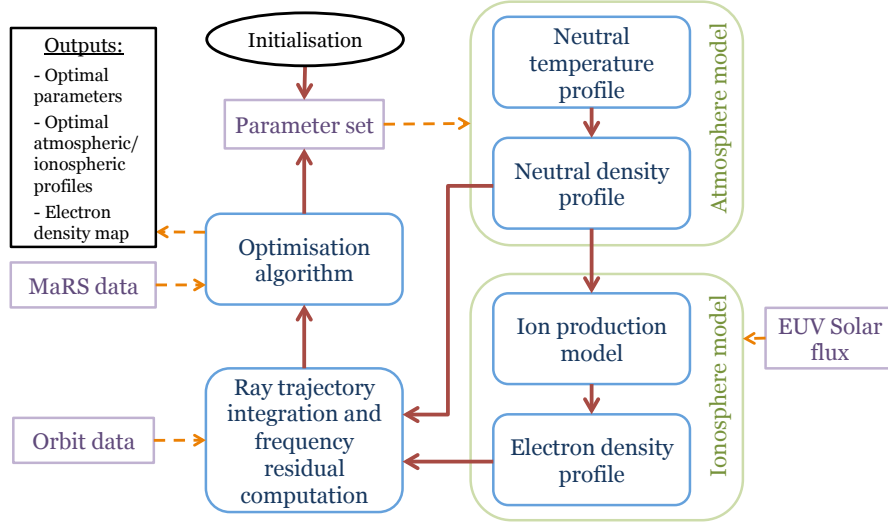


**Figure 3.3.** Overview of the radio-occultation model (coloured version of Figure 1 from Paper IV).

a spherical symmetry. Therefore, the inversion is theoretically not applicable to the analysis of radio-occultation data measured close to the twilight terminator of Mars, where the electron density is subject to strong gradients depending on the solar zenith angle.

The data analysis approach proposed in Papers IV and V aims at avoiding those two assumptions by making a direct simulation of the radio wave propagation in a modelled Martian environment during a radio-occultation experiment. An overview of the model is given in Figure 3.3.

First, the Martian environment is modelled (green blocks corresponding to atmosphere and ionosphere models) as a function of initial parameters (e.g., neutral temperature values at reference altitudes, reference densities for neutral species). In particular, the neutral temperature profile is parametrised to follow a general pattern (overall decrease from ground to mesosphere, and exponential thermospheric profile as given by *Bates [1959]*) which can be adjusted. The neutral density profiles are then obtained under the assumption of hydrostatic equilibrium (see section 1.1.1). Three neutral constituents are considered in this model:  $\text{CO}_2$ ,  $\text{O}$ , and  $\text{N}_2$ . Once the neutral atmosphere is determined, the ionosphere is constructed by photoionisation of the neutral species by the EUV and X-ray solar flux, combined with the computation of the chemical equilibrium. Three ion species are produced by photoionisation:  $\text{CO}_2^+$ ,  $\text{O}^+$ , and  $\text{N}_2^+$ . Their primary and secondary production rates are calculated using a kinetic model for suprathermal electrons based on the one used in the TRANSCAR model [*Robineau et al., 1996; Lilensten and Blelly, 2002; Marchaudon and Blelly, 2015*] and using the  $F_{10.7}$  index as a proxy for solar activity at the time of the experiment. This index corresponds to a daily measurement of the 10.7 cm radio flux performed

at the Penticton Radio Observatory (Canada) at local noon [Tapping, 2013]. Two more ion species are produced by chemistry:  $\text{O}_2^+$  and  $\text{NO}^+$ . The model considers a set of 13 chemical reactions which are summarised in Table 1 of Paper IV. The ionospheric model computes the chemical equilibrium for the five ion densities and 13 reactions, given the background neutral atmosphere and the ion production rates. It is important to note that this approach, in which the planetary environment is modelled as described, avoids both assumptions required to use the classical inversion method, as the obtained ionosphere is based on the neutral atmosphere and the local solar zenith angle. This enables one to couple the neutral and ionised media and to have an asymmetric ionosphere.

The neutral and electron densities being defined, it is therefore possible to calculate the refractive index at any point within the Martian environment – within the limits of the model and its assumptions – by using equation (3.2). Given the orbit data of the ground station on Earth, Mars, and the Mars Express spacecraft, it is then possible to simulate the radio-occultation experiment by computing the ray trajectories followed by the uplink and downlink radio waves. For each ray, the frequency residual is computed, and a frequency residual profile is obtained by simulating several rays as the occultation takes place. This step corresponds to the blue block in the bottom-left-hand corner of Figure 3.3.

Finally, the simulated frequency residual profile is compared to the profile actually measured by Mars Express. The difference between these two enables one to define a cost function to be minimised through an optimisation algorithm adjusting the parameters which were used to construct the Martian neutral atmosphere (blue “Optimisation algorithm” box in Figure 3.3). Here, the Levenberg–Marquardt algorithm [Marquardt, 1963] is used for the optimisation. Once the algorithm has converged, it is then possible to use the optimal parameters to compute the neutral temperature, neutral density, ion and electron density profiles in the region probed by the radio-occultation experiment (black “Outputs” box in the top-left-hand corner of Figure 3.3).



## Chapter 4

# Results

### 4.1 Effects of solar wind high-speed streams on the high-latitude ionosphere of the Earth

Papers I and II present the results of two studies on the effects of solar wind high-speed streams in the auroral and subauroral ( $L = 3.8\text{--}5.7$ ) ionosphere. While Paper I focuses essentially on the response of the  $F$  region and also addresses  $E$ -region aspects, Paper II deals with effects on cosmic noise absorption, taking place in the  $D$  region.

For these two studies, 95 high-speed stream events were detected during 2006–2008 based on the behaviour of solar wind parameters measured by the ACE satellite. The criteria for high-speed stream event detection were as follows:

- (i) sharp increase in the interplanetary magnetic field (IMF) magnitude;
- (ii) within 48 h after the IMF increase, solar wind speed enhancement up to at least 500 km/s;
- (iii) two consecutive events must be separated by at least four days.

Sharp increases in the IMF magnitude were detected by calculating the time derivative of the IMF strength using a central differencing scheme (criterion (i)). Around each data point  $i$  at  $\Delta t = 5$  min resolution, the time derivative was estimated by

$$\frac{dB}{dt} \hat{=} \frac{1}{4\Delta t} \left[ \frac{1}{3}(B_{i+3} + B_{i+2} + B_{i+1}) - \frac{1}{3}(B_{i-1} + B_{i-2} + B_{i-3}) \right]. \quad (4.1)$$

Taking into account 6 data points in the derivative estimation provided a value smoothed over timescales of the order of 20–30 min. When this derivative exceeded an empirically determined threshold of 0.1 nT/min, the corresponding times were taken as high-speed stream event candidates, which were then tested according to criteria (ii) and (iii). Each high-speed stream event candidate was then validated by a visual check of the solar wind parameter behaviours, and a few false events were removed during this process. The zero epochs for the superposed epoch analysis were defined as the times of sharp IMF magnitude increases. They were occasionally adjusted during the visual check when they did not correspond to the most suitable IMF increase for

the event, i.e., when they did not take place at the time when the solar wind speed starts to increase.

#### 4.1.1 Solar wind driving

The solar wind driving during high-speed stream events is presented in Figure 4.1. Solar wind parameters and geomagnetic indices have been analysed using the superposed epoch method in its classical version. Days relative to the zero epoch are referred to as days D-2, D-1, D1, D2, D3, D4, and D5, as indicated in panel (c). The sharp IMF increase at the zero epoch in panel (a) corresponds to the time when the solar wind speed starts to increase gradually in panel (b). After reaching a maximum (600 km/s for the median curve) at the end of day D2, the speed decreases slowly and has not yet reached pre-event values at the end of day D5. The solar wind dynamic pressure peaks near the zero epoch and decreases promptly during day D1, as can be seen in panel (c). Panel (d) shows the Akasofu epsilon parameter [Akasofu, 1979], which is a coupling function used as a proxy for energy input from the solar wind into the magnetosphere given by

$$\varepsilon = \frac{4\pi}{\mu_0} V B^2 L_0^2 \sin^4 \left( \frac{\theta}{2} \right), \quad (4.2)$$

with  $\mu_0$  the vacuum permeability,  $V$  the solar wind speed,  $B$  the IMF magnitude,  $\theta$  its clock angle in the plane perpendicular to the Sun–Earth direction, and  $L_0 \simeq 7R_E$ . In Figure 4.1, the Akasofu epsilon parameter exhibits an enhancement principally during day D1, and to a lesser extent during day D2.

The large-scale geomagnetic response to high-speed stream driving is given in panels (e) and (f), where the AE and SYM-H indices are respectively shown. A geomagnetic storm signature can be seen in SYM-H data, with a negative deflection starting around the zero epoch and reaching lowest values during day D1. Median values of SYM-H do not decrease beyond -30 nT, which corresponds to moderate geomagnetic storms. The recovery phase, however, takes more than five days, which is in agreement with results by, e.g., *Gonzalez et al.* [1999]; *McPherron and Weygand* [2006]; *Denton and Borovsky* [2012]. Substorm activity, on the other hand, is enhanced from the zero epoch time until the end of day D3, and continues during days D4 and D5, yet with quite low intensity.

#### 4.1.2 Overview of ionospheric response to high-speed streams

An overview of the observations reported in Papers I and II and their suggested interpretations is given in Figure 4.2. The layout schematically presents the effects observed in each ionospheric region in different MLT sectors (outer circles), and chains of causal links connect high-speed stream characteristics (boxes in the grey inner circle) to these ionospheric responses, according to the interpretations proposed in the papers. The figure will be described in more detail as these observations and interpretations are presented in the following subsections.

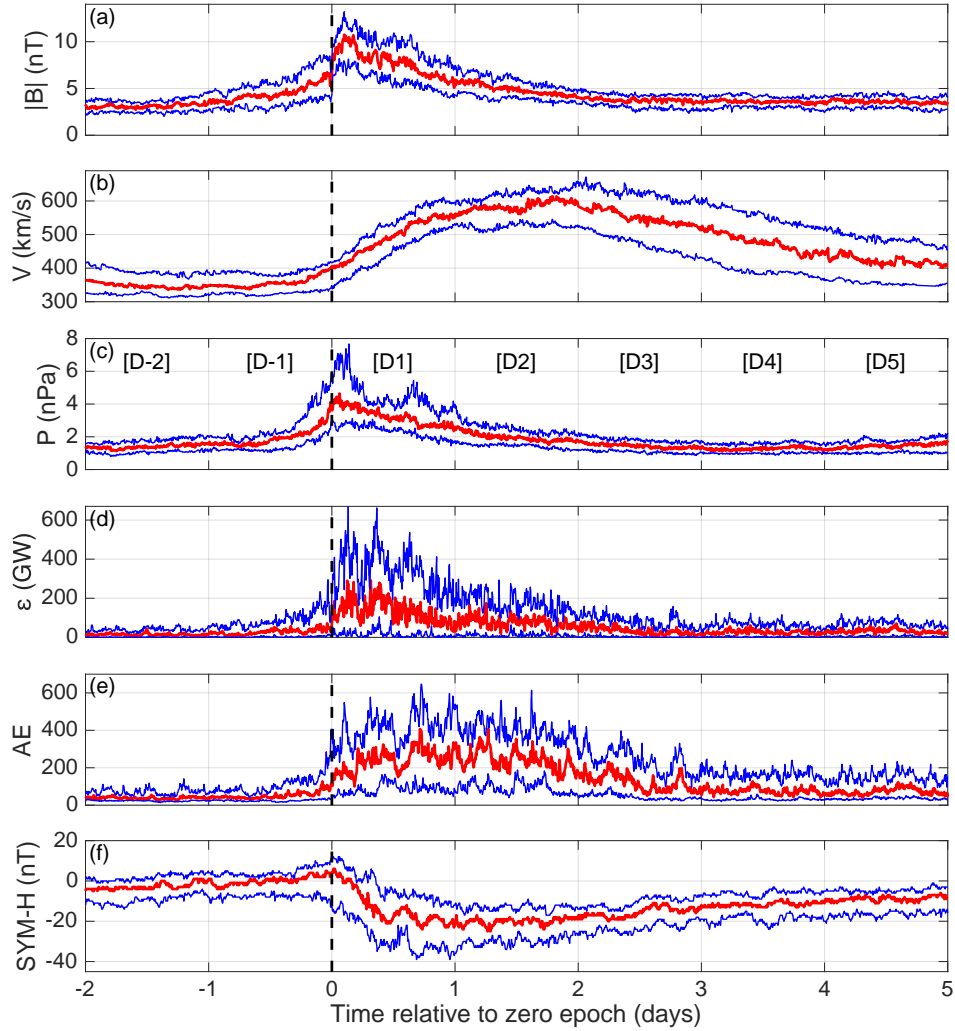


**Figure 4.1.** Superposed epoch analysis of solar wind parameters and geomagnetic indices during high-speed stream events. (a) IMF magnitude; (b) solar wind speed; (c) solar wind dynamic pressure; (d) Akasofu epsilon parameter; (e) AE index; (f) SYM-H index. Red lines represent median values, and blue lines give upper and lower quartiles. Day numbers are given in panel (c). (adapted from Paper I)

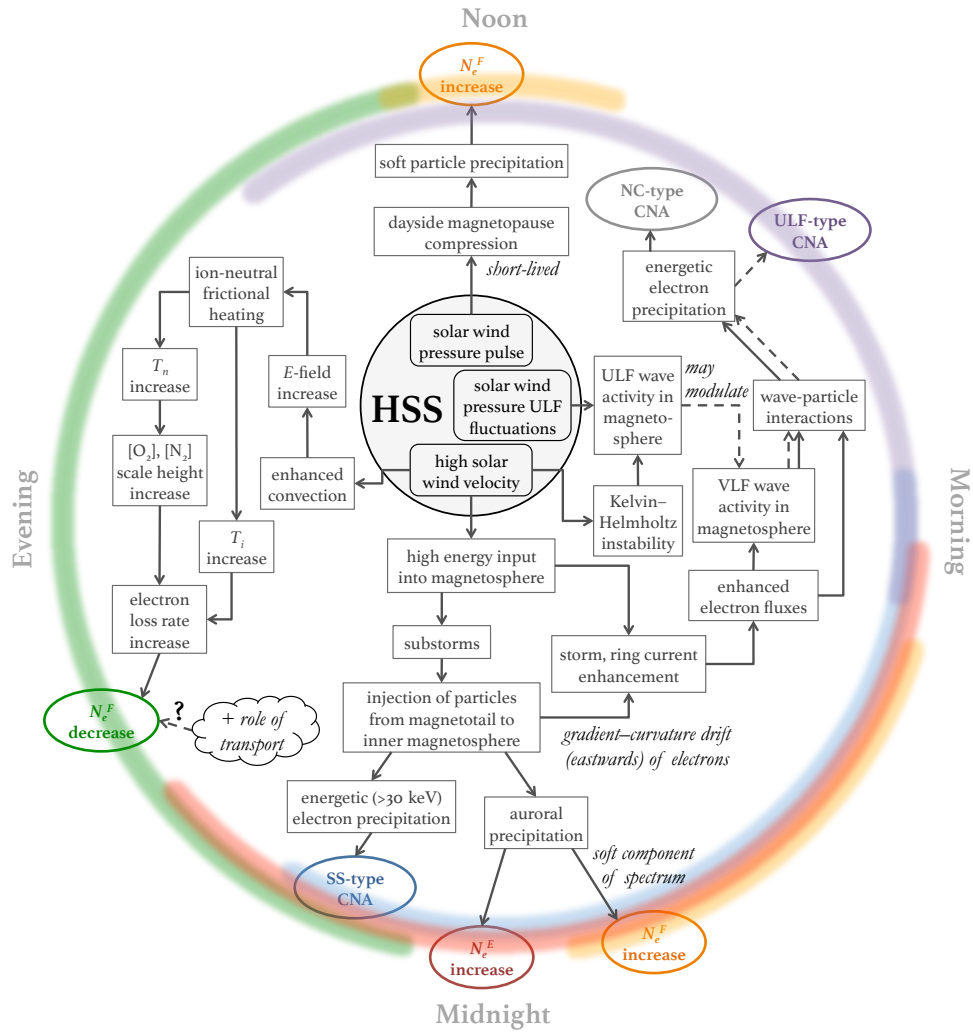


**Figure 4.2.** Summary of studied solar wind high-speed stream effects on the auroral ionosphere. Observations of the responses of the  $D$ ,  $E$  and  $F$  regions are shown by MLT sector, and interpretations are given as a box diagram.

### 4.1.3 $E$ and $F$ region responses

Sodankylä ionosonde data indicate different effects on the  $F$  region for different MLTs and seasons. Figure 4.3 presents the results of the phase-locked superposed epoch analysis of  $f_oF_2$  and  $f_oE(s)$  during the 95 high-speed stream events, with a phase-locking time at 5 UT (7.5 MLT). The events were divided into three seasons of equal length: summer (within  $\pm 2$  months from the summer solstices), winter (within  $\pm 2$  months from the winter solstices), and equinox (within  $\pm 1$  month from the spring and autumn equinoxes). This separation according to seasons is important given that the background ionisation differs significantly between summer, equinox and winter times, owing to the high geographic latitude location of Sodankylä.

In each panel of Figure 4.3, the data correspond to variations of median values of  $f_oF_2$  (top panels) and  $f_oE(s)$  (bottom panels) during high-speed stream events compared to pre-event median values, taken on day D-2. Effects are shown as a function of MLT (azimuthal coordinate) and day number (radial coordinate) from day D-1 (inside the black circle) to day D4 (outermost sectors). The main conclusions drawn from this figure can be summarised under three points.

- (i)  $f_oF_2$  exhibits a weak, short-lived enhancement near noon during day D1, visible in each season.
- (ii)  $f_oF_2$  is also increased during midnight-to-morning MLT hours in equinox, and in the morning sector in winter<sup>1</sup>. These increases last for several days and take place roughly in the same MLT sector as enhancements in  $f_oE(s)$ . In summer,  $f_oE(s)$  is also enhanced in a more restricted MLT sector near midnight, but no matching increase is visible in  $f_oF_2$ .
- (iii)  $f_oF_2$  is decreased compared to pre-event values in the afternoon sector in winter, in the whole pre-noon-to-midnight sector during equinox, and at most MLTs in summer. This effect is visible from day D2 onwards, and persists at least until day D4 in equinox and winter. The strongest depletions occur during equinoxes.

The interpretations of these observations suggested in Paper I are as follows. Firstly, the critical frequency (and hence electron density) increases are attributed to particle precipitation from the magnetosphere. Near noon, around the zero epoch of a high-speed stream event, the solar wind dynamic pressure pulse may provoke the scattering of low-energy particles into the loss cone through the compression of the magnetopause, producing  $F$ -region ionisation. This corresponds to the processes shown in the top of Figure 4.2. On the nightside, the  $f_oE(s)$  enhancements are likely to be related to auroral particle precipitation by substorm activity taking place during high-speed stream events (see AE index panel of Figure 4.1). If the precipitation energy spectrum has a soft component, part of the energy is deposited in the  $F$  region, which may enhance its electron density noticeably if the background ionisation is low (winter and equinox). In summer, however, the nighttime ionosphere being sunlit above Sodankylä, this effect may be negligible to create a measurable  $f_oF_2$  increase.

---

<sup>1</sup>Data availability was insufficient to make statistics during nighttime MLT hours in winter, since the  $F$  region is very often blanketed by underlying auroral  $E$  layers. Therefore, no echo corresponding to the  $F$ -region peak is present in the ionograms, and  $f_oF_2$  cannot be scaled.

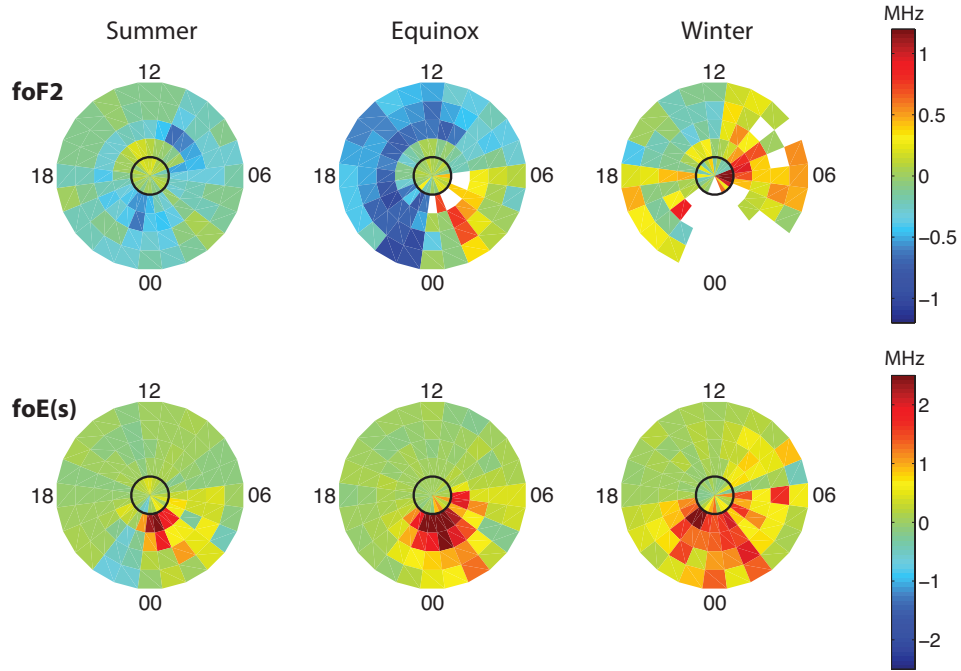


**Figure 4.3.** Change in the median of (top row)  $f_oF_2$  and (bottom row)  $f_oE(s)$  from background level (day D-2) during a high-speed stream event, with phase-locking time at 5 UT (7.5 MLT). Columns show seasons. In each panel, the azimuthal coordinate is MLT, and the radial coordinate is day number, from day D-1 (innermost sectors) to day D4 (outermost sectors). The black circle shows the zero epoch. (reproduced from Paper I)

This chain of phenomena leading to these observations appears in the bottom part of Figure 4.2.

Secondly, the noon-to-midnight  $f_oF_2$  decrease examined in Paper I is suggested to be associated with increased electric fields that produce ion-neutral frictional heating. Frictional heating increases the loss rate of  $O^+$  in the ionosphere by two processes. The first one is neutral heating producing thermal expansion of the ionosphere, which enhances the molecular ( $N_2$  and  $O_2$ ) content at the  $F$ -region peak. The second one is ion heating which may occur under strong enough electric fields (about 50–60 mV/m), leading to an enhancement of the chemical reaction coefficients. Both processes contribute to reduce the  $O^+$  density by producing  $O_2^+$  and  $NO^+$  ions which recombine promptly, leading to a reduction of the  $F$ -peak electron density. These processes appear in the left-hand side of Figure 4.2. Besides, the  $F$ -peak electron density decreases are collocated with signatures of enhancements in the eastward electrojet, visible in the Sodankylä magnetometer data (not shown here; see Figure 8 of Paper I),

which is consistent with the above-described interpretation. However, Paper I does not address possible effects of transport, which is likely to play a significant role in the dynamics of the  $F$  region. This should be the subject of future studies. Besides, Paper I does not discuss in detail why the  $f_oF_2$  decrease is significantly greater around the equinoxes compared to summer and winter times. This would require further investigation, but some possible explanations may be suggested. First, it is known that geomagnetic activity is more intense around the equinoxes than during the solstices [Sabine, 1852; Cortie, 1912], so high-speed streams may have greater effects on the equinox ionosphere. This enhanced activity may be due to the annual variation of the Earth magnetic dipole axis direction [Russell and McPherron, 1973] or to the interhemispheric asymmetry of solar illumination [Lyatsky et al., 2001]. Then, the greater  $F$ -region depletion during the equinoxes might be related to the semiannual variation of  $f_oF_2$  with greater  $F$ -region peak density around the equinoxes than in summer and winter [Torr and Torr, 1973; Rishbeth and Müller-Wodarg, 1999; Rishbeth et al., 2000b], visible from the top panels of Figures 9 and 10 in Paper I. It may be speculated that a change in the equilibrium between production, loss and transport processes could lead to a greater depletion during equinox-time high-speed stream events. These seasonal differences should be investigated in future studies (see Conclusion).

#### 4.1.4 Energetic particle precipitation

Paper II studies cosmic noise absorption during high-speed stream events. Cosmic noise absorption is generally produced by energetic ( $> 30$  keV) particle precipitation which ionises the  $D$  region of the ionosphere. Two main aspects are studied in Paper II.

First, high-speed stream events are divided into two categories, called “long” and “short”. During short events, the solar wind speed reaches its maximum value within 24 hours after the zero epoch. These cause cosmic noise absorption at auroral latitudes during up to three days after the zero epoch, but seldom affect subauroral latitudes. Long events, on the other hand, are those during which the solar wind speed reaches its maximum value later than 24 hours after the zero epoch. They are responsible for much more frequent cosmic noise absorption (in up to 65% of the cases on day D2), which persists at least until day D4 and which may be observed down to subauroral latitudes (in Oulu, at  $L = 4.5$ ).

Secondly, Paper II focuses on the conditions during which cosmic noise absorption occurs. Cosmic noise absorption (CNA) events (i.e., at a given riometer station, 15-min time intervals during which the cosmic noise absorption reaches a value above 0.5 dB) are sorted into three categories:

- (i) substorm-type (SS-type), if  $X < -100$  nT was observed at the neighbouring magnetometer station at the time of the CNA event;
- (ii) ULF-type, if the CNA event is not already labelled as substorm-type, and if the amplitude of fluctuations of the geomagnetic field horizontal component in the Pc5 frequency range was above 3 nT during the CNA event;
- (iii) non-classified (NC-type CNA) otherwise.

This classification is such that no CNA events are counted twice. The MLT distributions of these three types of CNA events at each of the four riometer stations used in the study are shown in Figure 4.4. These distributions are given for each day number from day D-2 until day D4. It appears quite clearly that substorm-type CNA essentially occurs within nighttime MLT sectors, and is restricted to auroral latitudes, with only few such events observed in Oulu. ULF-type CNA, on the other hand, is mostly observed on the dayside, with distributions reaching a broad maximum in the pre-noon to early-afternoon sector at auroral latitudes. In Oulu, ULF-type CNA is less frequent than at auroral latitudes, but dominates on day D1, and is maximum in the early-afternoon sector. Very few ULF-type CNA events are observed down to Jyväskylä ( $L = 3.8$ ), and only on day D1. Non-classified CNA events show quite flat distributions at auroral latitudes, exhibiting a small evening minimum, and they are only moderately increased during high-speed streams. In Oulu, NC-type CNA events are enhanced in the afternoon sector during days D1, D2 and D3, with a main peak around 15–16 MLT. In Jyväskylä, the NC-type CNA event distribution shows a small peak between 12 and 18 MLT, but there is no clear variation in this distribution from one day to another.

Paper II proposes the following interpretation for these CNA event distributions. Substorm-type CNA events show correlation with the AE index at zero lag, hence substorm-type CNA events are produced by electrons that have gained their energy as a consequence of processes directly associated with substorms, e.g. magnetic reconnection in the tail [Lui, 1991; Torbert *et al.*, 2016]. These processes leading to the production of substorm-type CNA appear in the bottom part of Figure 4.2.

Even though ULF-type CNA events are not associated with a locally occurring substorm, they may be associated with substorm plasma injections and subsequent electron drift from the night sector [Meredith *et al.*, 2001; Miyoshi *et al.*, 2013]. Indeed, a cross-correlation of the AE index and CNA measured at Ivalo and Sodankylä revealed that ULF-type CNA events are correlated with substorm activity with a delay of the order of 30 min (see Figure 9 of Paper II). This delay corresponds to the time needed for  $E \approx 70$  keV electrons with a small pitch angle ( $\alpha = \pi/12$ ) to drift from the midnight MLT sector to noon, and it is consistent with results from Beharrell *et al.* [2015] based on observations and modelling. In order for trapped electrons to precipitate into the ionosphere, their pitch angle needs to be decreased. An efficient mechanism is the cyclotron resonance of electrons with whistler-mode VLF waves [Thorne *et al.*, 2010, and references therein], in particular whistler-mode chorus waves which may scatter electrons into the loss cone over a broad range of energies [e.g., Lam *et al.*, 2010]. However, the growth rate of the electron-cyclotron VLF instability can be modulated by compressional ULF waves [Coroniti and Kennel, 1970; Motoba *et al.*, 2013]. Hence, we suggest that the main role of ULF waves is to modify the whistler-mode wave growth rates that produce the scattering of electrons into the loss cone.

Finally, the non-classified CNA events are probably associated with whistler-mode waves taking place in the magnetosphere independently from the presence of ULF waves. These VLF waves may be chorus waves in the midnight to morning and to

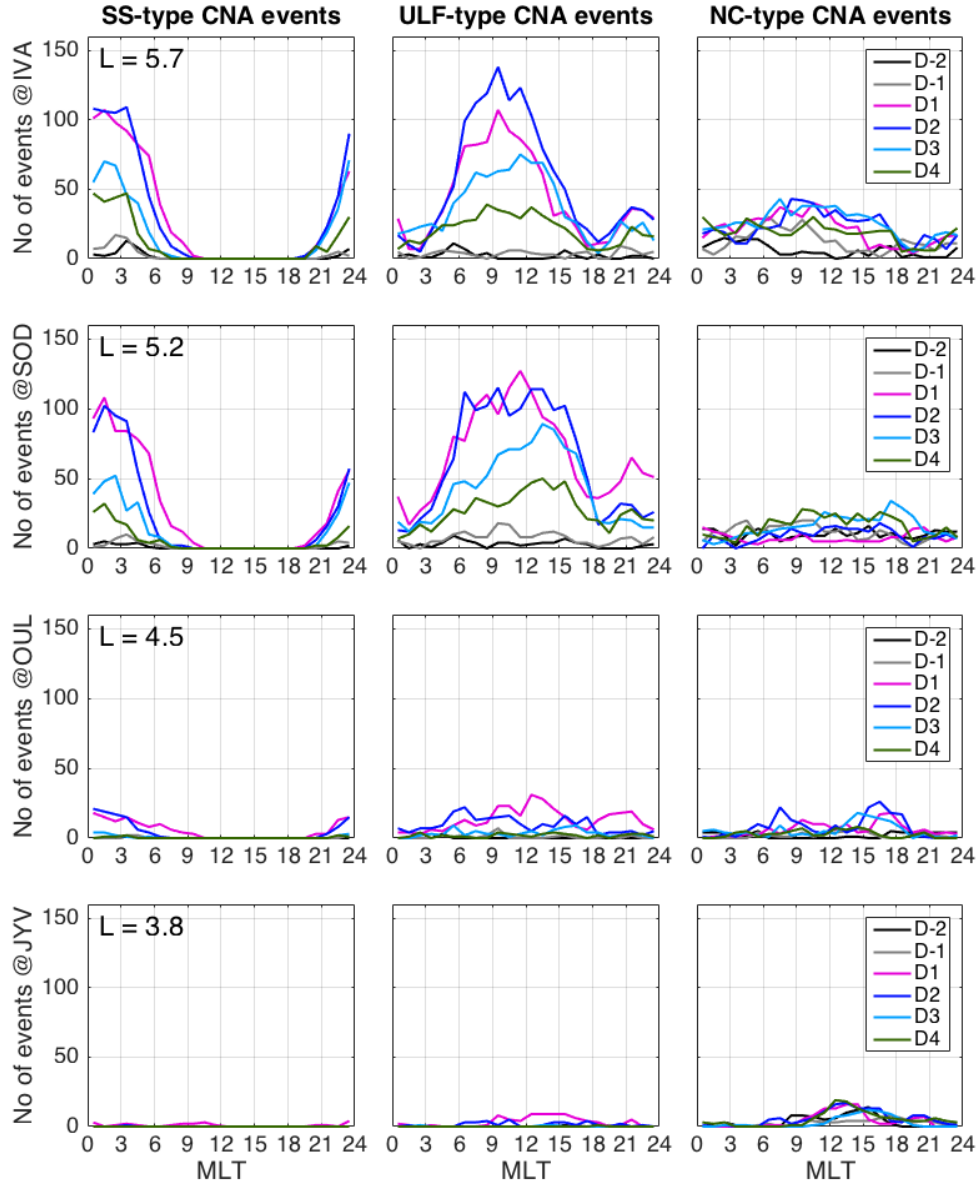


**Figure 4.4.** MLT distribution of CNA events classified into substorm-type (left panels), ULF-type (middle panels) and non-classified-type (right panels). The riometer stations are Ivalo (first row), Sodankylä (second row), Oulu (third row) and Jyväskylä (fourth row). Each line color corresponds to a day relative to zero epoch as indicated in the legend. (reproduced from Paper II)

day sectors, hiss in the afternoon sector, magnetosonic noise on the day to evening sector, and EMIC waves in the evening sector [Thorne *et al.*, 2010].

## 4.2 Modulation of energetic precipitation during pulsating aurora

Paper III presents an event study of pulsating aurora above Kilpisjärvi ( $L = 6.2$ ) on 26 February 2014. The aim was to assess whether pulsations can be seen in cosmic noise absorption data, and if they match the optical emission pulsations. This study makes use of the colocation of the Kilpisjärvi all-sky camera and KAIRA, used here in a riometry mode, since these two instruments are only a few kilometres apart from each other.

The chosen frequency at which CNA is studied here is 30 MHz. At this frequency, the KAIRA beams have a full width at half maximum ( $-3$  dB) of  $19^\circ$  [McKay-Bukowski *et al.*, 2015]. The beams are mapped onto the all-sky camera images in order to enable a comparison of data sets within chosen beams. The optical data are reduced to a time series corresponding to each KAIRA beam by computing a weighted average of the pixel values within the beam area.

In Paper III, data from both instruments are compared within three KAIRA beams close to the magnetic zenith. First, a very good correlation (Pearson correlation coefficient about 0.9) is found between the time series during the whole pulsating aurora event (02:00–02:35 UT). This indicates that the precipitating electron flux variations are consistent in the auroral (1–10 keV) and energetic ( $> 30$  keV) ranges.

Then, subsets of the time series are chosen to study more carefully time intervals during which a given beam is filled with a pulsating structure. The duration of these subsets is of the order of 2–3 min, as the pulsating patches drift in and out of the beams. Figure 4.5 shows the time series of blue-line emission (blue) and cosmic noise absorption (orange) during those time intervals. The raw data are shown in the top panels. To isolate the pulsations, a high-pass filter with a cutoff frequency of 16.7 mHz (1-min period) was applied, thus removing the data baselines. The filtered data, showing only the modulation of the auroral emission and cosmic noise absorption, are presented in the bottom panels. For each of the three KAIRA beams, it can be easily seen that (i) pulsating signatures are visible in cosmic noise absorption, and (ii) they match very well the optical pulsations. While it has been known since the late 1970s that cosmic noise absorption may be observed during pulsating aurora [Berkey, 1978; Arnoldy *et al.*, 1982], this is the first time a modulation of CNA close-to-identical to the optical emission one has been reported. This suggests that the modulation of the electron precipitation affects a broad range of energies.

The statistical characteristics of the observed pulsations in these subsets are obtained by applying the superposed epoch analysis. The zero epochs are chosen to correspond to the local brightness minima in the optical data. Results indicate that the pulsation periods are irregular (i) from one beam to another (12 s for beam 1, 10 s for beam 2, 8–10 s for beam 3), i.e., from one pulsating structure to another, but

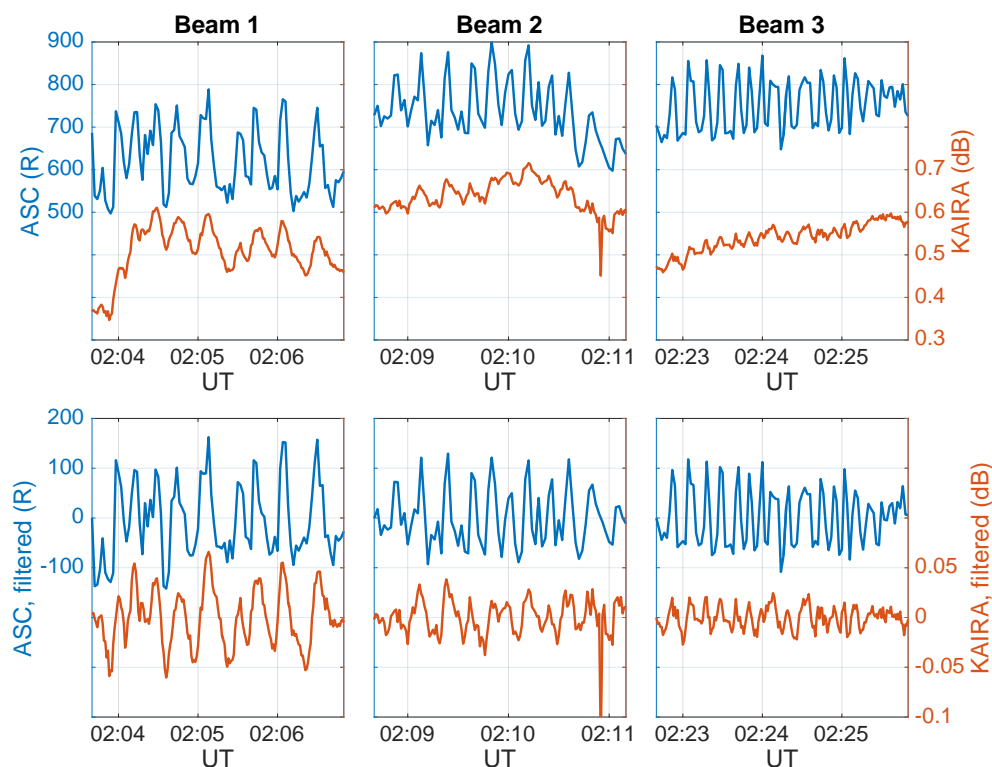


**Figure 4.5.** Time series of the data during pulsating time intervals in beams number 1, 2 and 3. (first row) Original optical (blue) and CNA (orange) data. (second row) High-pass-filtered optical (blue) and CNA (orange) data. (adapted from Paper III)

also (ii) as a function of time for a given beam, as a time spreading can be seen in the superposed epoch curves (see Figure 4 of Paper III). These observations can be made consistently with both the optical and cosmic noise absorption data. The irregularity in the (optical) pulsation periods was previously reported by *Humberset et al.* [2016].

In order to assess whether the CNA modulations could originate from electron density variations in the lower  $E$  region where optical emissions come from ( $\sim 100$  km altitude), simulations are carried out using the Sodankylä Ion–Neutral Chemistry (SIC) model [Verronen *et al.*, 2005]. SIC is a one-dimensional coupled chemistry model of the middle atmosphere which includes the resolution of the continuity equation for ion and neutral species in the  $D$  region, taking into account production processes including solar extreme ultraviolet and X-ray radiation, particle precipitation, and galactic cosmic rays, and loss processes through several hundred reactions. The precipitating spectrum is inferred by inverting electron density profiles measured by the European Incoherent Scatter Radar (EISCAT) system within the Kilpisjärvi all-

sky camera field of view during the pulsating aurora event, using a method described in *Turunen et al.* [2016]. Then, two scenarios are tested. In the first scenario, the precipitating spectrum is modulated (5 s on, 5 s off sequences, 25% modulation, based on beam 1 observations) only for energies up to 10 keV, i.e., auroral energies, reaching down to about 100 km altitude in the ionosphere. In the second scenario, the modulation is applied to all energies in the precipitating spectrum, i.e., including energies which affect the *D* region. Results show that the CNA modulation resulting from the first scenario is one order of magnitude too low in amplitude compared to what is observed in beam 1, while the second scenario leads to CNA pulsations with an amplitude close to the observations. This suggests that the CNA modulation can be explained if the energetic component of the electron precipitation is pulsating alongside the auroral component.

The results presented in Paper III may help in understanding the mechanism behind the origin of pulsating aurora. These results give support to a model proposed by *Miyoshi et al.* [2010, 2015b] in which chorus waves propagating along the field line can cause broad-energy electron loss-cone scattering simultaneously, hence predicting that electron precipitation is modulated over a wide energy range during pulsating aurora. In addition, the findings presented in Paper III suggest that the development of riometers sensitive enough to detect pulsating aurora signatures in cosmic noise absorption may enable the study of pulsating aurora even when optical observations are not available, e.g., because of overcast weather or during the polar summer.

### 4.3 Analysis of Mars Express data with the radio-occultation model

Papers IV and V present the new analysis approach for Mars Express radio-occultation data developed during this thesis work. The model-based method described in section 3.2.2 is tested on two radio-occultation experiments, one probing the dayside Martian environment and one performed near the twilight terminator of the planet. This section summarises the main results presented in Papers IV and V.

#### 4.3.1 Reproduction of the frequency residual profile

A first step to assess the validity of the new approach for Mars Express radio-occultation data analysis is to compare the simulated frequency residual profile to the data measured by MaRS. Then, the temperature and density profiles obtained with the fitted parameters may be compared to the results of the classical inversion.

In Paper IV, the model is first tested on a radio-occultation experiment probing the dayside of Mars. Indeed, this ensures that the spherical symmetry assumption needed for the classical inversion is not too strongly violated, thus enabling comparison with its results. For this purpose, data from the experiment of 28 April 2007 were used. The frequency residual profile obtained with the modelling approach is shown in Figure 4.6 (grey line). It is compared to the profile measured by MaRS (thick black line) during this experiment. One may see that after optimisation of its free parameters, the model reproduces well the overall shape of the measured frequency

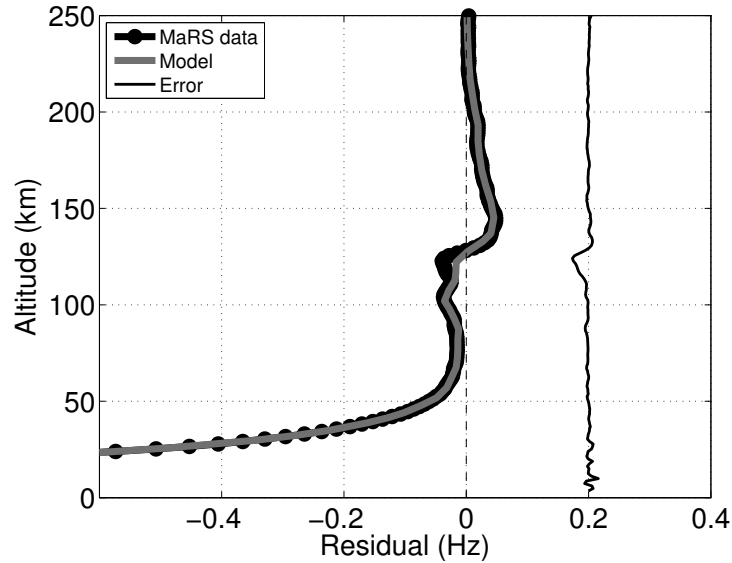


**Figure 4.6.** Frequency residual profiles for the experiment of 28 April 2007. The thick black line shows the MaRS measurements, and the grey line shows the frequency residual simulated by the model. The thin line gives the difference between those curves, shifted by 0.2 Hz for visibility. (reproduced from Paper IV)

residual profile. The difference between simulation and measurement is indicated with a thin line, shifted by 0.2 Hz for visibility. At most altitudes, the agreement is very good; only between 110 and 130 km is there a noticeable difference, the simulation reproducing a lower deviation than measured. This altitude range corresponds to the lower ionosphere, and a possible reason for this difference may be in relation to the X-ray and UV component of the solar flux model used as an input.

The comparison of the retrieved temperature and density profiles with the results given by the classical inversion (not shown here; see Figures 6–8 in Paper IV) reveals some differences. In the ionosphere, while the main electron density peak  $M_2$  is well reproduced, the  $M_1$  layer is overestimated by the model. This corresponds to the altitude range where the frequency residual is not well reproduced either, suggesting that both issues may have the same origin. At lower altitudes, in the neutral atmosphere, the comparison of neutral density profiles obtained with both methods shows good agreement. However, significant differences can be seen in the temperature profiles, not only near the altitudes where a boundary condition is needed for the classical inversion, but also down to the ground. A possible explanation for this discrepancy will be given in 4.3.4.

### 4.3.2 Influence of medium asymmetry

One of the main motivations for developing the ray-tracing approach was to overcome the limitations related to the planetary environment spherical symmetry assumption needed to apply the classical inversion. While this assumption may not be so critical in the neutral atmosphere, it may be strongly violated in the ionosphere, since the electron density is strongly dependent on the local solar zenith angle. Figure 4.7 gives the possible solar zenith angles at the occultation point as a function of the geometry of the radio-occultation experiment. A sketch on the left-hand side presents the geometry. For a given radio-occultation experiment, the occultation point is the location on the surface of Mars where the radio wave is stopped at the instant when the signal connection between the spacecraft and the ground station on Earth is lost. The ensemble of possible occultation points on the Martian surface for a given angle  $\theta$  defined by the Earth, the Sun and Mars draws an approximate circle around Mars, corresponding to the edge of Mars when seen from the Earth. It appears as a yellow segment in Figure 4.7 because of the projection. The extreme solar zenith angle values are given by the points of this circle located in the ecliptic plane. On the dayside of Mars,  $\alpha_1$  is the smallest possible solar zenith angle, and its supplementary  $\alpha_2$  is the largest possible solar zenith angle, on the nightside. The actual solar zenith angle at the occultation point during a radio-occultation experiment depends on the location of Mars Express, and is comprised between  $\alpha_1$  and  $\alpha_2$ . The right-hand part of the figure gives the possible solar zenith angles at the occultation point as a function of  $\theta$ . Since the orbit of Mars exhibits some ellipticity (or eccentricity), the allowed angles are given in the case when Mars is closest to the Sun (perihelion, in blue) and when it is furthest from the Sun (aphelion, in red). For instance, for  $\theta = 45^\circ$  in an aphelion configuration for Mars, the possible values for the solar zenith angle at the occultation point are comprised between  $53^\circ$  and  $127^\circ$ . Interestingly, one may see that the most frequent solar zenith angles near the occultation point are around  $90^\circ$ , which corresponds to the twilight terminator.

To illustrate the asymmetry of the ionosphere in the vicinity of the twilight terminator, Figure 4.8 shows the electron density derived by the model presented in Paper IV within the radio-occultation plane for the experiment of 14 May 2007. The radio-occultation plane is defined by the positions of the spacecraft at the occultation time, the centre of Mars, and the ground-based station on Earth. For this experiment, the solar zenith angle at the occultation point was  $89^\circ$  (see Table 2 in Paper IV). In the figure, the twilight terminator features are clearly visible in the electron density, with negligible ionisation on the nightside (right-hand side). A dash-dotted line shows the approximate trajectory of the lowest ray before occultation, which represents the lower boundary of the ionosphere through which radio waves propagate during this radio-occultation experiment. It is clear that the ionosphere does not exhibit spherical symmetry during an experiment with such a geometry, not even when considering only the vicinity of the occultation point. Hence, in this case, the classical inversion method is not suitable to analyse the data and retrieve the atmospheric and ionospheric profiles. This underlines the importance of developing alternative approaches to analyse radio-occultation data in order to be able to make use of all available experiments to improve the understanding of the Martian environment.

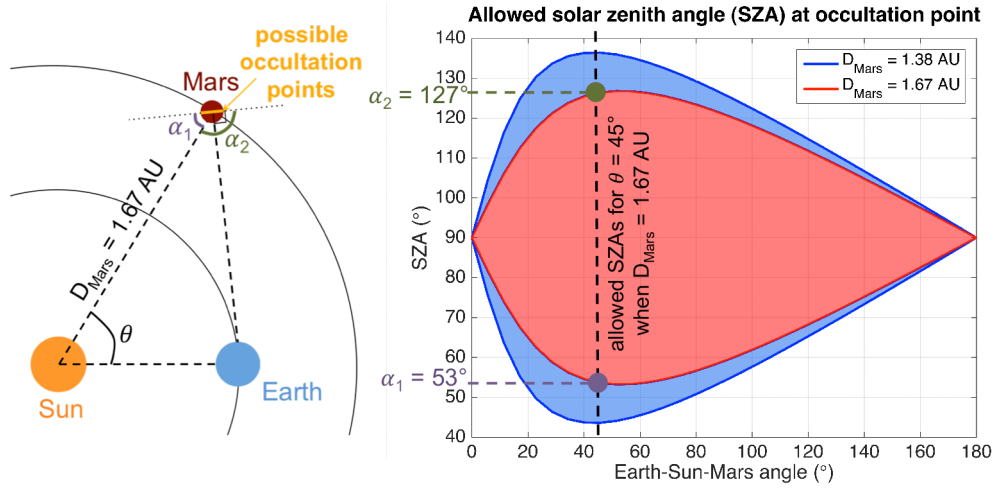


**Figure 4.7.** (left) Sketch of the Sun–Earth–Mars configuration indicating the possible locations of the occultation point during a radio-occultation experiment, seen in the ecliptic plane. (right) Allowed solar zenith angles at the occultation point as a function of the angle between the Sun–Earth and Sun–Mars directions. Due to the ellipticity of the Martian orbit, the angles are shown when Mars is at its perihelion (blue) and aphelion (red).

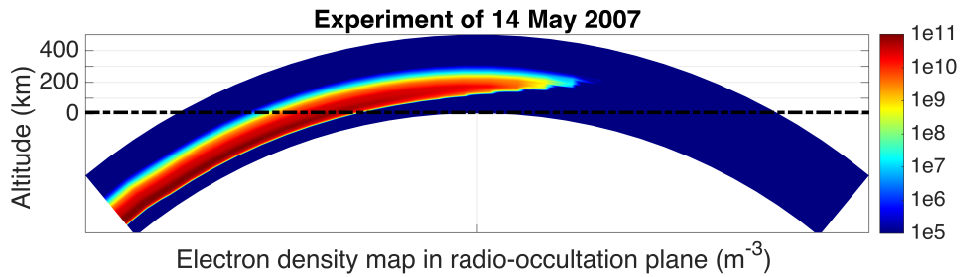


**Figure 4.8.** Electron density map in the radio-occultation plane for the experiment of 14 May 2007. The dash-dotted black line shows the trajectory of the lowest ray before occultation, thus defining the boundary of the domain where radio waves propagate during the occultation experiment. (adapted from Paper IV)

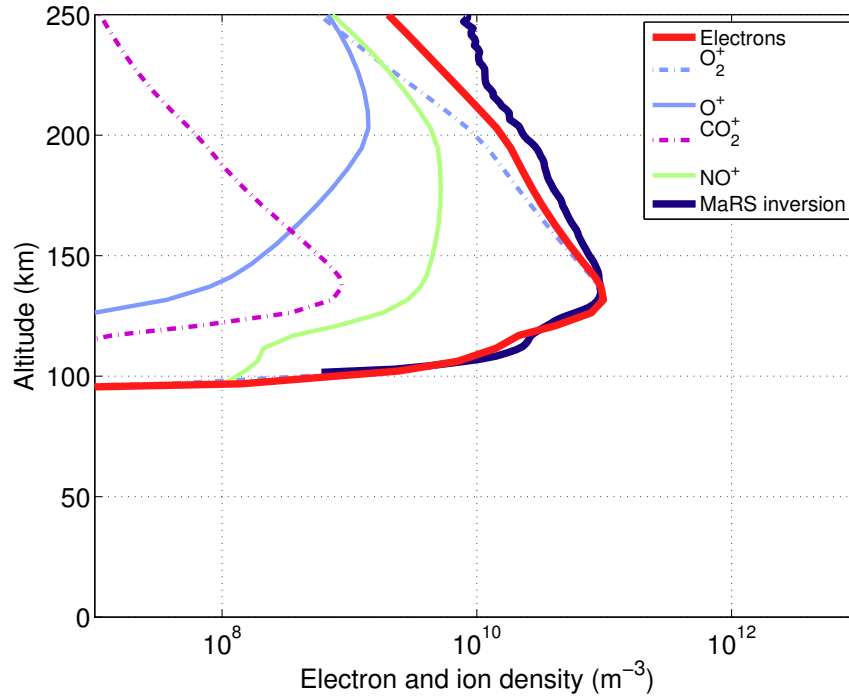


**Figure 4.9.** Ionospheric density profiles, showing simulated electron (red),  $O_2^+$  (dash-dotted blue),  $O^+$  (solid blue),  $CO_2^+$  (purple) and  $NO^+$  (green) number densities, and electron density (dark blue) obtained with the radio science classical inversion. (reproduced from Paper V)

### 4.3.3 Ion density profiles

Another interest of the model-based approach for radio-occultation data analysis is that this method enables the estimation of the main ion species densities in the Martian ionosphere. This is possible since the electron density is calculated by modelling the photoionisation and chemistry of the main ion species in the Martian ionosphere (see section 3.2.2). Hence, once the measured frequency residual profile has been fitted with the model by adjusting its free parameters, it is possible to compute the density profiles of the five modelled ion species:  $O_2^+$ ,  $O^+$ ,  $CO_2^+$ ,  $NO^+$ , and  $N_2^+$ .

Figure 4.9 shows the ionospheric density profiles retrieved for the experiment of 28 April 2007. The electron density profile obtained by the model-based approach (red line) is the sum of the densities of  $O_2^+$  (dash-dotted blue),  $O^+$  (solid blue),  $CO_2^+$  (purple),  $NO^+$  (green) and  $N_2^+$  (not visible: too low density) ions given by the ionospheric model. One may see that the dominant ion species up to almost 250 km altitude is  $O_2^+$ . The modelled electron density (red line) is compared to the electron density profile coming from the classical inversion (dark blue line). The

overall agreement between these two profiles is fairly good, especially near the main peak ( $M_2$ ). However, discrepancies are visible above the peak, where the modelled electron densities are lower than those obtained by the classical inversion method. This may be due to the fact that the present version of the ionospheric model used in the radio-occultation data analysis method does not include effects of vertical transport of species. Another discrepancy can be seen near the secondary electron density peak ( $M_1$ ), where the model also gives lower electron densities compared to the classical inversion. Understanding the origin of this difference still requires future work; this may be related to the fact that the X-ray and EUV component of the solar irradiance spectrum is subject to significant variability.

#### 4.3.4 Improvements introduced in Paper V

A few months after publication, Paper IV received a comment by *Pätzold et al.* [2016] raising some criticism on the presented approach for radio-occultation data analysis. While part of the comment aimed at advocating the historical importance of the classical inversion method, several precise points on the new approach were questioned. The reply given in Paper V aimed not only at providing clarifications on the aspects which might have been misunderstood by the authors of the comment, but also at taking into account the relevant sources of criticism, in order to improve the new method.

Besides minor remarks suggesting possible improvement in the implementation (solar flux model, effect of transport in the ionosphere, validity of choosing a homogeneous atmospheric refractive volume value...), one major issue was indeed pointed out in the comment, which needed to be addressed. The results obtained with the model version presented in Paper IV did not take into account the frequency change between the uplink and the downlink waves (transponder ratio mentioned in section 3.2.1). As a consequence, the uplink and downlink ray trajectories were identical, whereas in reality the refraction undergone by the uplink and downlink waves in the Martian ionosphere are different. This had to be corrected, and the frequency residual computation module of the model was modified accordingly. This correction made it possible to partly solve some issues which were discussed in Paper IV, in particular the unexplained difference between the atmospheric temperature profiles obtained by the new method and the classical inversion.

Another noticeable improvement which is presented in Paper V is the computation of error bars on some parameters. As explained in the paper, the new approach being based on a direct simulation of the radio wave trajectories during the radio-occultation experiment, error bars can intrinsically only be given for the parameters adjusted through the optimisation procedure, in particular: neutral temperatures at reference altitudes in the lower atmosphere, exospheric temperature, and neutral densities at a reference altitude. Indeed, the altitude profiles (neutral temperature, neutral, ion and electron densities) are fully determined by these parameters. Propagating the uncertainties of the fitted parameters to obtain error bars in the altitude profiles would therefore not make much sense, and would in any case require a full dedicated study. At this stage of the method development, this is certainly not a priority,

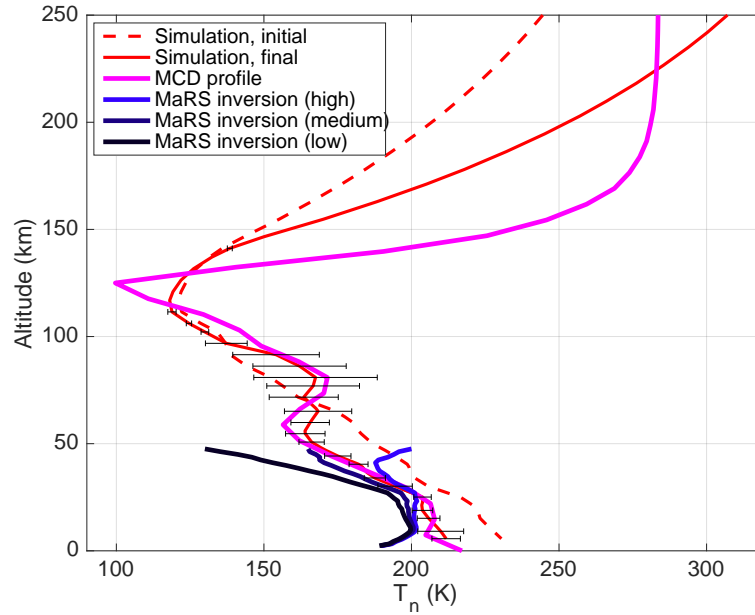


**Figure 4.10.** Comparison of the initial (dashed red line) and final (solid red line, with error bars) atmospheric temperature profiles for the experiment of 28 April 2007. The magenta line shows the neutral temperature profile given by the Mars Climate Database (MCD) v5.2 for the conditions of the experiment. The blue lines show the neutral temperature profile retrieved with the standard inversion method using high (light blue), medium (medium blue), and low (dark blue) upper boundary conditions. (modified from Paper V)

given that the model would still require improvement (e.g., implementation of the effect of transport in the topside ionosphere) before being usable for routine analysis of MaRS radio-occultation data. Figure 4.10 shows the neutral temperature profile retrieved with the corrected new method, where error bars were added at the altitudes corresponding to fitted temperature points. It can be seen that uncertainties are larger between 50 and 100 km altitude, which is probably related to the lower signal-to-noise ratio in the frequency residual data (see Figure 4.6). The temperature profile from the Mars Climate Database (MCD) v5.2 [Millour *et al.*, 2015] and the profiles retrieved with the classical inversion are also given for comparison. One may notice that the neutral temperature profile obtained with the model-based analysis (solid red line) shows good agreement with the MCD profile (magenta line) below 120 km. However, above 120 km, the two profiles are quite different. This may come from the fact that the method for radio-occultation data analysis presented in this thesis constrains the neutral temperature profile by coupling it to the ionospheric ion and electron densities through the computation of the photochemical equilibrium, while the MCD profile has no couplings with ionospheric parameters.

## Chapter 5

# Conclusion

The work presented in this thesis studies two planetary ionospheres by making use of versatile instruments and by developing new data analysis methods and novel modelling. The behaviour of the Earth's ionospheric  $F$  and  $E$  regions under solar wind high-speed stream driving was studied using ground-based instruments in Paper I by developing the phase-locked superposed epoch analysis method. In Paper II, the effect of high-speed streams on the  $D$ -region ionosphere was studied using the standard superposed epoch analysis method. Paper III showed for the first time the manifestation of pulsating aurora in riometer data. For Mars, a novel approach was developed in Papers IV and V for the analysis of Mars Express radio-occultation data to retrieve atmospheric and ionospheric profiles without needing to make strong assumptions on the planetary environment.

In Paper I, the phase-locked superposed epoch analysis method was developed to study 95 solar wind high-speed stream events using data from the Sodankylä ionosonde ( $L = 5.25$ ). Observations indicated a short-lived dayside increase in the  $F$ -peak electron density near the time of arrival of the corotating interaction region, which may be triggered by the solar wind pressure pulse associated with the stream interaction region, resulting in particle precipitation in the  $F$  region of the ionosphere from the dayside plasma sheet. In addition, post-midnight to morning increases in the electron peak density in the  $F$  and  $E$  regions are observed during several days, attributed to auroral electron precipitation during substorms. The most pronounced feature in the  $F$ -region peak electron density during equinoxes and summer is a decrease extending from noon to midnight and lasting for several days. The suggested explanation is that increased electric fields produce ion-neutral frictional heating, causing thermal expansion of the neutral atmosphere and an increase in the ion temperature. Both processes enhance the electron loss rate in the  $F$  region. The effect of transport was not investigated in that study.

The same set of high-speed stream events was used in Paper II to study cosmic noise absorption in the auroral and subauroral ionosphere. Riometer observations between  $L = 3.5$  and  $L = 5.7$  revealed that auroral latitudes are the most affected by energetic electron precipitation during high-speed stream events, with moderate

effects noticeable down to  $L = 4.5$ . Events for which the maximum solar wind speed is reached later than 24 hours after the zero epoch were called “long” events, and those produce cosmic noise absorption more frequently than “short” high-speed stream events, for which the maximum solar wind speed is reached less than 24 hours after the zero epoch. Three categories of cosmic noise absorption events were defined, depending on whether the absorption events coincide with substorm electrojet signatures, Pc5-range geomagnetic ULF pulsations, or neither of these. The substorm-type CNA events have the largest absorption values and they are directly associated with substorm injections on the nightside. The ULF-type CNA events are typically also associated with substorms, but with a delay of  $\sim 30$  min as the electrons drift eastwards towards the dayside. The electrons are likely to be scattered into the loss cone by ULF-modulated VLF whistler waves.

In Paper III, pulsating aurora signatures were for the first time identified in cosmic noise absorption data, representing observational evidence that the precipitation flux is modulated not only at auroral energies (1–10 keV) but also at higher energies ( $> 30$  keV), and that the modulation takes place simultaneously over this energy range. This result may give support to theories which predict a wide-energy modulation of the precipitation flux during pulsating aurora.

Paper IV presented a novel approach to analyse radio-occultation measurements as performed by the MaRS instrument onboard Mars Express, aiming at overcoming some limitations coming from strong assumptions on the planetary environment such as spherical symmetry which are necessary to apply the classical inversion method. The new approach is based on direct simulations of the radio wave propagation in the Martian atmosphere and ionosphere during a radio-occultation experiment. The neutral temperature, neutral density and electron density profiles are retrieved via the adjustment of the model parameters so that the simulated frequency residual profile reproduces the MaRS measurements. In addition, ion density profiles are estimated by the ionosphere model developed for this method, which gives access to new parameters compared to the classical inversion method.

After criticism made in a Comment on Paper IV, a reply was formulated in Paper V to clarify some aspects of the radio-occultation experiment model which had been misunderstood by the authors of the Comment. This also resulted in the correction of the calculation of the frequency residual by taking into account the change between the uplink and the downlink frequencies used during radio-occultation experiments. Error bars on the adjusted model parameters were also computed. This upgrade of the model improved the overall analysis of Mars Express radio-occultation data.

As a direct continuation of this doctoral training work, two future developments may be foreseen. Firstly, one could model the high-speed stream effects on the ionosphere by using the IRAP Plasmasphere–Ionosphere Model (IPIM) [Marchaudon and Blelly, 2015] for a selected event to investigate the mechanism behind the  $F$ -peak depletion. In particular, the role played by horizontal and field-aligned transport could be revealed by such a study. A high-speed stream event has been identified, and data from ground-based and satellite-borne instruments have been collected to provide inputs for the model. The objective will be to compare the results of IPIM

simulations with EISCAT and ionosonde observations during the high-speed stream event.

Secondly, the radio-occultation data analysis method could be transposed to the terrestrial case to analyse ionospheric tomography data using a similar ray tracing approach. This can be achieved by developing a radio wave propagation module to be plugged into a steady-state version of IPIM, which is currently being developed. Precipitating particle measurements and ionospheric convection can also be assimilated into the model. Besides the terrestrial case, the radio-occultation data analysis method could also be adapted to retrieve atmospheric and ionospheric profiles at Venus, Titan, or the Jupiter moons by developing the relevant models for neutral atmospheres and ionospheres. In the case of Mars, the method could still be improved. A first improvement item could be including the effect of vertical transport in the ionospheric model, which is expected to be significant in the topside ionosphere of Mars, above  $\sim 170$  km altitude [Mendillo *et al.*, 2011]. Although this would increase the complexity of the ion density computation by modifying the equations described in section 2.2.2 in Paper IV, one could start by assuming a uniform vertical speed for each given ion species, which would imply introducing an additional loss term in the equations in their present form. Also, the chemical reaction rates could be estimated more accurately by computing the electron temperature. However, this would require an estimation of the heating applied to the electrons, thus adding even more complexity to the model. Another way to improve the method would be to allow the neutral temperature profile to vary as a function of planetary coordinates in order to remove the symmetry in the atmospheric model. The method could then be used to routinely analyse all the available MaRS radio-occultation profiles, which would open the possibility to carry out statistical studies of the Martian ionosphere and atmosphere. Comparison with existing atmospheric and ionospheric models could therefore be considered. The method could also be adapted to analyse radio occultation data from other spacecraft, such as Mars Global Surveyor [Cahoy *et al.*, 2006].

Finally, it is foreseen that this co-supervised doctoral training initiates a tighter collaboration between SGO/UOulu and IRAP and will promote future joint studies of the high-latitude magnetosphere–ionosphere–thermosphere couplings, especially as the coming years should see the emergence of a new-generation incoherent scatter radar system in northern Fennoscandia, EISCAT\_3D.



# Bibliography

- Acuña, M. H., J. E. P. Connerney, N. F. Ness, R. P. Lin, D. Mitchell, C. W. Carlson, J. McFadden, K. A. Anderson, H. Reme, C. Mazelle, D. Vignes, P. Wasilewski, and P. Cloutier (1999), Global distribution of crustal magnetization discovered by the Mars Global Surveyor MAG/ER experiment, *Science*, *284*, 790, doi:10.1126/science.284.5415.790.
- Aikio, A., K. Mursula, S. Buchert, F. Forme, O. Amm, G. Marklund, M. Dunlop, D. Fontaine, A. Vaivads, and A. Fazakerley (2004), Temporal evolution of two auroral arcs as measured by the Cluster satellite and coordinated ground-based instruments, *Annales Geophysicae*, *22*, 4089–4101, doi:10.5194/angeo-22-4089-2004.
- Akasofu, S.-I. (1964), The development of the auroral substorm, *Planet. Space Sci.*, *12*, 273–282, doi:10.1016/0032-0633(64)90151-5.
- Akasofu, S.-I. (1979), A search for the interplanetary quantity controlling the development of geomagnetic storms, *Royal Astronomical Society, Quarterly Journal*, *20*, 119–137.
- Akasofu, S.-I. (1981), Relationships between the AE and Dst indices during geomagnetic storms, *J. Geophys. Res.*, *86*, 4820–4822, doi:10.1029/JA086iA06p04820.
- Appleton, E. V. (1932), Wireless studies of the ionosphere, *Institution of Electrical Engineers-Proceedings of the Wireless Section of the Institution*, *7*(21), 257–265.
- Arnoldy, R. L., K. Dragoon, L. J. Cahill, Jr., S. B. Mende, and T. J. Rosenberg (1982), Detailed correlations of magnetic field and riometer observations at  $L = 4.2$  with pulsating aurora, *J. Geophys. Res.*, *87*, 10,449–10,456, doi:10.1029/JA087iA12p10449.
- Asikainen, T., and K. Mursula (2013), Correcting the NOAA/MEPED energetic electron fluxes for detector efficiency and proton contamination, *J. Geophys. Res. Space Physics*, *118*, 6500–6510, doi:10.1002/jgra.50584.
- Axford, W. I. (1963), The formation and vertical movement of dense ionized layers in the ionosphere due to neutral wind shears, *J. Geophys. Res.*, *68*, 769–779, doi:10.1029/JZ068i003p00769.

- Axford, W. I., and C. O. Hines (1961), A unifying theory of high-latitude geophysical phenomena and geomagnetic storms, *Canadian Journal of Physics*, *39*, 1433, doi:10.1139/p61-172.
- Bates, D. R. (1959), Some problems concerning the terrestrial atmosphere above about the 100 km level, *Royal Society of London Proceedings Series A*, *253*, 451–462, doi:10.1098/rspa.1959.0207.
- Baumjohann, W., and R. A. Treumann (1997), *Basic Space Plasma Physics*, World Scientific.
- Beharrell, M. J., F. Honary, C. J. Rodger, and M. A. Clilverd (2015), Substorm-induced energetic electron precipitation: Morphology and prediction, *J. Geophys. Res. Space Physics*, *120*(4), 2993–3008, doi:10.1002/2014JA020632.
- Belov, A. V., E. A. Eroshenko, V. A. Oleneva, and V. G. Yanke (2008), Connection of Forbush effects to the X-ray flares, *J. Atmos. Sol. Terr. Phys.*, *70*, 342–350, doi:10.1016/j.jastp.2007.08.021.
- Berkey, F. T. (1978), Observations of pulsating aurora in the day sector auroral zone, *Planet. Space Sci.*, *26*, 635–650, doi:10.1016/0032-0633(78)90097-1.
- Bertucci, C., F. Duru, N. Edberg, M. Fraenz, C. Martinecz, K. Szego, and O. Vaisberg (2011), The induced magnetospheres of Mars, Venus, and Titan, *Space Science Reviews*, *162*, 113–171, doi:10.1007/s11214-011-9845-1.
- Blelly, P.-L., C. Lathuillère, B. Emery, J. Lilensten, J. Fontanari, and D. Alcaydé (2005), An extended TRANSCAR model including ionospheric convection: simulation of EISCAT observations using inputs from AMIE, *Annales Geophysicae*, *23*, 419–431, doi:10.5194/angeo-23-419-2005.
- Brain, D., and J. S. Halekas (2012), Aurora in Martian mini magnetospheres, in *Auroral Phenomenology and Magnetospheric Processes: Earth And Other Planets, Geophysical Monograph Series*, vol. 197, edited by A. Keiling, E. Donovan, F. Bagenal, and C. T., pp. 123–132, American Geophysical Union, Washington, D. C., doi:10.1029/2011GM001201.
- Brain, D. A., S. Barabash, S. W. Bougher, F. Duru, B. Jakosky, and R. Modolo (2017), Solar wind interaction and atmospheric escape, in *The Atmosphere and Climate of Mars*, edited by R. Haberle, R. Clancy, F. Forget, M. Smith, and R. Zurek, chap. 15, pp. 464–496, Cambridge University Press, Cambridge, United Kingdom.
- Brändström, B. U. E., C.-F. Enell, O. Widell, T. Hansson, D. Whiter, S. Mäkinen, D. Mikhaylova, K. Axelsson, F. Sigernes, N. Gulbrandsen, N. M. Schlatter, A. G. Gjendem, L. Cai, J. P. Reistad, M. Daae, T. D. Demissie, Y. L. Andalsvik, O. Roberts, S. Poluyanov, and S. Chernouss (2012), Results from the intercalibration of optical low light calibration sources 2011, *Geoscientific Instrumentation, Methods and Data Systems*, *1*(1), 43–51, doi:10.5194/gi-1-43-2012.

- Breit, G., and M. A. Tuve (1925), A radio method of estimating the height of the conducting layer, *Nature*, *116*, 357, doi:10.1038/116357a0.
- Brekke, A. (2012), *Physics of the Upper Polar Atmosphere*, Springer Atmospheric Sciences, Springer Berlin Heidelberg.
- Burch, J. L., and P. H. Reiff (1985), Field-aligned currents and ion convection at high altitudes, *Advances in Space Research*, *5*, 23–40, doi:10.1016/0273-1177(85)90113-9.
- Burgess, D. (1995), Collisionless shocks, in *Introduction to Space Physics*, edited by M. G. Kivelson and C. T. Russel, chap. 5, pp. 129–163, Cambridge University Press, Cambridge, United Kingdom.
- Cahoy, K. L., D. P. Hinson, and G. L. Tyler (2006), Radio science measurements of atmospheric refractivity with Mars Global Surveyor, *J. Geophys. Res. Planets*, *111*, E05003, doi:10.1029/2005JE002634.
- Cain, D. L., A. Kliore, G. S. Levy, and D. A. Tito (1967), A radio occultation experiment to probe the atmosphere of Venus, *Journal of Spacecraft and Rockets*, *4*, 1339–1346, doi:10.2514/3.29082.
- Cardnell, S., O. Witasse, G. J. Molina-Cuberos, M. Michael, S. N. Tripathi, G. Déprez, F. Montmessin, and K. O'Brien (2016), A photochemical model of the dust-loaded ionosphere of Mars, *J. Geophys. Res. Planets*, *121*, 2335–2348, doi:10.1002/2016JE005077.
- Chiu, M. C., U. I. von-Mehlem, C. E. Willey, T. M. Betenbaugh, J. J. Maynard, J. A. Krein, R. F. Conde, W. T. Gray, J. W. Hunt, Jr., L. E. Mosher, M. G. McCullough, P. E. Panneton, J. P. Staiger, and E. H. Rodberg (1998), ACE Spacecraft, *Space Science Reviews*, *86*, 257–284, doi:10.1023/A:1005002013459.
- Chree, C. (1913), Some phenomena of sunspots and of terrestrial magnetism at Kew Observatory, *Philosophical Transactions of the Royal Society of London Series A*, *212*, 75–116, doi:10.1098/rsta.1913.0003.
- Clancy, R. T., M. J. Wolff, B. A. Whitney, B. A. Cantor, M. D. Smith, and T. H. McConnochie (2010), Extension of atmospheric dust loading to high altitudes during the 2001 Mars dust storm: MGS TES limb observations, *Icarus*, *207*, 98–109, doi:10.1016/j.icarus.2009.10.011.
- Coroniti, F. V., and C. F. Kennel (1970), Electron precipitation pulsations, *J. Geophys. Res.*, *75*, 1279–1289, doi:10.1029/JA075i007p01279.
- Cortie, A. L. (1912), Sun-spots and terrestrial magnetic phenomena, 1898–1911, *Monthly Notices of the Royal Astronomical Society*, *73*, 52, doi:10.1093/mnras/73.1.52.
- Cowley, S. W. H., and M. Lockwood (1992), Excitation and decay of solar wind-driven flows in the magnetosphere-ionosphere system, *Annales Geophysicae*, *10*, 103–115.

- Cravens, T. E. (1997), *Physics of Solar System Plasmas*, Cambridge University Press, Cambridge, United Kingdom.
- Crider, D. H., D. A. Brain, M. H. Acuña, D. Vignes, C. Mazelle, and C. Bertucci (2004), Mars Global Surveyor observations of solar wind magnetic field draping around Mars, *Space Science Reviews*, *111*, 203–221, doi:10.1023/B:SPAC.0000032714.66124.4e.
- Davis, T. N. (1978), Observed characteristics of auroral forms, *Space Science Reviews*, *22*, 77–113, doi:10.1007/BF00215814.
- Davis, T. N., and M. Sugiura (1966), Auroral electrojet activity index AE and its universal time variations, *J. Geophys. Res.*, *71*, 785–801, doi:10.1029/JZ071i003p00785.
- Denton, M. H., and J. E. Borovsky (2012), Magnetosphere response to high-speed solar wind streams: A comparison of weak and strong driving and the importance of extended periods of fast solar wind, *J. Geophys. Res. Space Physics*, *117*, A00L05, doi:10.1029/2011JA017124.
- Denton, M. H., T. Ulich, and E. Turunen (2009), Modification of midlatitude ionospheric parameters in the F2 layer by persistent high-speed solar wind streams, *Space Weather*, *7*, S04006, doi:10.1029/2008SW000443.
- Dubinin, E. M., M. Fraenz, J. Woch, E. Roussos, J. D. Winningham, R. A. Frahm, A. Coates, F. Leblanc, R. Lundin, and S. Barabash (2008), Access of solar wind electrons into the Martian magnetosphere, *Annales Geophysicae*, *26*, 3511–3524, doi:10.5194/angeo-26-3511-2008.
- Dungey, J. W. (1961), Interplanetary magnetic field and the auroral zones, *Physical Review Letters*, *6*, 47–48, doi:10.1103/PhysRevLett.6.47.
- Dungey, J. W. (1963), The structure of the ionosphere, or adventures in velocity space, in *Geophysics: The Earth's Environment*, edited by C. DeWitt, J. Hiebolt, and A. Lebeau, pp. 522–536, Gordon and Breach, New York, United States.
- Eastwood, J. P., J. J. H. Videira, D. A. Brain, and J. S. Halekas (2012), A chain of magnetic flux ropes in the magnetotail of Mars, *Geophys. Res. Lett.*, *39*, L03104, doi:10.1029/2011GL050444.
- Enell, C.-F., A. Kozlovsky, T. Turunen, T. Ulich, S. Väitalo, C. Scotto, and M. Pezzopane (2016), Comparison between manual scaling and Autoscala automatic scaling applied to Sodankylä Geophysical Observatory ionograms, *Geoscientific Instrumentation, Methods and Data Systems*, *5*, 53–64, doi:10.5194/gi-5-53-2016.
- Evans, D. S., and M. S. Greer (2000), *Polar Orbiting Environmental Satellite Space Environment Monitor-2: Instrument Description and Archive Data Documentation*, US Department of Commerce, National Oceanic and Atmospheric Administration, Oceanic and Atmospheric Research Laboratories, Space Environment Center.

- Fjeldbo, G., A. J. Kliore, and V. R. Eshleman (1971), The neutral atmosphere of Venus as studied with the Mariner V radio occultation experiments, *Astronomical Journal*, *76*, 123, doi:10.1086/111096.
- Förster, M., S. E. Haaland, G. Paschmann, J. M. Quinn, R. B. Torbert, H. Vaith, and C. A. Kletzing (2008), High-latitude plasma convection during northward IMF as derived from in-situ magnetospheric Cluster EDI measurements, *Annales Geophysicae*, *26*(9), 2685–2700, doi:10.5194/angeo-26-2685-2008.
- Fowler, C. M., L. Andersson, R. E. Ergun, M. Morooka, G. Delory, D. J. Andrews, R. J. Lillis, T. McEnulty, T. D. Weber, T. M. Chamandy, A. I. Eriksson, D. L. Mitchell, C. Mazelle, and B. M. Jakosky (2015), The first in situ electron temperature and density measurements of the Martian nightside ionosphere, *Geophys. Res. Lett.*, *42*, 8854–8861, doi:10.1002/2015GL065267.
- Fox, J. L. (2009), Morphology of the dayside ionosphere of Mars: Implications for ion outflows, *J. Geophys. Res. Planets*, *114*, E12005, doi:10.1029/2009JE003432.
- Frank, L. A. (1967), On the extraterrestrial ring current during geomagnetic storms, *J. Geophys. Res.*, *72*(15), 3753–3767, doi:10.1029/JZ072i015p03753.
- Fränz, M., J. D. Winningham, E. Dubinin, E. Roussos, J. Woch, S. Barabash, R. Lundin, M. Holmström, H. Andersson, M. Yamauchi, A. Grigoriev, R. A. Frahm, J. R. Sharber, J. R. Scherrer, A. J. Coates, Y. Soobiah, D. R. Linder, D. O. Kataria, E. Kallio, T. Säles, P. Riihelä, W. Schmidt, H. E. J. Koskinen, J. Kozyra, J. Luhmann, E. Roelof, D. Williams, S. Livi, C. C. Curtis, K. C. Hsieh, B. R. Sandel, M. Grande, M. Carter, J.-A. Sauvaud, A. Fedorov, J.-J. Thocaven, S. McKenna-Lawler, S. Orsini, R. Cerulli-Irelli, M. Maggi, P. Wurz, P. Bochsler, N. Krupp, K. Asamura, and C. Dierker (2006), Plasma intrusion above Mars crustal fields — Mars Express ASPERA-3 observations, *Icarus*, *182*, 406–412, doi:10.1016/j.icarus.2005.11.016.
- Gonzalez, W. D., B. T. Tsurutani, and A. L. Clúa de Gonzalez (1999), Interplanetary origin of geomagnetic storms, *Space Science Reviews*, *88*, 529–562, doi:10.1023/A:1005160129098.
- Gosling, J., and V. Pizzo (1999), Formation and evolution of corotating interaction regions and their three dimensional structure, *Space Science Reviews*, *89*(1), 21–52, doi:10.1023/A:1005291711900.
- Gurnett, D. A., R. L. Huff, D. D. Morgan, A. M. Persoon, T. F. Averkamp, D. L. Kirchner, F. Duru, F. Akalin, A. J. Kopf, E. Nielsen, A. Safaeinili, J. J. Plaut, and G. Picardi (2008), An overview of radar soundings of the martian ionosphere from the Mars Express spacecraft, *Advances in Space Research*, *41*, 1335–1346, doi:10.1016/j.asr.2007.01.062.
- Gurvits, L. I., T. M. Bocanegra Bahamon, G. Cimò, D. A. Duev, G. Molera Calvés, S. V. Pogrebenko, I. de Pater, L. L. A. Vermeersen, P. Rosenblatt, J. Oberst, P. Charlot, S. Frey, and V. Tudose (2013), Planetary Radio Interferometry and

- Doppler Experiment (PRIDE) for the JUICE mission, *European Planetary Science Congress Abstracts*, 8, EPSC2013-357.
- Halekas, J. S., J. P. Eastwood, D. A. Brain, T. D. Phan, M. Øieroset, and R. P. Lin (2009), In situ observations of reconnection Hall magnetic fields at Mars: Evidence for ion diffusion region encounters, *J. Geophys. Res. Space Physics*, 114, A11204, doi:10.1029/2009JA014544.
- Hara, T., K. Seki, Y. Futaana, M. Yamauchi, M. Yagi, Y. Matsumoto, M. Tokumaru, A. Fedorov, and S. Barabash (2011), Heavy-ion flux enhancement in the vicinity of the Martian ionosphere during CIR passage: Mars Express ASPERA-3 observations, *J. Geophys. Res. Space Physics*, 116, A02,309, doi:10.1029/2010JA015778.
- Hargreaves, J. K. (1969), Auroral absorption of HF radio waves in the ionosphere: A review of results from the first decade of riometry., *IEEE Proceedings*, 57, 1348–1373.
- Hargreaves, J. K. (1995), *The Solar-Terrestrial Environment*, Cambridge University Press, Cambridge, United Kingdom.
- Hedin, A. E. (1991), Extension of the MSIS thermosphere model into the middle and lower atmosphere, *J. Geophys. Res.*, 96, 1159–1172, doi:10.1029/90JA02125.
- Hickey, M. P., R. L. Walterscheid, and G. Schubert (2011), Gravity wave heating and cooling of the thermosphere: Sensible heat flux and viscous flux of kinetic energy, *J. Geophys. Res. Space Physics*, 116, A12326, doi:10.1029/2011JA016792.
- Hinson, D. P., R. A. Simpson, J. D. Twicken, G. L. Tyler, and F. M. Flasar (1999), Initial results from radio occultation measurements with Mars Global Surveyor, *J. Geophys. Res.*, 104, 26,997–27,012, doi:10.1029/1999JE001069.
- Hughes, W. J. (1994), Magnetospheric ULF waves: A Tutorial with a historical perspective, *Washington DC American Geophysical Union Geophysical Monograph Series*, 81, 1–11, doi:10.1029/GM081p0001.
- Hughes, W. J. (1995), The magnetopause, magnetotail, and magnetic reconnection, in *Introduction to Space Physics*, edited by M. G. Kivelson and C. T. Russel, chap. 9, pp. 227–287, Cambridge University Press, Cambridge, United Kingdom.
- Humberset, B. K., J. W. Gjerloev, M. Samara, R. G. Michell, and I. R. Mann (2016), Temporal characteristics and energy deposition of pulsating auroral patches, *J. Geophys. Res. Space Physics*, 121(7), 7087–7107, doi:10.1002/2016JA022921, 2016JA022921.
- Hundhausen, A. J. (1995), The solar wind, in *Introduction to Space Physics*, edited by M. G. Kivelson and C. T. Russel, chap. 4, pp. 91–128, Cambridge University Press, Cambridge, United Kingdom.

- Huttunen, K. E. J., H. E. J. Koskinen, T. I. Pulkkinen, A. Pulkkinen, M. Palmroth, E. G. D. Reeves, and H. J. Singer (2002), April 2000 magnetic storm: Solar wind driver and magnetospheric response, *J. Geophys. Res. Space Physics*, *107*(A12), 1440, doi:10.1029/2001JA009154.
- Iijima, T., and T. A. Potemra (1978), Large-scale characteristics of field-aligned currents associated with substorms, *J. Geophys. Res.*, *83*, 599–615, doi:10.1029/JA083iA02p00599.
- Ilie, R., M. W. Liemohn, M. F. Thomsen, J. E. Borovsky, and J. Zhang (2008), Influence of epoch time selection on the results of superposed epoch analysis using ACE and MPA data, *J. Geophys. Res. Space Physics*, *113*(A3), A00A14, doi:10.1029/2008JA013241.
- Iyemori, T. (1990), Storm-time magnetospheric currents inferred from mid-latitude geomagnetic field variations, *Journal of Geomagnetism and Geoelectricity*, *42*, 1249–1265.
- Izakov, M. N. (2007), Turbulence in the free atmospheres of Earth, Mars, and Venus: A review, *Solar System Research*, *41*, 355–384, doi:10.1134/S0038094607050012.
- Jaynes, A. N., M. R. Lessard, J. V. Rodriguez, E. Donovan, T. M. Loto'Aniu, and K. Rychert (2013), Pulsating auroral electron flux modulations in the equatorial magnetosphere, *J. Geophys. Res. Space Physics*, *118*, 4884–4894, doi:10.1002/jgra.50434.
- Johnstone, A. D. (1978), Pulsating aurora, *Nature*, *274*, 119–126, doi:10.1038/274119a0.
- Jordan, R., G. Picardi, J. Plaut, K. Wheeler, D. Kirchner, A. Safaeinili, W. Johnson, R. Seu, D. Calabrese, E. Zampolini, A. Cicchetti, R. Huff, D. Gurnett, A. Ivanov, W. Kofman, R. Orosei, T. Thompson, P. Edenhofer, and O. Bombaci (2009), The Mars express MARSIS sounder instrument, *Planet. Space Sci.*, *57*, 1975–1986, doi:10.1016/j.pss.2009.09.016.
- Kavanagh, A. J., F. Honary, E. F. Donovan, T. Ulich, and M. H. Denton (2012), Key features of >30 keV electron precipitation during high speed solar wind streams: A superposed epoch analysis, *J. Geophys. Res. Space Physics*, *117*, A00L09, doi:10.1029/2011JA017320.
- King, J. H., and N. E. Papitashvili (2005), Solar wind spatial scales in and comparisons of hourly Wind and ACE plasma and magnetic field data, *J. Geophys. Res. Space Physics*, *110*, A02104, doi:10.1029/2004JA010649.
- Kliore, A., and D. A. Tito (1967), Radio occultation investigations of the atmosphere of Mars, *Journal of Spacecraft and Rockets*, *4*, 578–582, doi:10.2514/3.28912.
- Kojima, M., and T. Kakinuma (1987), Solar cycle evolution of solar wind speed structure between 1973 and 1985 observed with the interplanetary scintillation method, *J. Geophys. Res.*, *92*, 7269–7279, doi:10.1029/JA092iA07p07269.

- Kozlovsky, A., T. Turunen, and T. Ulich (2013), Rapid-run ionosonde observations of traveling ionospheric disturbances in the auroral ionosphere, *J. Geophys. Res. Space Physics*, *118*, 5265–5276, doi:10.1002/jgra.50474.
- Kvifte, G. J., and H. Pettersen (1969), Morphology of the pulsating aurora, *Planet. Space Sci.*, *17*, 1599–1607, doi:10.1016/0032-0633(69)90148-2.
- Lam, M. M., R. B. Horne, N. P. Meredith, S. A. Glauert, T. Moffat-Griffin, and J. C. Green (2010), Origin of energetic electron precipitation >30 keV into the atmosphere, *J. Geophys. Res. Space Physics*, *115*, A00F08, doi:10.1029/2009JA014619.
- Lassen, H. (1927), Über den Einfluss des Erdmagnetfeldes auf die Fortpflanzung der elektrischen Wellen der drahtlosen Telegraphie in der Atmosphäre, *Elektrische Nachrichten-Technik*, *4*, 324–334.
- Lewis, K. W., and F. J. Simons (2012), Local spectral variability and the origin of the Martian crustal magnetic field, *Geophys. Res. Lett.*, *39*, L18201, doi:10.1029/2012GL052708.
- Li, W., R. M. Thorne, J. Bortnik, Y. Nishimura, and V. Angelopoulos (2011a), Modulation of whistler mode chorus waves: 1. Role of compressional Pc4-5 pulsations, *J. Geophys. Res. Space Physics*, *116*, A06205, doi:10.1029/2010JA016312.
- Li, W., J. Bortnik, R. M. Thorne, Y. Nishimura, V. Angelopoulos, and L. Chen (2011b), Modulation of whistler mode chorus waves: 2. Role of density variations, *J. Geophys. Res. Space Physics*, *116*, A06206, doi:10.1029/2010JA016313.
- Lilensten, J., and P. L. Blelly (2002), The TEC and  $F_2$  parameters as tracers of the ionosphere and thermosphere, *J. Atmos. Sol. Terr. Phys.*, *64*, 775–793, doi:10.1016/S1364-6826(02)00,079-2.
- Lindal, G. F., G. E. Wood, H. B. Hotz, D. N. Sweetnam, V. R. Eshleman, and G. L. Tyler (1983), The atmosphere of Titan: An analysis of the Voyager 1 radio occultation measurements, *Icarus*, *53*, 348–363, doi:10.1016/0019-1035(83)90155-0.
- Lowder, C., J. Qiu, and R. Leamon (2017), Coronal holes and open magnetic flux over cycles 23 and 24, *Solar Physics*, *292*, 18, doi:10.1007/s11207-016-1041-8.
- Lugaz, N., W. B. Manchester, IV, and T. I. Gombosi (2005), The evolution of coronal mass ejection density structures, *The Astrophysical Journal*, *627*, 1019–1030, doi:10.1086/430465.
- Lui, A. T. Y. (1991), A synthesis of magnetospheric substorm models, *J. Geophys. Res.*, *96*, 1849–1856, doi:10.1029/90JA02430.
- Lyatsky, W., P. T. Newell, and A. Hamza (2001), Solar illumination as cause of the equinoctial preference for geomagnetic activity, *Geophys. Res. Lett.*, *28*, 2353–2356, doi:10.1029/2000GL012803.

- Mahaffy, P. R., C. R. Webster, S. K. Atreya, H. Franz, M. Wong, P. G. Conrad, D. Harpold, J. J. Jones, L. A. Leshin, H. Manning, et al. (2013), Abundance and isotopic composition of gases in the Martian atmosphere from the Curiosity rover, *Science*, *341*, 263–266, doi:10.1126/science.1237966.
- Marchaudon, A., and P.-L. Blelly (2015), A new interhemispheric 16-moment model of the plasmasphere-ionosphere system: IPIM, *J. Geophys. Res. Space Physics*, *120*, 5728–5745, doi:10.1002/2015JA021193.
- Marquardt, D. W. (1963), An algorithm for least-squares estimation of nonlinear parameters, *SIAM Journal on Applied Mathematics*, *11*(2), 431–441, doi:10.1137/0111030.
- Masunaga, K., K. Seki, D. A. Brain, X. Fang, Y. Dong, B. M. Jakosky, J. P. McFadden, J. S. Halekas, J. E. P. Connerney, D. L. Mitchell, and F. G. Eparvier (2017), Statistical analysis of the reflection of incident O<sup>+</sup> pickup ions at Mars: MAVEN observations, *J. Geophys. Res. Space Physics*, *122*(4), 4089–4101, doi:10.1002/2016JA023516, 2016JA023516.
- Mayyasi, M., and M. Mendillo (2015), Why the Viking descent probes found only one ionospheric layer at Mars, *Geophys. Res. Lett.*, *42*(18), 7359–7365, doi:10.1002/2015GL065575, 2015GL065575.
- McComas, D. J., S. J. Bame, P. Barker, W. C. Feldman, J. L. Phillips, P. Riley, and J. W. Griffee (1998), Solar Wind Electron Proton Alpha Monitor (SWEPAM) for the Advanced Composition Explorer, *Space Science Reviews*, *86*, 563–612, doi:10.1023/A:1005040232597.
- McIlwain, C. E. (1961), Coordinates for mapping the distribution of magnetically trapped particles, *J. Geophys. Res.*, *66*, 3681–3691, doi:10.1029/JZ066i011p03681.
- McKay-Bukowski, D., J. Vierinen, I. I. Virtanen, R. Fallows, M. Postila, T. Ulich, O. Wucknitz, M. Brentjens, N. Ebbendorf, C.-F. Enell, M. Gerbers, T. Grit, P. Gruppen, A. Kero, T. Iinatti, M. Lehtinen, H. Meulman, M. Norden, M. Orispää, T. Raita, J. P. de Reijer, L. Roininen, A. Schoenmakers, K. Stuurwold, and E. Turunen (2015), KAIRA: The Kilpisjärvi Atmospheric Imaging Receiver Array—System overview and first results, *IEEE Transactions on Geoscience and Remote Sensing*, *53*, 1440–1451, doi:10.1109/TGRS.2014.2342252.
- McPherron, R. L., and J. Weygand (2006), The solar wind and geomagnetic activity as a function of time relative to corotating interaction regions, in *Recurrent Magnetic Storms: Corotating Solar Wind Streams*, edited by B. T. Tsurutani, R. McPherron, W. Gonzalez, G. Lu, J. H. A. Sobral, and N. Gopalswamy, Geophysical Monograph Series, pp. 125–137, American Geophysical Union, Washington, D. C.
- Mendillo, M., A. Lollo, P. Withers, M. Matta, M. Pätzold, and S. Tellmann (2011), Modeling Mars’ ionosphere with constraints from same-day observations by Mars Global Surveyor and Mars Express, *J. Geophys. Res. Space Physics*, *116*, A11303, doi:10.1029/2011JA016865.

- Meredith, N. P., R. B. Horne, and R. R. Anderson (2001), Substorm dependence of chorus amplitudes: Implications for the acceleration of electrons to relativistic energies, *J. Geophys. Res.*, *106*, 13,165–13,178, doi:10.1029/2000JA900156.
- Milan, S. E., A. Grocott, C. Forsyth, S. M. Imber, P. D. Boakes, and B. Hubert (2009), A superposed epoch analysis of auroral evolution during substorm growth, onset and recovery: Open magnetic flux control of substorm intensity, *Annales Geophysicae*, *27*, 659–668, doi:10.5194/angeo-27-659-2009.
- Millour, E., F. Forget, A. Spiga, T. Navarro, J.-B. Madeleine, L. Montabone, A. Pottier, F. Lefevre, F. Montmessin, J.-Y. Chaufray, M. A. Lopez-Valverde, F. Gonzalez-Galindo, S. R. Lewis, P. L. Read, J.-P. Huot, M.-C. Desjean, and MCD/GCM development Team (2015), The Mars Climate Database (MCD version 5.2), *European Planetary Science Congress Abstracts*, *10*, EPSC2015-438.
- Miyoshi, Y., Y. Katoh, T. Nishiyama, T. Sakanoi, K. Asamura, and M. Hirahara (2010), Time of flight analysis of pulsating aurora electrons, considering wave-particle interactions with propagating whistler mode waves, *J. Geophys. Res. Space Physics*, *115*, A10312, doi:10.1029/2009JA015127.
- Miyoshi, Y., R. Kataoka, Y. Kasahara, A. Kumamoto, T. Nagai, and M. F. Thomsen (2013), High-speed solar wind with southward interplanetary magnetic field causes relativistic electron flux enhancement of the outer radiation belt via enhanced condition of whistler waves, *Geophys. Res. Lett.*, *40*, 4520–4525, doi:10.1002/grl.50916.
- Miyoshi, Y., S. Oyama, S. Saito, S. Kurita, H. Fujiwara, R. Kataoka, Y. Ebihara, C. Kletzing, G. Reeves, O. Santolik, M. Clilverd, C. J. Rodger, E. Turunen, and F. Tsuchiya (2015a), Energetic electron precipitation associated with pulsating aurora: EISCAT and Van Allen Probe observations, *J. Geophys. Res. Space Physics*, *120*, 2754–2766, doi:10.1002/2014JA020690.
- Miyoshi, Y., S. Saito, K. Seki, T. Nishiyama, R. Kataoka, K. Asamura, Y. Katoh, Y. Ebihara, T. Sakanoi, M. Hirahara, S. Oyama, S. Kurita, and O. Santolik (2015b), Relation between fine structure of energy spectra for pulsating aurora electrons and frequency spectra of whistler mode chorus waves, *J. Geophys. Res. Space Physics*, *120*, 7728–7736, doi:10.1002/2015JA021562.
- Molina-Cuberos, G. J., O. Witasse, J.-P. Lebreton, R. Rodrigo, and J. J. López-Moreno (2003), Meteoric ions in the atmosphere of Mars, *Planet. Space Sci.*, *51*, 239–249, doi:10.1016/S0032-0633(02)00197-6.
- Motoba, T., K. Takahashi, J. Gjerloev, S. Ohtani, and D. K. Milling (2013), The role of compressional Pc5 pulsations in modulating precipitation of energetic electrons, *J. Geophys. Res. Space Physics*, *118*, 7728–7739, doi:10.1002/2013JA018912.
- Motoba, T., S. Ohtani, B. J. Anderson, H. Korth, D. Mitchell, L. J. Lanzerotti, K. Shiokawa, M. Connors, C. A. Kletzing, and G. D. Reeves (2015), On the formation and origin of substorm growth phase/onset auroral arcs inferred from

- conjugate space-ground observations, *J. Geophys. Res. Space Physics*, *120*, 8707–8722, doi:10.1002/2015JA021676.
- Nagy, A. F., D. Winterhalter, K. Sauer, T. E. Cravens, S. Brecht, C. Mazelle, D. Crider, E. Kallio, A. Zakharov, E. Dubinin, M. Verigin, G. Kotova, W. I. Axford, C. Bertucci, and J. G. Trotignon (2004), The plasma Environment of Mars, *Space Science Reviews*, *111*(1), 33–114, doi:10.1023/B:SPAC.0000032718.47512.92.
- Newell, P. T., C. Meng, D. G. Sibeck, and R. Lepping (1989), Some low-altitude cusp dependencies on the interplanetary magnetic field, *J. Geophys. Res. Space Physics*, *94*(A7), 8921–8927, doi:10.1029/JA094iA07p08921.
- Newell, P. T., Y. I. Feldstein, Y. I. Galperin, and C.-I. Meng (1996), Morphology of nightside precipitation, *J. Geophys. Res.*, *101*, 10,737–10,748, doi:10.1029/95JA03516.
- Nier, A. O., and M. B. McElroy (1977), Composition and structure of Mars' upper atmosphere: Results from the neutral mass spectrometers on Viking 1 and 2, *J. Geophys. Res.*, *82*, 4341–4349, doi:10.1029/JS082i028p04341.
- Nilsson, H., S. Kirkwood, L. Eliasson, O. Norberg, J. Clemmons, and M. Boehm (1994), The ionospheric signature of the cusp: A case study using Freja and the Sondrestrom radar, *Geophys. Res. Lett.*, *21*, 1923–1926, doi:10.1029/94GL00698.
- Nishimura, Y., J. Bortnik, W. Li, R. M. Thorne, L. Chen, L. R. Lyons, V. Angelopoulos, S. B. Mende, J. Bonnell, O. L. Contel, C. Cully, R. Ergun, and U. Auster (2011), Multievent study of the correlation between pulsating aurora and whistler mode chorus emissions, *J. Geophys. Res. Space Physics*, *116*(A11), doi:10.1029/2011JA016876.
- Nishiyama, T., Y. Miyoshi, Y. Katoh, T. Sakanoi, R. Kataoka, and S. Okano (2016), Substructures with luminosity modulation and horizontal oscillation in pulsating patch: Principal component analysis application to pulsating aurora, *J. Geophys. Res. Space Physics*, *121*, 2360–2373, doi:10.1002/2015JA022288.
- Orosei, R., R. L. Jordan, D. D. Morgan, M. Cartacci, A. Cicchetti, F. Duru, D. A. Gurnett, E. Heggy, D. L. Kirchner, R. Noschese, W. Kofman, A. Masdea, J. J. Plaut, R. Seu, T. R. Watters, and G. Picardi (2015), Mars Advanced Radar for Subsurface and Ionospheric Sounding (MARSIS) after nine years of operation: A summary, *Planet. Space Sci.*, *112*, 98–114, doi:10.1016/j.pss.2014.07.010.
- Papitashvili, V. O., B. A. Belov, and L. I. Gromova (1989), Field-aligned currents and convection patterns in the southern polar cap during stable northward, southward, and azimuthal IMF, *IEEE Transactions on Plasma Science*, *17*, 167–173, doi:10.1109/27.24621.
- Parker, E. N. (1958), Dynamics of the interplanetary gas and magnetic fields., *Astrophys. J.*, *128*, 664–676, doi:10.1086/146579.

- Pätzold, M., F. M. Neubauer, L. Carone, A. Hagermann, C. Stanzel, B. Häusler, S. Remus, J. Selle, D. Hagl, D. P. Hinson, R. A. Simpson, G. L. Tyler, S. W. Asmar, W. I. Axford, T. Hagfors, J.-P. Barriot, J.-C. Cerisier, T. Imamura, K.-I. Oyama, P. Janle, G. Kirchengast, and V. Dehant (2004), MaRS: Mars Express Orbiter Radio Science, in *Mars Express: the Scientific Payload, ESA Special Publication*, vol. 1240, edited by A. Wilson and A. Chicarro, pp. 141–163.
- Pätzold, M., M. K. Bird, B. Häusler, K. Peter, S. Tellmann, and G. L. Tyler (2016), Comment on the paper “Mars Express radio occultation data: A novel analysis approach” by Grandin et al. (2014), *J. Geophys. Res. Space Physics*, *121*, 10,578–10,591, doi:10.1002/2015JA021955.
- Phipps, P. H., and P. Withers (2017), Radio occultations of the Io plasma torus by Juno are feasible, *J. Geophys. Res. Space Physics*, *22*(2), 1731–1750, doi:10.1002/2016JA023447.
- Pulkkinen, T. I., A. P. Dimmock, A. Lakka, A. Osmane, E. Kilpua, M. Myllys, E. I. Tanskanen, and A. Viljanen (2016), Magnetosheath control of solar wind–magnetosphere coupling efficiency, *J. Geophys. Res. Space Physics*, *121*(9), 8728–8739, doi:10.1002/2016JA023011.
- Rees, M. H. (1963), Auroral ionization and excitation by incident energetic electrons, *Planet. Space Sci.*, *11*, 1209–1218, doi:10.1016/0032-0633(63)90252-6.
- Rees, M. H. (1989), *Physics and Chemistry of the Upper Atmosphere*, Cambridge University Press, Cambridge, United Kingdom.
- Richter, A. K., and A. H. Luttrell (1986), Superposed epoch analysis of corotating interaction regions at 0.3 and 1.0 AU: A comparative study, *J. Geophys. Res. Space Physics*, *91*(A5), 5873–5878, doi:10.1029/JA091iA05p05873.
- Rishbeth, H., and M. Mendillo (2004), Ionospheric layers of Mars and Earth, *Planet. Space Sci.*, *52*, 849–852, doi:10.1016/j.pss.2004.02.007.
- Rishbeth, H., and I. C. F. Müller-Wodarg (1999), Vertical circulation and thermospheric composition: A modelling study, *Annales Geophysicae*, *17*, 794–805, doi:10.1007/s00585-999-0794-x.
- Rishbeth, H., K. J. F. Sedgemore-Schulthess, and T. Ulich (2000a), Semiannual and annual variations in the height of the ionospheric  $F_2$  peak, *Annales Geophysicae*, *18*, 285–299, doi:10.1007/s00585-000-0285-6.
- Rishbeth, H., I. C. F. Müller-Wodarg, L. Zou, T. J. Fuller-Rowell, G. H. Millward, R. J. Moffett, D. W. Idenden, and A. D. Aylward (2000b), Annual and semiannual variations in the ionospheric  $F_2$  layer: II. Physical discussion, *Annales Geophysicae*, *18*, 945–956, doi:10.1007/s00585-000-0945-6.
- Robineau, A., P. L. Blelly, and J. Fontanari (1996), Time dependent models of the auroral ionosphere above EISCAT, *J. Atmos. Terr. Phys.*, *58*, 257–271.

- Rodger, C. J., A. J. Kavanagh, M. A. Clilverd, and S. R. Marple (2013), Comparison between POES energetic electron precipitation observations and riometer absorptions: Implications for determining true precipitation fluxes, *J. Geophys. Res. Space Physics*, *118*, 7810–7821, doi:10.1002/2013JA019439.
- Rousseeuw, P. J., and C. Croux (1993), Alternatives to the median absolute deviation, *Journal of the American Statistical Association*, *88*(424), 1273–1283.
- Russell, C. T., and R. L. McPherron (1973), Semiannual variation of geomagnetic activity, *J. Geophys. Res.*, *78*, 92, doi:10.1029/JA078i001p00092.
- Sabine, E. (1852), On periodical laws discoverable in the mean effects of the larger magnetic disturbances. No. II, *Philosophical Transactions of the Royal Society of London*, *142*, 103–124.
- Saito, T. (1978), Long-period irregular magnetic pulsation, Pi3, *Space Science Reviews*, *21*, 427–467, doi:10.1007/BF00173068.
- Samson, J. C., and K. L. Yeung (1986), Some generalizations on the method of superimposed epoch analysis, *Planet. Space Sci.*, *34*, 1133–1142, doi:10.1016/0032-0633(86)90025-5.
- Sandahl, I., L. Eliasson, and R. Lundin (1980), Rocket observations of precipitating electrons over a pulsating aurora, *Geophys. Res. Lett.*, *7*, 309–312, doi:10.1029/GL007i005p00309.
- Sangalli, L., N. Partamies, M. Syrjäsuo, C.-F. Enell, K. Kauristie, and S. Mäkinen (2011), Performance study of the new EMCCD-based all-sky cameras for auroral imaging, *International Journal of Remote Sensing*, *32*, 2987–3003, doi:10.1080/01431161.2010.541505.
- Schinder, P. J., F. M. Flasar, E. A. Marouf, R. G. French, C. A. McGhee, A. J. Kliore, N. J. Rappaport, E. Barbini, D. Fleischman, and A. Anabtawi (2011a), Saturn’s equatorial oscillation: Evidence of descending thermal structure from Cassini radio occultations, *Geophys. Res. Lett.*, *38*, L08205, doi:10.1029/2011GL047191.
- Schinder, P. J., F. M. Flasar, E. A. Marouf, R. G. French, C. A. McGhee, A. J. Kliore, N. J. Rappaport, E. Barbini, D. Fleischman, and A. Anabtawi (2011b), The structure of Titan’s atmosphere from Cassini radio occultations, *Icarus*, *215*, 460–474, doi:10.1016/j.icarus.2011.07.030.
- Schneider, N. M., J. I. Deighan, S. K. Jain, A. Stiepen, A. I. F. Stewart, D. Larson, D. L. Mitchell, C. Mazelle, C. O. Lee, R. J. Lillis, J. S. Evans, D. Brain, M. H. Stevens, W. E. McClintock, M. S. Chaffin, M. Crismani, G. M. Holsclaw, F. Lefevre, D. Y. Lo, J. T. Clarke, F. Montmessin, and B. M. Jakosky (2015), Discovery of diffuse aurora on Mars, *Science*, *350*, 0313, doi:10.1126/science.aad0313.
- Seiff, A., and D. B. Kirk (1977), Structure of the atmosphere of Mars in summer at mid-latitudes, *J. Geophys. Res.*, *82*, 4364–4378, doi:10.1029/JS082i028p04364.

- Sergeev, V. A., V. Angelopoulos, and R. Nakamura (2012), Recent advances in understanding substorm dynamics, *Geophys. Res. Lett.*, *39*, L05101, doi:10.1029/2012GL050859.
- Shain, C. A. (1951), Galactic Radiation at 18.3 Mc/s., *Australian Journal of Scientific Research A Physical Sciences*, *4*, 258, doi:10.1071/PH510258.
- Shubin, V. N., A. T. Karpachev, and K. G. Tsybulya (2013), Global model of the  $F_2$  layer peak height for low solar activity based on GPS radio-occultation data, *J. Atmos. Sol. Terr. Phys.*, *104*, 106–115, doi:10.1016/j.jastp.2013.08.024.
- Shue, J.-H., P. Song, C. T. Russell, M. F. Thomsen, and S. M. Petrinec (2001), Dependence of magnetopause erosion on southward interplanetary magnetic field, *J. Geophys. Res.*, *106*, 18,777–18,788, doi:10.1029/2001JA900039.
- Slavin, J. A., B. T. Tsurutani, E. J. Smith, D. E. Jones, and D. G. Sibeck (1983), Average configuration of the distant ( $< 220R_e$ ) magnetotail: Initial ISEE-3 magnetic field results, *Geophys. Res. Lett.*, *10*(10), 973–976, doi:10.1029/GL010i010p00973.
- Smith, C. W., J. L'Heureux, N. F. Ness, M. H. Acuña, L. F. Burlaga, and J. Scheifele (1998), The ACE magnetic fields experiment, *Space Science Reviews*, *86*, 613–632, doi:10.1023/A:1005092216668.
- Sugiura, M. (1964), Hourly values of equatorial Dst for the IGY, *Ann. Int. Geophys. Yr.*, *35*.
- Sugiura, M., T. Kamei, A. Berthelier, and M. Menvielle (1991), *Equatorial Dst Index: 1957-1986*, ISGI Publications Office.
- Tanskanen, E. I. (2009), A comprehensive high-throughput analysis of substorms observed by IMAGE magnetometer network: Years 1993-2003 examined, *J. Geophys. Res. Space Physics*, *114*, A05204, doi:10.1029/2008JA013682.
- Tapping, K. F. (2013), The 10.7 cm solar radio flux ( $F_{10.7}$ ), *Space Weather*, *11*, 394–406, doi:10.1002/swe.20064.
- Tellmann, S., M. Pätzold, B. Häusler, D. P. Hinson, and G. L. Tyler (2013), The structure of Mars lower atmosphere from Mars Express Radio Science (MaRS) occultation measurements, *J. Geophys. Res. Planets*, *118*, 306–320, doi:10.1002/jgre.20058.
- Thorne, R. M., B. Ni, X. Tao, R. B. Horne, and N. P. Meredith (2010), Scattering by chorus waves as the dominant cause of diffuse auroral precipitation, *Nature*, *467*, 943–946, doi:10.1038/nature09467.
- Torbert, R. B., C. T. Russell, W. Magnes, R. E. Ergun, P.-A. Lindqvist, O. LeContel, H. Vaith, J. Macri, S. Myers, D. Rau, J. Needell, B. King, M. Granoff, M. Chutter, I. Dors, G. Olsson, Y. V. Khotyaintsev, A. Eriksson, C. A. Kletzing, S. Bounds, B. Anderson, W. Baumjohann, M. Steller, K. Bromund, G. Le, R. Nakamura, R. J. Strangeway, H. K. Leinweber, S. Tucker, J. Westfall, D. Fischer, F. Plaschke,

- J. Porter, and K. Lappalainen (2016), The FIELDS instrument suite on MMS: Scientific objectives, measurements, and data products, *Space Science Reviews*, *199*, 105–135, doi:10.1007/s11214-014-0109-8.
- Torr, M. R., and D. Torr (1973), The seasonal behaviour of the  $F_2$  layer of the ionosphere, *J. Atmos. Terr. Phys.*, *35*(12), 2237–2251, doi: [http://dx.doi.org/10.1016/0021-9169\(73\)90140-2](http://dx.doi.org/10.1016/0021-9169(73)90140-2).
- Trotignon, J., R. Grard, and A. Skalsky (1993), Position and shape of the Martian bow shock: The Phobos 2 plasma wave system observations, *Planet. Space Sci.*, *41*(3), 189–198, doi:[http://dx.doi.org/10.1016/0032-0633\(93\)90058-A](http://dx.doi.org/10.1016/0032-0633(93)90058-A).
- Turner, N. E., W. D. Cramer, S. K. Earles, and B. A. Emery (2009), Geoefficiency and energy partitioning in CIR-driven and CME-driven storms, *J. Atmos. Sol. Terr. Phys.*, *71*, 1023–1031, doi:10.1016/j.jastp.2009.02.005.
- Turunen, E., H. Matveinen, J. Tolvanen, and H. Ranta (1996),  $D$ -region ion chemistry model, *STEP handbook of ionospheric models*, pp. 1–25.
- Turunen, E., A. Kero, P. T. Verronen, Y. Miyoshi, S.-I. Oyama, and S. Saito (2016), Mesospheric ozone destruction by high-energy electron precipitation associated with pulsating aurora, *J. Geophys. Res. Atmospheres*, *121*(19), 11,852–11,861, doi: 10.1002/2016JD025015, 2016JD025015.
- Valdivia-Silva, J. E., H. Beraldi, M. Colín-García, J. L. García-Martínez, A. Heredia-Barbero, H. J. Durand-Manterola, A. Negrón-Mendoza, F. Ortega-Gutierrez, and S. Ramos (2013), Noachian environments on Mars and the possible emergence of life, in *Mars : Evolution, Geology and Exploration*, edited by A. G. Fairén, chap. 6, pp. 103–152, Nova Science Publishers.
- van Allen, J. A., and L. A. Frank (1959), Radiation around the Earth to a radial distance of 107,400 km, *Nature*, *183*, 430–434, doi:10.1038/183430a0.
- Velinov, P. I. Y., S. Asenovski, K. Kudela, J. Lastovicka, L. Mateev, A. Mishev, and P. Tonev (2013), Impact of cosmic rays and solar energetic particles on the Earth’s ionosphere and atmosphere, *J. Space Weather Space Climate*, *3*(27), A14, doi:10.1051/swsc/2013036.
- Verronen, P. T., A. Seppälä, M. A. Clilverd, C. J. Rodger, E. Kyrölä, C.-F. Enell, T. Ulich, and E. Turunen (2005), Diurnal variation of ozone depletion during the October–November 2003 solar proton events, *J. Geophys. Res. Space Physics*, *110*(A9), doi:10.1029/2004JA010932, A09S32.
- Vogt, M. F., P. Withers, K. Fallows, C. L. Flynn, D. J. Andrews, F. Duru, and D. D. Morgan (2016), Electron densities in the ionosphere of Mars: A comparison of MARSIS and radio occultation measurements, *J. Geophys. Res. Space Physics*, *121*, 10,241–10,257, doi:10.1002/2016JA022987.
- Vorobjev, V. G., and O. I. Yagodkina (2010), Seasonal and UT variations of the position of the auroral precipitation and polar cap boundaries, *Geomagnetism and Aeronomy*, *50*, 597–605, doi:10.1134/S0016793210050063.

- Vyushin, D., I. Zhidkov, S. Havlin, A. Bunde, and S. Brenner (2004), Volcanic forcing improves Atmosphere-Ocean Coupled General Circulation Model scaling performance, *Geophys. Res. Lett.*, *31*, L10206, doi:10.1029/2004GL019499.
- Walker, R. J., and C. T. Russel (1995), Solar-wind with magnetized planets, in *Introduction to Space Physics*, edited by M. G. Kivelson and C. T. Russel, chap. 6, pp. 164–182, Cambridge University Press, Cambridge, United Kingdom.
- Wang, J.-S., and E. Nielsen (2003), Behavior of the Martian dayside electron density peak during global dust storms, *Planet. Space Sci.*, *51*(4), 329–338, doi: http://dx.doi.org/10.1016/S0032-0633(03)00015-1.
- Wanliss, J. A., and K. M. Showalter (2006), High-resolution global storm index: Dst versus SYM-H, *J. Geophys. Res. Space Physics*, *111*, A02202, doi: 10.1029/2005JA011034.
- Winningham, J. D., F. Yasuhara, S. I. Akasofu, and W. J. Heikkila (1975), The latitudinal morphology of 10-eV to 10-keV electron fluxes during magnetically quiet and disturbed times in the 2100–0300 MLT sector, *J. Geophys. Res.*, *80*(22), 3148–3171, doi:10.1029/JA080i022p03148.
- Withers, P. (2009), A review of observed variability in the dayside ionosphere of Mars, *Advances in Space Research*, *44*, 277–307, doi:10.1016/j.asr.2009.04.027.
- Withers, P., M. O. Fillingim, R. J. Lillis, B. Häusler, D. P. Hinson, G. L. Tyler, M. Pätzold, K. Peter, S. Tellmann, and O. Witasse (2012), Observations of the nightside ionosphere of Mars by the Mars Express Radio Science Experiment (MaRS), *J. Geophys. Res. Space Physics*, *117*, A12307, doi:10.1029/2012JA018185.
- Withers, P., M. Matta, M. Lester, D. Andrews, N. J. T. Edberg, H. Nilsson, H. Opgenoorth, S. Curry, R. Lillis, E. Dubinin, M. Fränz, X. Han, W. Kofman, L. Lei, D. Morgan, M. Pätzold, K. Peter, A. Opitz, J. A. Wild, and O. Witasse (2016), The morphology of the topside ionosphere of Mars under different solar wind conditions: Results of a multi-instrument observing campaign by Mars Express in 2010, *Planet. Space Sci.*, *120*, 24–34, doi:10.1016/j.pss.2015.10.013.
- Yeroshenko, E., W. Riedler, K. Schwingenschuh, J. G. Luhmann, and M. Ong (1990), The magnetotail of Mars - PHOBOS observations, *Geophys. Res. Lett.*, *17*, 885–888, doi:10.1029/GL017i006p00885.



ISBN 978-952-62-1614-0 (paperback)

ISBN 978-952-62-1615-7 (pdf)

ISSN 1456-3673